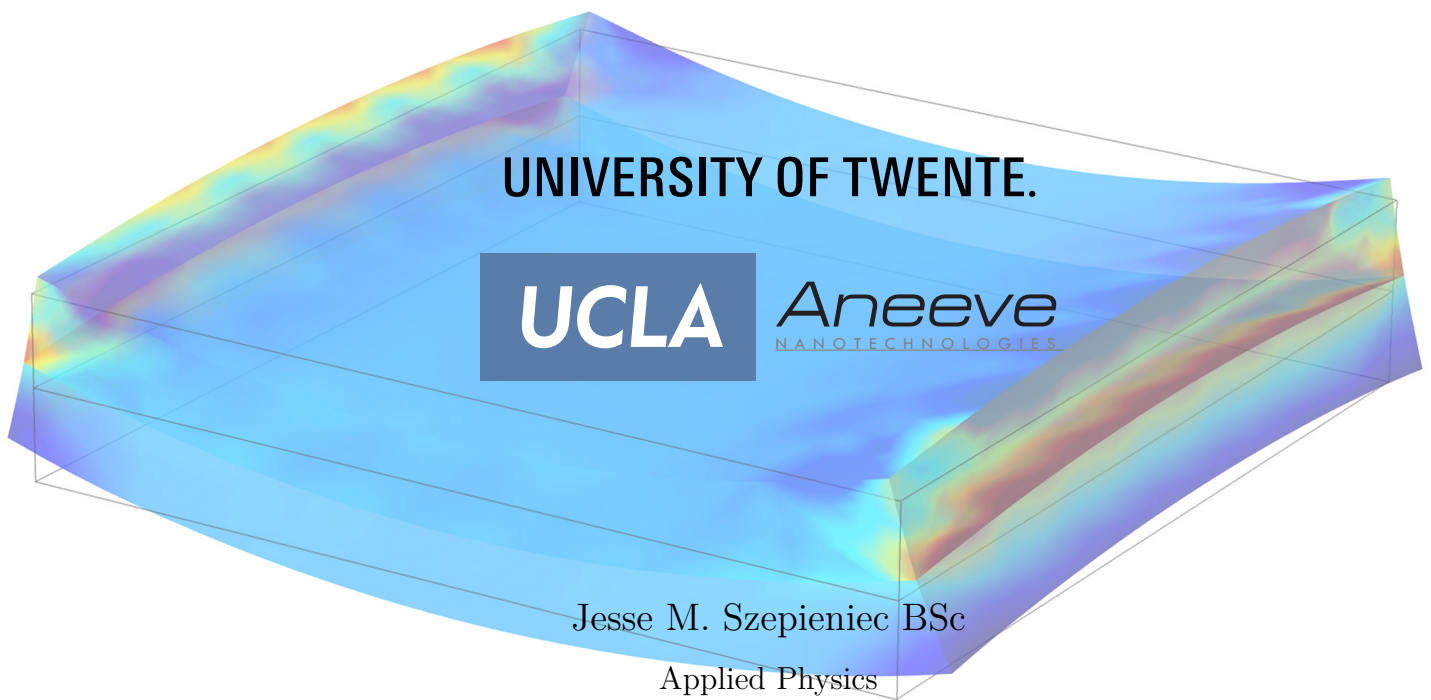


# Magnetolectric Thin Film Laminate Composites for Voltage-Controlled Tunable Nonreciprocal RF Devices



Submitted in partial fulfillment of the requirements for the degree of  
*Master of Science Applied Physics*

2012 November

---

*Graduation Committee*

Prof. Dr. Ing. A.J.H.M. Rijnders

Dr. Ir. M. Huijben

Prof. Dr. Ir. A. Brinkman

Inorganic Materials Science (IMS)

Faculty of Science & Technology

MESA+ Institute of Nanotechnology

University of Twente

The Netherlands

Aneve Nanotechnologies LLC

UCLA California NanoSystems Institute

USA

Cover: Simulation of the induced magnetic field in a piezoelectric-magnetolectric laminate composite heterostructure. Piezoelectric deformation is exaggerated for clarity.

## Abstract

Military and commercial applications for microwave components continue to demand smaller, more efficient, frequency-agile devices. As the mobile frequency spectrum grows increasingly crowded, the demands on battery life, size, weight and costs, increase. Adaptability to these ever changing conditions becomes beneficial. It is technologies that enable such adaptability that are becoming increasingly relevant. Conventional, magnetic field tuning of ferrite devices is often slow, bulky, noisy, and requires comparatively high power consumption for operation. Voltage-tunability provides a pathway towards tunable RF components with fast tuning, low noise levels, requiring minimal power and producing components that can be easily miniaturized and integrated. The feasibility of magnetoelectrically tunable RF isolators for frequencies above 10 GHz was investigated. Metallic magnetostatic surface wave isolators were constructed employing  $\text{Ni}_{80}\text{Fe}_{20}$  films in coplanar and microstrip geometries. Magnetoelectric coupling was shown for a  $\text{Co}_{80}\text{Fe}_{20}/(011)\text{PMN-PT}(70:30)$  heterostructure. The  $M_r/M_s$  ratio was reduced by 26% by an applied electric field of 0.01 kV/cm. Barium M-type hexaferrite (BaM) thin films were grown on highly (111) oriented Pt plated silicon and PMN-PT(011) substrates through metallo-organic decomposition. Based on the high squareness ratio obtained for the out-of-plane orientation, the film on silicon was suspected to be highly textured with the crystallographic  $c$ -axis out-of-plane. Sol-gel deposition of PMN-PT (70:30) was investigated. When annealed at  $600^\circ$ , a predominantly perovskite, highly (021) oriented spin-coated film is obtained. Finally, the first steps towards a ME model of voltage-tunable RF devices were undertaken. Basic 3D, two-way, linear magnetoelectrical coupling was realized in a magnetostatic approximation using finite element method (FEM) software.

## Samenvatting

Militaire en commerciële toepassingen voor microgolfcomponenten eisen kleinere, efficiëntere, frequentie-flexibele apparaten. Terwijl het mobiele spectrum alsmat dichter bevolkt raakt, worden er hardere eisen gesteld aan de levensduur van de batterijen, het gewicht en de kosten. Een aanpassingsvermogen voor deze steeds veranderende condities wordt als een voordeel beschouwd. Het is technologieën die juist dat aanpassingsvermogen mogelijk maken die nu in toenemende mate relevant aan het worden zijn. Conventionele afstelbare ferriet apparaten maken gebruik van een magneetveld en zijn vaak langzaam, omvangrijk, vatbaar voor stoorgeluiden, en vereisen een relatief hoog stroomverbruik. Voltage-afstelbaarheid is een weg naar radiofrequentie (RF) componenten met snelle afstelbaarheid, laag niveau aan , minimaal stroomgebruik en componenten die makkelijk geminiaturiseerd en geïntegreerd kunnen worden. De haalbaarheid van magnetoelektrische (ME) afgestelde RF isolatoren voor frequenties boven 10 GHz is onderzocht. Metallische magnetostatische oppervlaktegolfisolatoren zijn gefabriceerd, gebruikmakende van  $\text{Ni}_{80}\text{Fe}_{20}$  films in coplanaire en micro stripgeometrie. ME koppeling is gerealiseerd voor een  $\text{Co}_{80}\text{Fe}_{20}/\text{PMN-PT}(011)$  heterostructuur. De  $M_r/M_s$  ratio kon met 26% gereduceerd worden bij een aangelegd elektrisch veld van 0.01 kV/cm. M-type hexaferriet dunne films zijn gegroeid op sterk (111) georiënteerde Pt geplaatste silicium en PMN-PT(011) substraten met behulp van metallo-organische decompositie. De film op silicium is vermoedelijk sterk getextureerd met de *c*-as uit het vlak gericht. Verder is sol-gel depositie van PMN-PT (70:30) onderzocht. Na een anneal-stap op 600° C, werd een overwegend perovskiet, sterk (021) georiënteerde gespinoate film verkregen. Ten laatste werden de eerste stappen richting een ME simulatie voor voltage-afstelbare radiofrequentieapparaten ondernomen. Eenvoudige 3D, wederzijdse lineaire ME koppeling is gerealiseerd in een magnetostatische benadering gebruikmakende van eindige elementenmethode software.

In loving memory of

C.J. van Zwet

1927–2012

&

M. Sillevis Smitt

1924–2012

A sensitive compass having a Bi needle would be ideal for the young man going west or east, for it always aligns itself at right angles to the magnetic field.

William H. Hayt Jr., *Engineering Electromagnetics*, 1958

# Contents

<b>List of Figures</b>	<b>vi</b>
<b>List of Tables</b>	<b>viii</b>
<b>Preface</b>	<b>xi</b>
<b>Research Method</b>	<b>xii</b>
<b>1 Introduction</b>	<b>1</b>
1.1 Background and Theory . . . . .	4
1.1.1 Magnetism . . . . .	4
1.1.2 Microwave Theory . . . . .	9
1.1.3 Microwave Network Analysis . . . . .	14
1.1.4 The Magnetoelectric Effect . . . . .	16
1.2 Application Potential . . . . .	23
1.3 Research Goals . . . . .	24
1.4 Original Research Proposal . . . . .	24
1.5 Dissertation Organization . . . . .	25
<b>2 Metallic Magnetostatic Surface Wave Isolator</b>	<b>26</b>
2.1 Introduction . . . . .	26
2.2 Background & Theory . . . . .	28
2.3 Coplanar Waveguide (GSSG) . . . . .	31
2.3.1 Materials & Methods . . . . .	31
2.3.2 Results & Discussion . . . . .	31
2.4 Coplanar Waveguide (SGS) . . . . .	33
2.4.1 Materials & Methods . . . . .	33

2.4.2	Results & Discussion . . . . .	34
2.5	Microstrip . . . . .	35
2.5.1	Materials & Methods . . . . .	35
2.5.2	Results & Discussion . . . . .	35
2.6	Results & Discussion . . . . .	37
2.7	Conclusion . . . . .	39
<b>3</b>	<b>Magnetolectric Composite Materials Characterization</b>	<b>40</b>
3.1	Introduction . . . . .	40
3.1.1	PMN-PT (68:32) Single Crystal Substrates . . . . .	41
3.2	CoFe/PMN-PT Thin Film on Substrate Heterostructure . . . . .	43
3.2.1	Introduction . . . . .	43
3.2.2	Materials & Methods . . . . .	45
3.2.3	Results & Discussion . . . . .	45
3.2.4	Conclusion . . . . .	48
3.3	BaM/PMN-PT Thin Film on Substrate Heterostructure . . . . .	48
3.3.1	Methods & Materials . . . . .	50
3.3.2	Results & Discussion . . . . .	51
3.3.3	Conclusion . . . . .	53
<b>4</b>	<b>PMN-PT Sol-Gel Deposition Optimization</b>	<b>54</b>
4.1	Introduction . . . . .	54
4.2	Methods & Materials . . . . .	57
4.3	Results & Discussion . . . . .	58
4.4	Conclusion . . . . .	61
<b>5</b>	<b>Simulation of Magnetolectrically Coupled RF Devices</b>	<b>63</b>
5.1	Introduction . . . . .	63
5.2	Derivation of the Constitutive Relations . . . . .	64
5.3	Implementation . . . . .	69
5.3.1	The Magnetic Field Interface . . . . .	69
5.3.2	The Piezoelectric Interface . . . . .	69
5.4	Verification of the Model . . . . .	70
5.4.1	Piezoelectric Material Properties . . . . .	70

5.4.2 Magnetostrictive Material Properties . . . . .	71
5.5 Results & Discussion . . . . .	72
5.6 Conclusion . . . . .	75
<b>6 Conclusion</b>	<b>76</b>
<b>7 Suggestions for Future Work</b>	<b>80</b>
<b>A Microwave Theory</b>	<b>84</b>
A.1 Frequency Bands . . . . .	84
A.2 Derivation of Polder Permeability . . . . .	85
<b>B Modeling Parameters and Derivations</b>	<b>87</b>
B.1 Magnetic Field . . . . .	87
B.1.1 Boundary Conditions for the Magnetic Fields Module . . . . .	88
B.2 Structural Mechanics . . . . .	88
B.3 Implementation . . . . .	91
B.4 Modeling Parameters . . . . .	92
B.4.1 Spring Foundation . . . . .	92
B.4.2 Piezoelectric Material Parameters . . . . .	92
B.4.3 Magnetostrictive Material Parameters . . . . .	93
B.5 Notation of the Piezoelectric and Piezomagnetic Tensors . . . . .	93
<b>C Thin Film Characterization</b>	<b>95</b>
<b>References</b>	<b>96</b>

# List of Figures

1.1	The Hysteresis Loop of a Ferromagnet . . . . .	5
1.2	Superexchange . . . . .	7
1.3	Magnetic Easy and Hard Axes . . . . .	8
1.4	Precession of a Magnetic Dipole Moment . . . . .	10
1.5	Permeability As a Function of Frequency . . . . .	12
1.6	Linewidth and Losses . . . . .	13
1.7	S-Parameter Definition . . . . .	14
1.8	Decoupling of Generator and Load . . . . .	15
1.9	Transmitter and Receiver on The Same Antenna . . . . .	16
1.10	Origin And Behavior of Magnetostriction . . . . .	17
1.11	Structure-Property Relations for the Intrinsic Piezoelectric Effect in $\text{PbTiO}_3$ . . . . .	19
1.12	Piezoelectric-Magnetostrictive Composite . . . . .	22
2.1	Magnetostatic Modes . . . . .	28
2.2	Magnetostatic Wave Disperion . . . . .	29
2.3	MSSW Isolator Shorted Microstrip Structure . . . . .	30
2.4	Coplanar Waveguide (GSSG) . . . . .	32
2.5	Spin-Waves in Coplanar Waveguide (SGS) . . . . .	33
2.6	Coplanar Waveguide (SGS) Device Geometry . . . . .	34
2.7	S-Parameters for CPW S-G-S Geometry . . . . .	34
2.8	Microstrip Device Geometry . . . . .	36
2.9	S-parameters for Mirostrip Geometry . . . . .	36
2.10	SQUID measurement of NiFe . . . . .	38
3.1	PMN-PT Crystal Polarization Orientations and Strain Curve . . . . .	41

## LIST OF FIGURES

---

3.2	Material Parameters as a Function of Cobalt Content in CoFe . . . . .	44
3.3	In-Plane Magnetic Characterization of $\text{Co}_{80}\text{Fe}_{20}$ . . . . .	45
3.4	CoFe on PMN-PT . . . . .	46
3.5	BaM Structure, Doping Effects and Magnetic Hysteresis . . . . .	49
3.6	Magnetic Hysteresis for $\text{BaAl}_{0.25}\text{Fe}_{11.75}\text{O}_{19}$ . . . . .	52
3.7	Structural and Magnetic Characterization of a BaM thin film on PMN-PT	52
4.1	Phase Diagram of PMN-PT . . . . .	55
4.2	PMN-PT Sol-Gel XRD Profiles for 4 and 7 layers . . . . .	58
4.3	PMN-PT Sol-Gel XRD Profiles for 1 Layer . . . . .	60
5.1	H-Field Distribution for 100 nm $\text{Fe}_{75}\text{Ga}_{10}\text{B}_{15}$ /PMN-PT . . . . .	73
C.1	BaM on Pt/Si . . . . .	95

# List of Tables

2.1	CPW GSSG Isolator Dimension Matrix . . . . .	31
2.2	CPW SGS Isolator Dimension Matrix . . . . .	33
2.3	Microstrip Isolator Dimension Matrix . . . . .	35
A.1	Waveguide Frequency Bands . . . . .	84

## Acknowledgements

After an internship at UC Berkeley I returned home with a strong desire to, somehow, conduct my Master thesis assignment in an entrepreneurial environment in California. Kos, Guus, Mark, thank you for recognizing in me that desire and helping me turn that dream into reality. Without doubt, this has been one of the most valuable and transformative experiences of my life.

Thanks to Kin, Jing and Pedram for the invaluable discussions and help with sample preparations and measurements. A very special thank you to Scott for his guidance in the FEM model derivation and implementation.

Gentlemen from the BRAK and Bracque. The world of physics started off as a lonely world for me, the BRAK changed that. Few things in my life have been as satisfying and rewarding as the friendships I have had the privilege to share with you fellow physicists.

Gentlemen from Heeren Jaarclub Quinta Essentia. At time of our inception, we barely knew one another. Some might even say our mutual association was random. Be that as it may, now, six years later, I have grown extremely fond of each and every one of you.

Fellow board members of the 21<sup>st</sup> board of ASV Taste. My memories are pervaded by joy, fun and laughter. It was truly an unforgettable year which we shared together.

Gentlemen from HST. It's easy to take for granted, but we created a special little place on the Noorderhagen. Undoubtedly some of my most fondest memories are from those times we shared there.

Ladies and gentlemen from Villa 65. The easy going, mischievous and fun-loving culture that underpinned the Villa 65 experience have continued to be a thread running through my entire college career.

Thank you mom and dad for your patience, understanding and guidance.

Thank you Marissa, for that benevolent kick in the ass that spurred me to follow my dream.

# Preface

The research presented in this thesis was conducted in collaboration with the Aneev team and its collaborators at UC Irvine and University of Colorado, Colorado Springs.

J.M. Szepieniec, A. Jooyaie, T. Wu, H. Li, K. Galatsis, “*STTR Phase I Monthly Report: November*”

J.M. Szepieniec, A. Jooyaie, T. Wu, H. Li, K. Galatsis, “*STTR Phase I Monthly Report: December*”

J.M. Szepieniec, A. Jooyaie, T. Wu, H. Li, K. Galatsis, “*STTR Phase I Monthly Report: January*”

J.M. Szepieniec, A. Jooyaie, T. Wu, H. Li, K. Galatsis, “*STTR Phase I Monthly Report: February*”

J.M. Szepieniec, A. Jooyaie, T. Wu, H. Li, K. Galatsis, “*STTR Phase I Final Report*”

J.M. Szepieniec, A. Jooyaie, T. Wu, Z. Celinski, K. Galatsis, “*STTR Phase II Proposal*”

# Research Method

The research outlined in this thesis was part of a research initiative led by Aneve Nanotechnologies and funded through a Phase I Small Business Technology Transfer (STTR) research and development fund issued by the US Army. STTRs are designed to bridge the gap between performance of basic science and commercialization of resulting innovations.

The length of the Phase I fund was six months and, by design, culminated in an elaborate Phase II proposal. This dictated the nature of the research to be less of a narrow in-depth approach and more of a holistic fast-paced approach. As a result, many different areas within the topic of tunable ME composites were covered, as opposed to a complete description of one facet.

# Chapter 1

## Introduction

At the onset of the 18th century, Dutch merchants affiliated to the Dutch East India Trade Company (Verenigd Oostindische Compagnie), set sail for the island of Ceylon — modern day Sri Lanka. They would return with — in addition to their usual cargo of fine spices [1] — a peculiar little gem: tourmaline. When placed in hot ashes, these crystals were known to first attract them, and, when cooled, to repel them [2]. The Dutch merchants referred to these gems as ‘aschentrekker’ — ash-drawer in English — and would use them to draw ashes from their pipes [3]. These gems demonstrated the seemingly miraculous phenomenon of *attraction at a distance*, assuaging the contemporaneous demand in Europe for curiosities.

The only other phenomenon contemporaries could relate this curious attracting power to, was that of magnetism. Although not well understood, magnets had long before found their application in compasses used for naval navigation. In fact, the treacherous and lengthy voyage to, and from Ceylon, had been made possible by virtue of that early application of magnetic technology. Not surprisingly, the tourmaline crystals, when first imported to Europe, were sometimes referred to as “Ceylon magnets” [4].

The effect observed in tourmaline crystals, however, is not magnetic in nature — it is *piezoelectric*. The material is strained by an expansion of the atomic lattice that occurs at elevated temperatures. Through the piezoelectric effect this strain is intrinsically coupled to a spontaneous polarization — which subsequently arises. In retrospect, however, relating an electric phenomenon to magnetism, was not that crazy of an idea. It turns out that these natural forces *are* intimately related. In fact, they

---

are different manifestations of the same physical phenomenon: the electromagnetic field. This was first observed by Hans Christian Ørsted, who noticed the deflection of a compass needle from magnetic north when the current from the battery he was using, was turned on and off. Michael Faraday later established the coupling between electric and magnetic fields and would go on to form the basis for the concept of the electromagnetic field. Subsequently, Maxwell was able to cast this into an elegant mathematical framework known as Maxwell's equations.

Maxwell's equations relate time varying electric and magnetic fields to spatial gradients of electric and magnetic fields. In doing so, these equations allow for a self-sustaining electromagnetic wave, where a time variation in one field generates a spatial gradient in the other. These manifestations, however, are inherently perpendicular.

By definition, then, these perpendicular relationships dictate the manner in which one can generate a magnetic field. A feat most often accomplished by sending a current through a conducting loop, which, in doing so, induces a magnetic field to pass through the loop. The induced magnetic field is directed perpendicularly to the plane in which the loop resides. In order to generate greater fields, larger currents, or more loops, are required — usually both are utilized. Thus, there is an inherent difficulty in generating large magnetic fields at a small scale. Not only are miniature electromagnets hard to engineer; getting to, and from, the desired fields, reveals another inherent difficulty. Ramping up to the desired current, involves a time varying magnetic field and will therefore induce a current density in the coil which opposes the magnetic field increase. As a result, ramping up and down can only be accomplished comparatively slowly as to minimize this magnetic induction. Comparatively slow-switching, hard-to-miniaturize technology is at risk of being rendered obsolete in a society continuously and ruthlessly shifting towards increasingly smaller and faster electronics.

Such is the fate of conventional tunable microwave electronics. Magnetic field tunable ferrite devices are currently used as resonators, filters, phase-shifters, circulators and isolators, in test equipment, radar, and electronic-warfare. They offer a wider tuning range than competing technology such as varactors, ferroelectrics, and micro-electromechanical systems (MEMS). The operating frequencies are tuned linearly by an applied magnetic bias. Unfortunately, the tuning response times limit their use at higher frequencies, and the material losses and device noise characteristics are be-

---

coming unacceptable. Furthermore, they are incompatible with monolithic microwave integrated circuits (MMIC) technology and have relatively high power requirements.

An interesting — perhaps counterintuitive — approach to this problem is captured by the question: “Can a *different* type of coupling between these two phenomena be conceived?” The answer came three decades after Maxwell’s equations were first published in their entirety, when Pierre Curie proposed just that: an intrinsic, linear coupling between electric and magnetic fields [5]. This *magnetoelectric* (ME) effect was predicted to manifest itself in a single structural arrangement of atoms — known also as a single phase material. These single phase materials have since been demonstrated, and extensively researched. The effective ME coupling at room temperature, however, has so far, been too small to satisfy any practical applications.

The quest for a greater magnitude of ME coupling brings us back to our peculiar piezoelectric crystal, tourmaline. The import of tourmaline crystals into Europe became a catalyst for research into crystallography [2]. This would eventually result in the understanding of the piezoelectric effect. It is this understanding that enabled Van Suchtelen [6] in 1972 to propose and pioneer the concept of product and sum properties in composite systems. Van Suchtelen showed that by bringing materials with different properties in intimate contact with one another, a composite system can be manufactured that can exhibit properties that are the product or sum of the constituent materials. In this manner, an effective magnetoelectric effect can be engineered by joining magnetostrictive and piezoelectric materials in composite systems.

Magnetoelectric composites show a linear coupling between electric potential and magnetization. These systems have the potential to provide a feasible pathway towards electrically tunable RF devices. The additional design space gained from exploiting voltage controlled magnetization could greatly expand the range of tuning in integrated microwave circuitry. This could result in RF systems that are lighter, smaller, more reliable and more affordable than current devices and systems.

Recent results in magnetoelectric composites used in tunable RF components suggest that isolator and circulator applications are within reach. Although tunable microwave filters and oscillators have been shown, comparatively little research has focused on the class of tunable nonreciprocal devices. The objective of this research is to demonstrate the feasibility of a magnetoelectrically tunable RF isolator at frequencies above 10 GHz.

## 1.1 Background and Theory

The frequency bands above 10 GHz have a number of possible applications, both military and civilian. As mobile technology further pervades our society, the frequency landscape becomes increasingly crowded. Mobile technology is shifting towards the use of higher frequencies to cope with this development.

In order to understand this new class of microwave devices and the potential that exists in their tuning, we must take a closer look at the areas of physics and microwave theory that are involved. We must review magnetism, its nonreciprocal character and its behavior at microwave frequencies. We must understand the constituent effects of magnetoelectricity in composites: piezoelectricity and magnetostriction. And we must understand how these phenomena come together to create a magnetoelectrically tunable RF component.

### 1.1.1 Magnetism

When a magnetic field  $\mathbf{H}$  is applied to a material, the material responds by allowing a flux density  $\mathbf{B}$  to be established within itself. The relationship between  $\mathbf{B}$  and  $\mathbf{H}$  is a material property, and is often approached as being linear. In cgs units

$$\mathbf{B} = \mathbf{H} + 4\pi\mathbf{M} \quad (1.1)$$

where  $\mathbf{M}$  denotes the magnetization of the material, and finds its origin in the individual magnetic moments in the material and how they interact with each other. The cgs unit of magnetization is emu/cm<sup>3</sup>. In SI units the relationship becomes

$$\mathbf{B} = \mu_0(\mathbf{H} + \mathbf{M}) \quad (1.2)$$

where  $\mu_0$  is the permeability of free space. The units of  $\mathbf{M}$  are the same as those of  $\mathbf{H}$ , namely (A/m). The units of  $\mu_0$  are weber/(A/m), also known as henry/m. Thus, the units of  $\mathbf{B}$  are weber/m<sup>2</sup>, or tesla (T).

The ratio of  $\mathbf{M}$  to  $\mathbf{H}$  is called the susceptibility:

$$\chi = \frac{\mathbf{M}}{\mathbf{H}} \quad \frac{\text{emu}}{\text{cm}^3\text{Oe}} \quad (1.3)$$

The susceptibility indicates how *responsive* a material is to an applied magnetic field. The ratio of  $\mathbf{B}$  to  $\mathbf{H}$  is called the permeability

$$\mu = \frac{\mathbf{B}}{\mathbf{H}} \quad \frac{\text{gauss}}{\text{Oe}} \quad (1.4)$$

and  $\mu$  indicates how *permeable* a material is to a magnetic field. A high permeability equates to a material which concentrates a large amount of flux density in its interior. The relationship between permeability and susceptibility in SI units is

$$\frac{\mu}{\mu_0} = 1 + \chi. \quad (1.5)$$

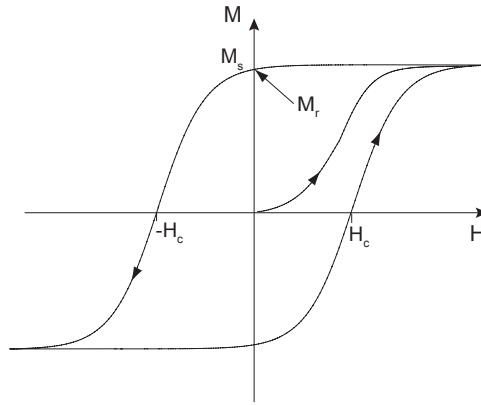


**Figure 1.1: The Hysteresis Loop of a Ferromagnet** - The ferromagnet starts in an unmagnetized state. Magnetization appears as an imposed magnetic field  $\mathbf{H}$ , modifies and eventually eliminates the microstructure of ferromagnetic domains magnetized in different directions, resulting in the saturation magnetization  $M_s$ . When the imposed field is subsequently removed, the magnetization is largely retained, denoted by the remnant magnetization  $M_r$ . To reduce  $M_r$  to zero a reverse magnetic field is needed equating to the coercivity  $H_c$ . After Ref. [7]

The ratio between the remnant magnetization ( $M_r$ ) and the saturation magnetization ( $M_s$ ) is known as the squareness. A factor close to 1 indicates that the hysteresis loop has a very square-like shape and a lot of the magnetization is retained upon removing the imposed field. This attribute is also referred to as self-biasing. Self-biasing renders an external biasing magnet unnecessary and is therefore a highly coveted feat for further miniaturization of ferrite and ferromagnetic microwave components [8].

Magnetic materials tend to be anisotropic. In this case the permeability needs to

become a  $3 \times 3$  tensor to account for the anisotropy

$$\begin{pmatrix} B_x \\ B_y \\ B_z \end{pmatrix} = \begin{pmatrix} \mu_{xx} & \mu_{xy} & \mu_{xz} \\ \mu_{yx} & \mu_{yy} & \mu_{yz} \\ \mu_{zx} & \mu_{zy} & \mu_{zz} \end{pmatrix} \begin{pmatrix} H_x \\ H_y \\ H_z \end{pmatrix} = \mu \begin{pmatrix} H_x \\ H_y \\ H_z \end{pmatrix} \quad (1.6)$$

### 1.1.1.1 Ferromagnetism

For a material to exhibit ferromagnetism, generally speaking, it must possess unpaired electrons in highly directional orbits — either in  $3d$  or  $4f$  shells [9]. These unpaired electrons minimize their interaction energy by aligning their spin moments in parallel. This gives rise to the macroscopic effect we have come to know as ferromagnetism. This type of magnetism is known to occur in transition metals and rare earth metals and many of their alloys.

### 1.1.1.2 Ferrimagnetism

The mechanism underlying ferromagnetism becomes more complicated in oxides due to the interaction of unpaired electrons with neighboring oxygen orbitals. The oxygen orbitals allow the cation electrons to align their spin moments in an antiparallel fashion in a process known as superexchange. This leads to the phenomenon of antiferromagnetism. A simple schematic of superexchange is shown in Fig. 1.2(a). Each  $\text{Mn}^{2+}$  ion has five unpaired  $d$ -electrons and forms a bond with oxygen that has a certain degree of covalence. The electrons in the oxygen  $p$ -orbital align antiparallel due to Pauli's exclusion principle. When shared with neighboring Mn atoms, the Mn  $d$ -orbitals align themselves antiparallel to one another.

Superexchange generally leads to a nett cancellation of magnetic moments of the cations. Certain materials, however, have cations that are linked by an oxygen atom and their magnetic behavior depends on the valence state of the respective cations. The spinel nickel ferrite,  $\text{NiFe}_2\text{O}_4$ , has magnetic properties that are dominated by exchange between  $\text{Ni}^{2+}$  and  $\text{Fe}^{3+}$  [10] as shown in Fig. 1.2(b). Most of the spin moments cancel due to anti-parallel alignment of the unpaired electrons, but a few remain uncanceled. This leads to a nett magnetic moment when they couple to their next-nearest neighboring cations. This effect is known as ferrimagnetism and it produces a macroscopic response which is similar to that of ferromagnetism. For this reason this effect is often treated as ferromagnetism.

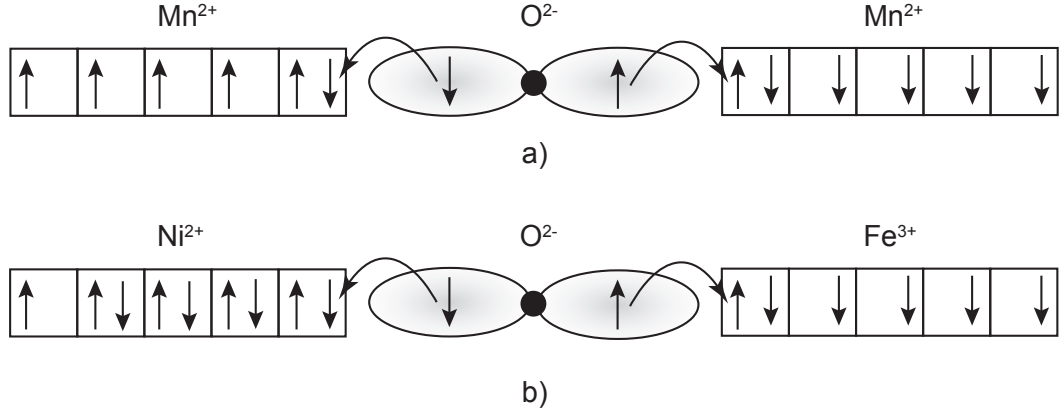


**Figure 1.2: Superexchange** - a) Schematic of the superexchange mechanism in MnO. After Ref. [9]. b) Schematic of a double exchange interaction in NiFe<sub>2</sub>O<sub>4</sub>. After Ref. [10].

### 1.1.1.3 Magnetocrystalline Anisotropy

As discussed in Section 1.1.1.1, a partially filled  $d$  or  $f$  shell causes an orbital imbalance. This constitutes the orbital contribution to the magnetic moment. It also gives rise to an anisotropic shape for the electron charge cloud. Since the greatest contribution to the magnetic moment derives from the electron spin, strong magnetoelastic coupling occurs for strong coupling between spin moment direction and charge cloud orientation. This interaction is known as spin-orbit coupling and its magnitude depends on relativistic aspects of electron motion. For the purposes of this thesis we can say that heavier atoms have larger centripetal forces and will cause electrons to move faster. Comparatively heavy rare earth atoms thus exhibit strong spin-orbit coupling. This results in a rigid attachment of the spin moment to the electron charge cloud [11].

Magnetocrystalline anisotropy for rare earth metals can now be defined. *“It is the tendency of a magnetic moment to point in a particular crystalline direction because of the electrical attraction or repulsion between its attached electronic charge cloud and the neighboring charged ions”* [11]. The anisotropy energy, then, is the energy required to rotate the magnetic moment away from its preferred direction. For transition metals, the spin-orbit coupling is an order of magnitude weaker and the atomic picture becomes more complex. The operational definition for magnetocrystalline anisotropy, however, remains the same [11].

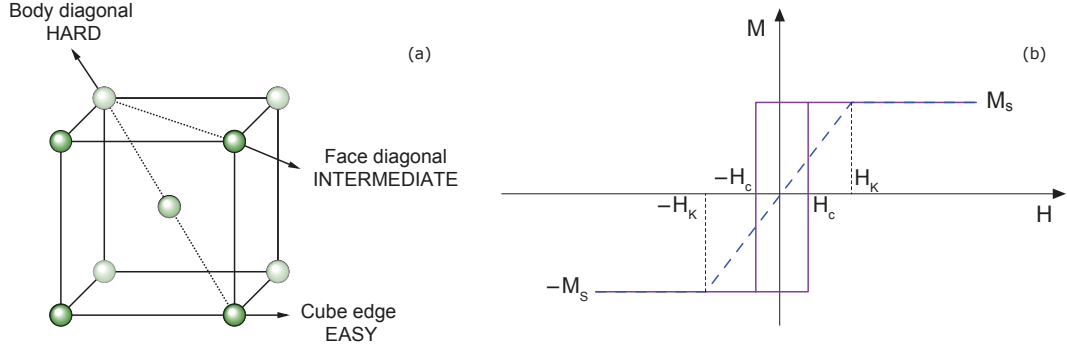


**Figure 1.3: Magnetic Easy and Hard Axes - a)** Easy, medium, and hard directions of magnetization in a unit cell of bcc Fe. Adapted from Ref. [9]. **b)** Schematic magnetization curves for a ferromagnet with the field oriented along the hard (dashed line) and easy (connected line) axes.

The preferred crystallographic directions are known as “easy” axes. Owing their name to the comparative ease of magnetizing a material to saturation when the external field is applied along a preferred direction (which is depicted in Fig. 1.3(a)). Different materials have different easy preferred axes. In body-centered cubic (bcc) iron the easy axis is the  $\langle 100 \rangle$  direction. Since bcc iron is a cubic crystal, all six cube edges are equivalent easy axes. The body diagonal is the hard axis of magnetization, and other orientations, are intermediate (see Fig. 1.3(a)). By contrast face-centered cubic Ni has an easy axis along the  $\langle 111 \rangle$  body diagonal. In hexagonal close-packed Co it is the  $\langle 0001 \rangle$  direction. Schematic magnetization curves for a ferromagnetic material are shown in Fig. 1.3(b), with the field applied along the easy and hard axes. The same saturation magnetization is achieved, but a comparatively larger applied field is required along the hard axis than is required along the easy axis [9].

Experimental values for the anisotropy field ( $H_k$ ) are often obtained through the measurement of the hysteresis loops of hard and easy axes. The anisotropy field is then obtained at the intersection of both curves at  $M_s$  [12].

#### 1.1.1.4 Shape Anisotropy

The DC bias field,  $H_0$ , internal to a ferromagnetic sample differs from the externally applied field,  $H_a$ , because of the boundary conditions at the surface of the sample. To illustrate this effect, consider a thin ferromagnetic plate. When the applied field is

normal to the plate, continuity of  $B_n$  at the surface of the plate gives

$$B_n = \mu_0 H_a = \mu_0 (M_s + H_0) \quad (1.7)$$

so the internal magnetic bias field is

$$H_0 = H_a - M_s \quad (1.8)$$

So the internal field is less than the applied field by an amount equal to the saturation magnetization. When the applied field is parallel to the ferromagnetic plate, the internal field is not reduced. In general, the internal field,  $\mathbf{H}$  is determined by the shape of the sample and its orientation with respect to the external field,  $\mathbf{H}_e$ . It can be expressed as

$$\mathbf{H} = \mathbf{H}_e - N\mathbf{M} \quad (1.9)$$

where  $N = N_x, N_y,$  or  $N_z$  is known as the demagnetization factor. Different shapes and orientations of the applied field correspond to different demagnetization factors.

Calculations of  $N_d$  for different shapes indicate that, for elongated samples,  $N_d$  is smallest along the long axis and largest along the short axis [9]. Thus, most of the applied field goes into overcoming the demagnetizing field. As a consequence it is easier to magnetize a sample along a long axis.

## 1.1.2 Microwave Theory

### 1.1.2.1 High Frequency Permeability

Understanding how ferri- and ferromagnetic materials respond to a high frequency magnetic field requires a study of the interaction between the magnetization of the ferrite and a radio frequency (RF) magnetic field. In the linear regime, this can be expressed in terms of the Polder tensor permeability [13].

The permeability tensor is derived from the tensor susceptibility ( $\chi$ ), which in turn, is derived from the equation of motion of a magnetic dipole (due to electron spin) in the presence of both a static magnetic field ( $H_0$ ) and a transverse RF magnetic field ( $H_y$ ) [14]. This is shown in Fig. 1.4(a) and it is assumed that  $|H_y| \ll |H_0|$ . The results are presented here, the derivations are listed in Appendix A.2.

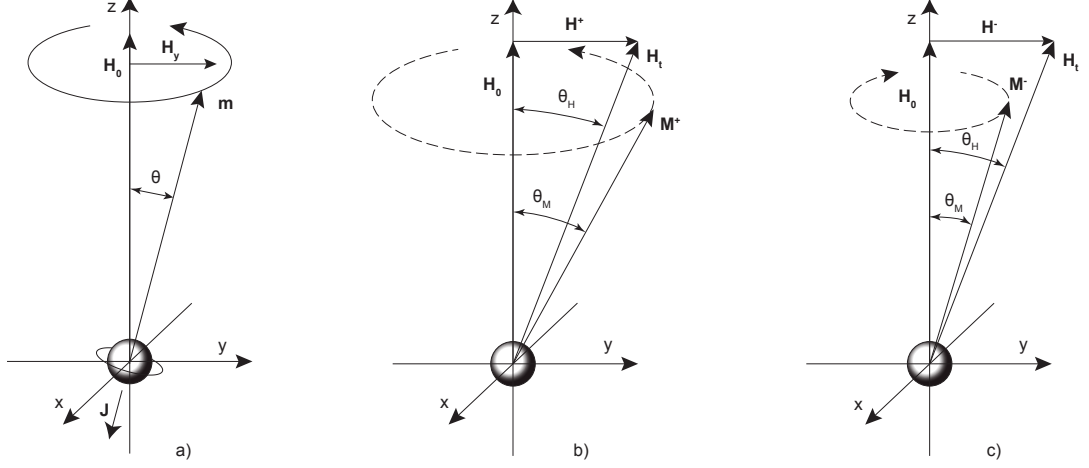


**Figure 1.4: Precession of a Magnetic Dipole Moment** - **a)** Spin magnetic dipole moment and angular momentum vectors for a spinning electron. **b)** Forced precession of a magnetic dipole with right hand circularly polarized (RHCP) field,  $\theta_M > \theta_H$  **c)** Forced precession of a magnetic dipole with left hand circularly polarized (LHCP) field,  $\theta_M < \theta_H$

Due to the electron spin, when a magnetic dipole ( $\mathbf{m}$ ) is immersed in a static magnetic field, it precesses about the field axis with an angular frequency  $\omega_0$ . If the dipole is subjected to a small transverse RF magnetic field  $H_y$  at an angular frequency  $\omega$ , the precession will be forced at this frequency and an additional transverse component ( $H_x$ ) will occur. Due to the time taken for  $\mathbf{m}$  to precess, there is a phase difference of  $90^\circ$  between  $H_x$  and  $H_y$ . The susceptibility tensor relating  $\mathbf{M}$  to  $\mathbf{H}$  can be derived from these assumptions [15] and is given by

$$\chi = \begin{pmatrix} \chi_{xx} & \chi_{xy} & 0 \\ \chi_{yx} & \chi_{yy} & 0 \\ 0 & 0 & 0 \end{pmatrix} \quad (1.10)$$

where the elements of  $\chi$  are given by

$$\chi_{xx} = \chi_{yy} = \frac{\omega_0 \omega_m}{\omega_0^2 - \omega^2} \quad (1.11)$$

$$\chi_{xy} = -\chi_{yx} = \frac{j\omega\omega_m}{\omega_0^2 - \omega^2} \quad (1.12)$$

and the relative permeability tensor follows in a straightforward manner [14]. The presence of  $\pm j$  in the off-diagonal terms is due to the  $90^\circ$  phase difference mentioned

earlier and is the cause of nonreciprocal behavior.

$$\boldsymbol{\mu} = \begin{pmatrix} \mu & j\kappa & 0 \\ -j\kappa & \mu & 0 \\ 0 & 0 & \mu_0 \end{pmatrix} \quad (1.13)$$

where

$$\mu = \mu_0 \left( 1 + \frac{\omega_0 \omega_m}{\omega_0^2 - \omega^2} \right) \quad (1.14)$$

$$\kappa = \mu_0 \frac{\omega \omega_m}{\omega_0^2 - \omega^2} \quad (1.15)$$

$$\omega_0 = \gamma \mu_0 H_0 \quad (1.16)$$

$$\omega_m = \gamma \mu_0 M \quad (1.17)$$

$$\omega = 2\pi f \quad (1.18)$$

$\mathbf{H}_0$  is the *internal* static magnetic field intensity and it is assumed to be uniform. In practice, it will be smaller than the applied field and nonuniform, which is further explored in 1.1.1.4. Also, the effects of losses have been neglected for clarity. In the absence of a transverse RF magnetic field, the cone angle in Fig. 1.4(a) will decrease with time until  $\mathbf{m}$  is aligned with  $H_0$ . In the presence of an RF field, the precession will be sustained albeit with some absorption of the field. Analogously to a gyroscope and the direction of gravity, there is a natural direction of precession associated with the direction of the static field. The precession can be reversed by reversing  $H_0$  [14].

Equations (1.14) and (1.15) show that the elements of the susceptibility or permeability tensors become infinite when the frequency  $\omega$ , equals the Larmor frequency  $\omega_0$  (Fig. 1.5(a)). This effect is known as ferromagnetic resonance (FMR), and occurs when the forced precession frequency is equal to the free precession frequency [15]. If the precession is against the natural direction ( $\mathbf{M}^-$ ), the cone angle  $\theta$  is reduced (Fig. 1.4(c)). If they are in the same sense ( $\mathbf{M}^+$ ), the cone angle will increase (Fig. 1.4(b)). Furthermore, if they are in the same sense and the driving frequency is equal to the natural frequency, resonance will occur accompanied by strong absorption of the RF field. The absorption can be observed by sweeping either the frequency at a static magnetic bias, or the magnetic bias at static frequency, until the precession frequency equals the microwave frequency [16].

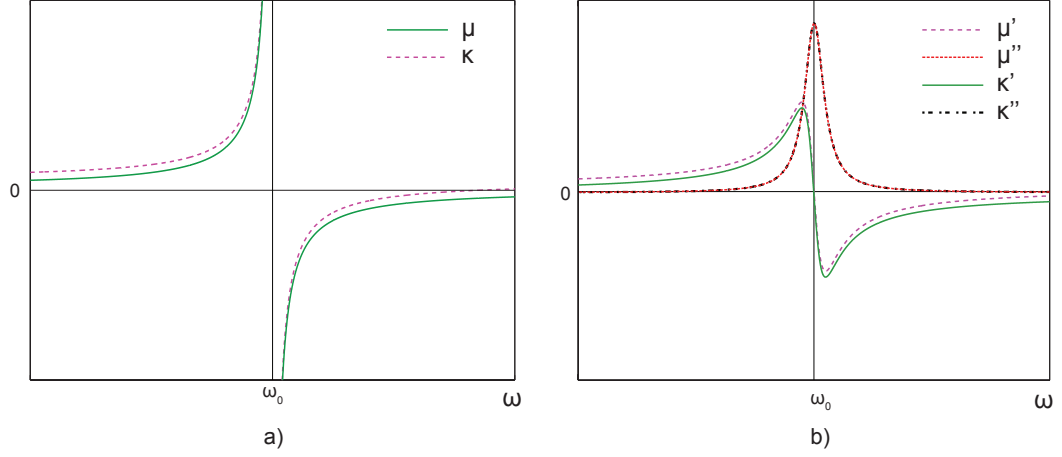


**Figure 1.5: Permeability As a Function of Frequency - a)** Permeability vs. frequency without losses taken into account. **b)** Permeability vs. frequency with losses taken into account

To take this absorption into account — as with other resonant systems — the resonant frequency is made complex

$$\omega_0 \leftarrow \omega_0 + j\alpha\omega \quad (1.19)$$

where  $\alpha$  is a damping factor (Fig. 1.5(b)). Using this new complex definition of the resonance frequency, eqs. (1.11) and (1.12), become

$$\chi_{xx} = \chi'_{xx} - j\chi''_{xx} \quad (1.20)$$

$$\chi_{xy} = \chi''_{xy} + j\chi'_{xy} \quad (1.21)$$

where the real and imaginary parts are given in Appendix A.2.

The range of static magnetic field, at a fixed frequency, over which this absorption is significant is denoted by the linewidth  $\Delta H$  (Fig. 1.6). Alternatively, the linewidth can just as easily be determined as a range in frequency at constant magnetic bias. In polycrystalline ferri-/ferromagnets, additional effects contribute to the linewidth, namely, random anisotropy fields and residual porosity [14]. The damping factor  $\alpha$  relates losses to linewidth through

$$\alpha = \frac{\mu_0\gamma\Delta H}{2\omega}. \quad (1.22)$$

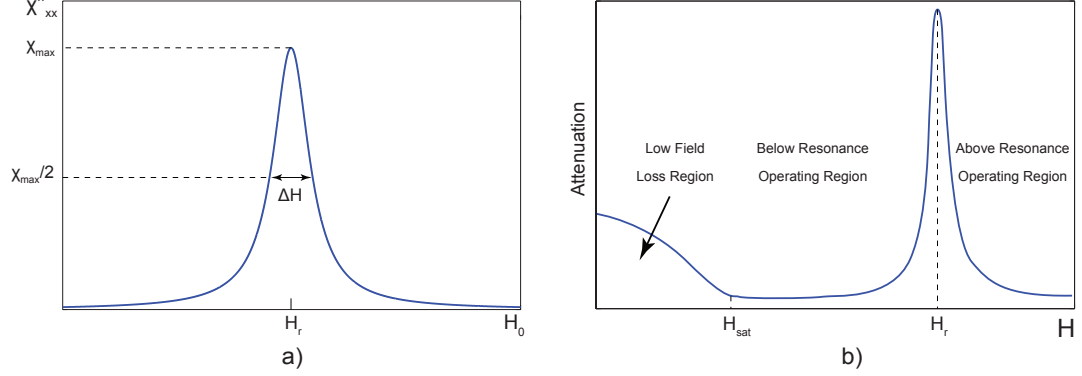


**Figure 1.6: Linewidth and Losses** - a) Definition of linewidth ( $\Delta H$ ) of the gyromagnetic resonance. After Ref. [17]. b) Attenuation vs. DC bias magnetic field. At low fields showing low field loss and at FMR showing loss due to resonance. After Ref. [18].

Due to the absorption of the microwave signal occurring at FMR, the FMR frequency becomes a key metric in the design of microwave devices, as can be understood from Fig. 1.6(b). This class of devices is characterized by a specified operation frequency bandwidth. Depending on the nature of the device and its mode of operation, the absorption which occurs at FMR will either be harnessed, or avoided. Logically, then, the FMR frequency and its linewidth have a critical role in the determination of the operation frequency bandwidth. As we will see in Section 2, devices based on magnetostatic surface waves operate above resonance.

Careful consideration of FMR frequency and linewidth are essential in the design of microwave devices. The ferromagnetic resonance frequency is defined to occur when the driving frequency equals the natural resonance frequency according to eq. (1.16). However, we must adjust this equation for the effective internal field, taking the shape anisotropy of the sample into account. For a finite-sized gyrotropic sample the gyromagnetic resonance frequency is altered by the demagnetization factors. The resonance frequency can be expressed in terms of applied bias field strength ( $H$ ) and demagnetization factors known as *Kittel's equation* [15].

$$\omega_r = \mu_0 \gamma \sqrt{[H + (N_x - N_z)M_s][H + (N_y - N_z)M_s]} \quad (1.23)$$

### 1.1.3 Microwave Network Analysis

#### 1.1.3.1 Scattering Matrix

The scattering matrix relates the voltage waves incident on the ports to those reflected from the ports. Scattering parameters — in certain cases — can be calculated or otherwise measured directly with a vector network analyzer (VNA) [15].

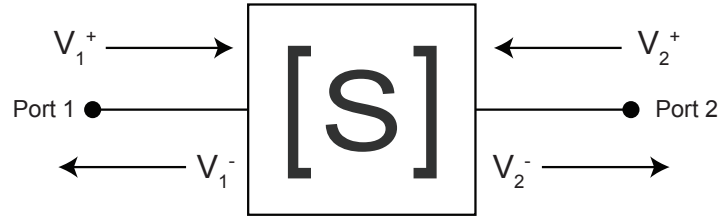


**Figure 1.7: S-Parameter Definition** - The S-Parameter, defined by forward and reverse voltage waves. After Ref. [19]

Fig. 1.7 illustrates a two-port device under test (DUT). If the generator is connected to port 1 and a matched load to port 2, the incident wave to the DUT is  $V_1^+$ . A wave reflected from the device back to port 1 is  $V_1^-$ . A signal traveling through the DUT and toward port 2 is  $V_2^-$ . Any reflection from the load (zero if it is truly matched) is  $V_2^+$ . The S-parameters are defined in terms of these voltage waves:

$$S_{11} = \frac{V_1^-}{V_1^+} \quad \text{Input Port Reflection Coefficient} \quad (1.24)$$

$$S_{21} = \frac{V_2^-}{V_1^+} \quad \text{Insertion Loss} \quad (1.25)$$

$$S_{12} = \frac{V_1^-}{V_2^+} \quad \text{Return loss} \quad (1.26)$$

$$S_{22} = \frac{V_2^-}{V_2^+} \quad \text{Output Port Reflection Coefficient} \quad (1.27)$$

The S-matrix becomes

$$[S] = \begin{bmatrix} S_{11} & S_{12} \\ S_{21} & S_{22} \end{bmatrix} \quad (1.28)$$

where

$$\begin{bmatrix} V_1^- \\ V_2^- \end{bmatrix} = \begin{bmatrix} S_{11} & S_{12} \\ S_{21} & S_{22} \end{bmatrix} \begin{bmatrix} V_1^+ \\ V_2^+ \end{bmatrix} \quad (1.29)$$

### 1.1.3.2 Isolator

Of critical importance for this research and one of the most used microwave ferrite components is the isolator, which is a two-port device having unidirectional transmission characteristics. The  $S$  matrix for an ideal isolator has the form

$$[S] = \begin{bmatrix} 0 & 0 \\ 1 & 0 \end{bmatrix} \quad (1.30)$$

indicating transmission occurs only in the direction from port 1 to port 2. Since  $[S]$  is not unitary, it must be lossy. Also,  $[S]$  is not asymmetric, since an isolator is a nonreciprocal component.

An example of an isolator application is the decoupling of a generator. Generators are affected by their loads which results in a frequency shift, instabilities and — in some cases — frequency jumping. To avoid this, an attenuator, of for instance 10 dB, can be placed between generator and load to attenuate the reflected signal by 20 dB (Fig. 1.8(a)). The reflected signal is attenuated, but this also results in high losses. Instead, a 20 dB isolator can be used. The attenuation is now limited to the insertion loss, which is normally less than 0.5 dB [20].

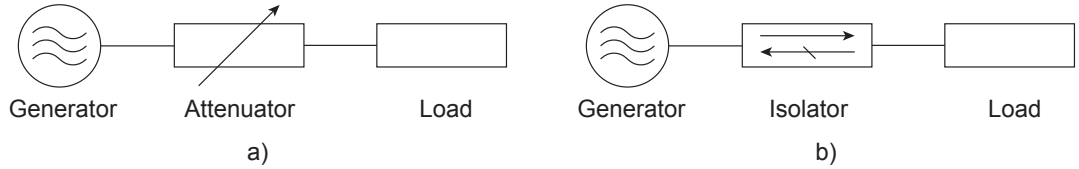


**Figure 1.8: Decoupling of Generator and Load - a)** Decoupling with a variable attenuator. **b)** Decoupling with an isolator

### 1.1.3.3 Circulator

A circulator is a three-port device that can be lossless and matched at all ports. The scattering matrix of an ideal circulator has the form

$$[S] = \begin{bmatrix} 0 & 0 & 1 \\ 1 & 0 & 0 \\ 0 & 1 & 0 \end{bmatrix} \quad (1.31)$$

which shows that power flow can occur from ports 1 to 2, 2 to 3, and 3 to 1, but not in the reverse direction.

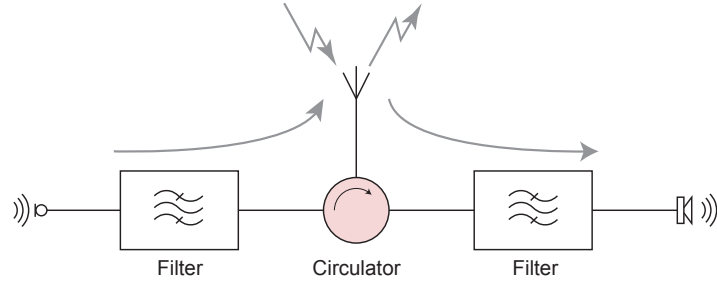


**Figure 1.9: Transmitter and Receiver on The Same Antenna** - Use of a circulator makes it possible for a transmitter and a receiver to use the same antenna

Circulators are used, for instance, if one wants to operate a transmitter and a receiver using the same antenna, tuned to different frequencies. Using a circulator the power of the transmitter at the input of the receiver branch is reduced (Fig. 1.9), thereby isolating transmitter from receiver [20]. For commercial circulators, the insertion loss typically does not exceed 0.5 dB and isolation is greater than 20 dB. The bandwidth can vary from several percent to more than an octave.

#### 1.1.4 The Magnetolectric Effect

Now that we've discussed the physics underlying a microwave isolator, we must investigate the physics underlying the magnetolectrical tuning mechanism. To understand the magnetolectric effect as a product property of magnetostriction and piezoelectricity, it is beneficial to understand those effects separately.

##### 1.1.4.1 Magnetostriction

Magnetostriction is defined as the deformation of a body in response to a change in its magnetization. More specifically, the magnetostrictive coefficients  $N_{ijkl}$  relate strain  $S_{ij}$  to the square of the magnetization  $M_k M_l$  [21]

$$S_I = N_{IJ} M_k M_l. \tag{1.32}$$

Magnetostriction, therefore, should not be mistaken with piezomagnetism — the latter being defined as linear relationship between strain and magnetization.

All magnetic materials exhibit magnetostriction to some degree. Empirical evidence, has shown that, in most cases, the second order effect of magnetostriction is far larger than the first order effect of piezomagnetism [11]. That being said, a pseudo-piezomagnetic response can be elicited by applying a static bias field which exceeds the driving field, as depicted in the grey region in Fig. 1.10(b).

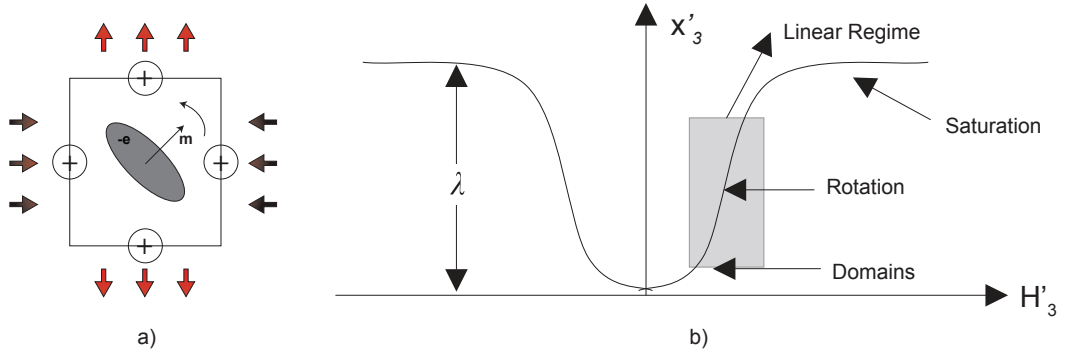


**Figure 1.10: Origin And Behavior of Magnetostriction - a)** Schematic of a  $4f$  charge density rotating in a magnetic field. After Ref. [11] **b)** Schematic of the magnetic field vs. strain behavior for a magnetostrictive material. After Ref. [21]

The magnetoelastic coupling — the coupling of a magnetic order to an elastic order — is the tendency of neighboring ions to shift their positions in response to the rotation of the magnetic moment and its rigidly attached anisotropic charge cloud, as can be seen in Fig. 1.10(a). This results in the anisotropic change in length of the crystal due to the application of a magnetic field which we call magnetostriction [11].

Quantitatively, magnetostriction is a change in elastic energy associated with a rotation of the magnetic moment. Or, conversely, a change in magnetic anisotropy energy due to a specified strain. Induced strain is related to the rotation of the magnetic moment, and thus, both saturate at some large field, resulting in the saturation magnetostriction ( $\lambda_s$ ) and saturation magnetization ( $M_s$ ) respectively. Materials with large magnetostriction also exhibit the reciprocal effect: a large change in magnetization due to induced strain [11]. The induced strain is mainly caused by rotation of the magnetic dipoles rather than domain wall motion.

The strain in any direction can be evaluated from the following expression

$$\frac{\Delta l}{l} = \lambda = \frac{3}{2}\lambda_{100} \left( \alpha_1^2\beta_1^2 + \alpha_2^2\beta_2^2 + \alpha_3^2\beta_3^2 - \frac{1}{3} \right) + 3\lambda_{111} (\alpha_1\alpha_2\beta_1\beta_2 + \alpha_1\alpha_3\beta_1\beta_3 + \alpha_2\alpha_3\beta_2\beta_3) \quad (1.33)$$

where  $(\alpha_1, \alpha_2, \alpha_3)$  specify the direction of the magnetization relative to the principal axes. In the case of a cubic crystal, the principal axes  $Z_1, Z_2, Z_3$  are along the cube edges  $[100], [010]$  and  $[001]$ . A second set of direction cosines  $(\beta_1, \beta_2, \beta_3)$  specify the direction  $Z'_3$  in which the strain  $x'_{33}$  is measured. The magnetostrictive coefficients  $\lambda_{100}$  and  $\lambda_{111}$  are the saturation strains measured along the specified crystal directions [21] given by

$$\lambda_{100} = \frac{2h_1}{3} \quad (1.34)$$

and

$$\lambda_{111} = \frac{h_2}{3} \quad (1.35)$$

with

$$h_1 = (N_{11} - N_{12})M_s^2 \quad (1.36)$$

and

$$h_2 = N_{44}M_s^2. \quad (1.37)$$

We have now established a mechanism which can induce a change in magnetic anisotropy energy by imposing a specified strain. As discussed in Section 1.1.2, the Kittel equation determines the FMR frequency and depends on a magnetic shape anisotropy term. Thus, we can influence this term by imposing a strain on a magnetostrictive material. By using a magnetostrictive material as the magnetic core of our microwave device, we can then, by imposing a strain, tune the FMR frequency of the device. In magnetoelectric composites, the strain is imposed by a piezoelectric element over which a voltage is applied. Understanding the underlying effect of piezoelectricity thus becomes important.

### 1.1.4.2 Piezoelectricity

The direct piezoelectric effect refers to the linear coupling between mechanical stress and electric polarization [21] as

$$P_i = d_{iJ}T_J. \quad (1.38)$$

The converse piezoelectric effect refers to the linear coupling between mechanical strain and applied electric field.

$$S_J = d_{Ji}E_i. \quad (1.39)$$

The notation conventions used are explained in Appendix B.2.

Of the materials already discovered to be piezoelectric, the complex oxides, and more specifically the perovskite piezoelectrics, have the largest piezoelectric coefficients. The perovskite crystal system is characterized by the general formula  $ABO_3$ , where A and B are cationic metals. A depiction of the perovskite structure is shown in Fig. 1.11(a). Generally perovskites can be characterized by  $BO_6$  octahedra surrounded by octahedrally coordinated A atoms. The overall stoichiometry becomes  $ABO_3$ .

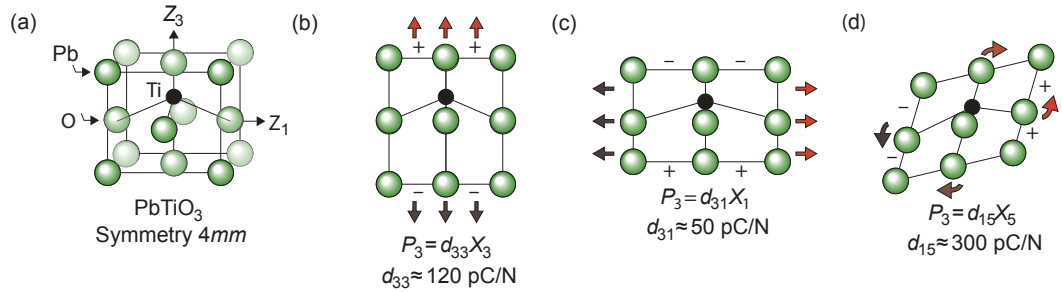


**Figure 1.11: Structure-Property Relations for the Intrinsic Piezoelectric Effect in  $PbTiO_3$**  - In the unstressed state there is an electric dipole associated with the off-center shift of the titanium atom. Under stress, this dipole can be increased ( $d_{33}$ ), decreased ( $d_{31}$ ), or tilted ( $d_{15}$ ). After Ref. [21]

While there are many oxide crystals that display a piezoelectric response, the best piezoelectrics tend to also be ferroelectric [10]. A ferroelectric is an insulating system with two or more discrete stable states of different nonzero electric polarization. A ferroelectric system can switch between states under influence of an applied electric field. This changes the relative energy of the states through the coupling of the field to the polarization [22]. Each of these states is crystallographically equivalent. In

ferroelectrics, these orientation states can be visualized as a double energy well symmetrically positioned around the centrosymmetric cation position. The applied electric field transitions the ion through the energy barrier, to one of the other orientation states. This changes the strain state of the system. It is this double well that leads to the high piezoelectric coefficients found in ferroelectric materials [10].

### 1.1.4.3 Magnetoelectric Effect

The magnetoelectric effect is defined as the occurrence of a polarization in response to a magnetic field, or conversely, the occurrence of a magnetization in response to an electric field. Although this effect has been observed in single phase materials, only composites systems have shown ME voltages at room temperature of significant magnitude for practical purposes. Thus we only consider composite systems consisting of a magnetostrictive and a piezoelectric phase. One then arrives at the ME susceptibility  $\alpha = \delta P / \delta H$  by taking the product of piezomagnetic deformation  $\delta z / \delta H$  with piezoelectric charge generation  $\delta Q / \delta z$ . Thus, an effective magnetic field is induced in the magnetostrictive phase by imposing a voltage-induced strain via the converse piezoelectric effect in the piezoelectric phase.

In ME materials, the induced polarization  $P$  is related to the applied magnetic field  $H$  as [23]

$$P_i = \alpha_{ij} H_j \quad (1.40)$$

and the induced magnetization  $M$  to the applied electric field  $E$  as

$$\mu_0 M_i = \alpha_{ji} E_j \quad (1.41)$$

where  $\alpha$  is the second rank ME-susceptibility tensor. Another important quantity is the ME voltage coefficient

$$\alpha_E = \delta E / \delta H \quad (1.42)$$

which is related to  $\alpha$  by

$$\alpha = \epsilon_0 \epsilon_r \alpha_E \quad (1.43)$$

where  $\epsilon_r$  is the relative permittivity of the material. Mostly  $\alpha_E$  is provided in  $\text{V} \cdot \text{cm}^{-1} \text{Oe}^{-1}$ .

These equations are valid for a magnetoelectric composite, regardless of the connectivity of its phases. There are a handful of ways to interconnect the phases of a

two-part composite [24]. Not all connectivity schemes are equally practical, or effective. We will focus on the laminate composites (with connectivity 2-2) for their proven high ME coefficients and ease of production.

### 1.1.4.4 Magnetolectric Laminate Composites

A bilayer or multilayer configuration for ME composites has several advantages over bulk composites and other composite connectivities.

1. The loss of polarization in bulk composites due to leakage currents can be overcome in layered structures
2. It is generally easier to apply large electric fields to thin film samples rather than bulk crystal or ceramic samples, because these require relatively smaller bias voltages
3. The piezoelectric phase can be poled to enhance the ME coupling
4. It is also possible to vary the poling and applied field directions to achieve maximum ME coupling
5. Different composites might experience line broadening effects for increased piezoelectric phase ratios
6. The planar thin-film geometry is more likely to be compatible with conventional deposition techniques employed in the IC industry compared to bulk and semi-monolithic alternatives

In order to obtain a better understanding as to what physical quantities are involved in ME coupling, the theory provided by Bichurin *et al.* [25] for low-frequency ME coupling, is considered. These authors consider a bilayer in the (1, 2) plane as can be seen in Fig. 1.12. The system is biased in a magnetic field  $H$  on which an AC magnetic field  $\delta H$  is superimposed. This gives rise to a pseudo-piezomagnetic effect (See Section 1.1.4.1) leading to an AC electric field  $\delta E$  across the piezoelectric phase. Bichurin *et al.* then estimate the ME voltage coefficient by solving the elastostatic and electrostatic equations.

Different field orientations can be considered, however, only one case is considered here:  $\alpha_{31}$ , for electric fields along direction 3 and magnetic fields along direction 1.

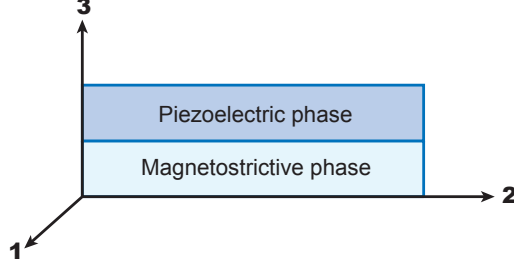


**Figure 1.12: Piezoelectric-Magnetostrictive Composite** - A bilayer of magnetostrictive and piezoelectric phases in the (1,2) plane with its thickness along axis 3. The bilayer is assumed to be poled with an electric field along axis 3. A bias magnetic field  $H$  and an AC magnetic field  $\delta H$  result in an AC electric field  $\delta E$  across the piezoelectric layer. Adapted from Ref. [26]

The value for  $\alpha_{33}$ , with both the magnetic and electric field oriented out-of-plane, is comparatively smaller. In fact, the maximum value for  $\alpha_{31}$  is five times larger than the maximum value for  $\alpha_{33}$ . Other orientations are not discussed due to their comparatively low ME coefficients. The ME voltage coefficient  $\alpha_{31}$  is given by [25]:

$$\alpha_{31} = \frac{\delta E_3}{\delta H_1} = \frac{-t(1-t)({}^m q_{11} + {}^m q_{21}){}^p d_{31}}{p\epsilon_{33}({}^m s_{12} + {}^m s_{11})t + p\epsilon_{33}({}^p s_{11} + {}^p s_{12})(1-t) - 2({}^p d_{31})^2(1-t)} \quad (1.44)$$

where  $m$  and  $p$  denote magnetostrictive and piezoelectric phases, respectively. The piezoelectric and piezomagnetic coupling coefficients are denoted by  $d$  and  $q$  respectively. The compliance coefficient is denoted by  $s$ ,  $\epsilon$  is the permittivity at constant stress,  $\mu$  is the tensor permeability and  ${}^p t$  and  ${}^m t$  are the thicknesses of the magnetostrictive and the piezoelectrics respectively. Lastly,  $t = {}^p t / ({}^p t + {}^m t)$  is the fractional thickness for the piezoelectric layer. Bichurin *et al.* show that, in the case of a NFO-PZT bilayer,  $\alpha_{31}$  is maximized for  $t = 0.4 - 0.6$  [25].

Although this not a general result, it is reasonable to assume, based on eq. (1.44), that for equal compliances for the piezoelectric and magnetostrictive phases, the optimal fractional thickness will lie around 0.5. It so happens that most candidate materials for ME bilayers (electroceramics, magnetostrictive ceramics and metals) have compliances in the range  $4-12 \cdot 10^{12} \text{ m}^2/\text{N}$  [27]. In general, maximizing the piezoelectric and magnetostrictive coefficients will maximize the magnetoelectric coupling.

In the area of magnetoelectric composites for microwave devices, the ME voltage is often deduced by the induced shift in FMR frequency. The induced strain in the

magnetostrictive material results in a shift in FMR frequency which can be measured as a function of applied voltage over the piezoelectric layer, see eq. (1.45).

$$\omega_{FMR} = \gamma \sqrt{(H_k + H_{DC} + \Delta H_{eff})(4\pi M_s + H_k + H_{DC} + \Delta H_{eff})} \quad (1.45)$$

Magnetoelectric composite materials consisting of both magnetic and ferroelectric phases with strong magnetoelectric coupling have led to many different classes of devices, one being, electrostatically tunable microwave devices [28–32]. These heterostructures have consisted of either piezoelectric substrates with thin polycrystalline ferro-/ferrimagnetic films or ferrite slabs epoxy bonded onto piezoelectric substrates.

Now that we have gone through the relevant theory and some of the cutting edge applications, we are ready to more accurately define the research goal.

## 1.2 Application Potential

Military and commercial applications for microwave components continue to demand smaller, more efficient, frequency-agile devices. As the mobile frequency spectrum grows increasingly crowded, the demands on battery life, size, weight and costs, increase. Adaptability to these ever changing conditions becomes beneficial. It is technologies that enable such adaptability that are becoming increasingly important [33].

Conventional magnetic field tuning of ferrite devices is often slow, bulky, noisy, and requires comparatively high power consumption for operation. Such components show no prospect of being miniaturized or integrated with semiconductor processing technologies. The main advantages of electric field tuning using ME materials are [34–36]:

1. **Increased tuning speed**
2. **Low power requirement** — When controlling an electrical field the energy is practically only consumed at the moment of switching.
3. **Low noise** — Arises inevitably when controlling the magnetic field.
4. **Isolation of circuits** — Circuits can be isolated without the need for simultaneously controlling electric and magnetic fields.

5. **Reduced size and weight**
6. **Simplify design and technology** – To advance towards integrated systems.
7. **Expand functional opportunities** – To develop essentially new devices.

### 1.3 Research Goals

The research goal, as defined by the US Army, was defined as:

*Demonstrate the feasibility of a magnetoelectrically tunable RF isolator at frequencies above 10 GHz.*

This was then recast by Aneve into a set of technical goals, formulated as:

1. Develop magnetoelectric thin film heterostructures with RF operation  $>10$  GHz
2. Develop microwave isolators with attractive figures of merit for military systems applicable to X and Ku bands
3. Optimize magnetoelectric thin films in order to design other crucial microwave passive elements, such as filters, phase shifters, circulators, and further develop a transistor integration friendly process

### 1.4 Original Research Proposal

In order to accurately and holistically reflect on this research project it's important to discuss its full context. The research was funded by the US Army under a STTR small business investment fund based on a proposal submitted by Aneve nanotechnologies. The writing of the proposal was done before my collaboration with Aneve nanotechnologies had started. For this reason, certain research avenues in this project were, from my point of view, predetermined.

In Phase I, CoFeB/PMN-PT heterostructure were set out to be studied. Preliminary results, as obtained by Prof. Kang Wang's research group, showed a tunability of  $\Delta f/f$  of 25% for this heterostructure. CoFeB is a well characterized system, used in the magnetic memory industry. The ideal magnetic material in a ME composite for isolator applications requires a low coercivity, low RF damping, high saturation magnetization

and high permeability. CoFeB meets most of these requirements. Furthermore CoFeB films show a high saturation magnetization of 20 kG [37] and a very high magnetostriction constant of 31 ppm [38]. The project aimed to develop isolators with attractive figures of merit for X and Ku bands.

### 1.5 Dissertation Organization

In Chapter 2 the design, fabrication and characterization of metallic magnetostatic surface wave isolators is documented. In Chapter 3 the deposition and characterization of various piezoelectric, magnetostrictive and magnetoelectric films is described. The results are presented and discussed. In Chapter 4 the results are presented of an optimization study of a PMN-PT sol-gel deposition process. In Chapter 5 progress towards a FEM model for ME RF devices is documented. The underlying theory is presented as well as modeling results for PMN-PT-based heterostructures. In Chapter 6 the conclusions to the research initiative are presented. And finally, in Chapter 7, a set of recommendations for future research is made.

## Chapter 2

# Metallic Magnetostatic Surface Wave Isolator

The first thrust in our efforts to develop a tunable IC compatible isolator involved the fabrication of metallic magnetostatic surface wave devices. Magnetostatic surface wave technology, also referred to as spin-wave propagation, was the basis of the proposal for which the project had been funded.

### 2.1 Introduction

Conventional, *ferrite-based*, MSW technology is based on the transduction of an RF signal into a magnetostatic wave. Through its slower propagation speed, the magnetostatic wave delays the propagation of the signal, until it is transduced back into an RF wave. Ferrimagnetic single-crystal films such as LPE-grown yttrium iron garnet (YIG) films have been the material of choice for the propagation of low loss magnetostatic waves. These films provide the physical basis for a large array of planar devices for signal identification, control, and processing at microwave frequencies [39]. Non-reciprocity in these films, can be introduced by exciting a pair of oppositely traveling magnetostatic *surface waves* (MSSW) and forcing their dispersion characteristics to diverge by subjecting them to different boundary conditions.

In recent years, spin-wave propagation in *metallic* ferromagnetic layers has been studied extensively in part due to its potential in high-speed and high-density magnetic data storage and potential applications in spin-wave-based logic devices. Recently, their

application has extended to nonreciprocal devices [40, 41]. Nonreciprocal effects have been inferred by employing the propagating spin wave spectroscopy (PSWS) technique where a pair of transmission lines are placed on top of a magnetic film acting as antennas for spin wave excitation and detection [40, 41]. The principle of a PSWS experiment is to produce a microwave field which is sufficiently nonuniform, so that it couples to spin waves with nonzero wave vectors. This is achieved by sending microwave current through a sufficiently narrow microwave antenna [42].

Since traditional ferrite-based nonreciprocal devices are not compatible with standard silicon integrated circuit (IC) technology [8], nonreciprocal behavior in IC-compatible magnetic materials can be of interest for the on-chip integration of these devices into microwave integrated circuits [40]. Surface spin waves on Ni-Fe [40] and Co-Ta-Zr [41], excited in a coupled microstrip structure, for example, have been shown to result in a nonreciprocal phase shift between the transmission lines. This could be exploited to realize nonreciprocal integrated passives on silicon. The main advantages of MSW technology are as follows [17, 39, 43]:

1. **Broad frequency range** - Can operate from 1 to 50 GHz limited from above only by high values of the steady magnetic field.
2. **Confinement of wave near surface** - This allows the wave energy to be tapped or otherwise modified while it is propagating. This is particularly interesting from a device point of view with tuning in mind.
3. **Bandwidths up to 1 GHz at microwave frequencies.**
4. **Comparatively low propagation losses.**
5. **Planar technology** - Compatible with presently available hybrid circuits and MMICs.
6. **Low, tunable group velocity** - Allows for compact devices and tunable delay respectively.
7. **Magnetic field tunable** - The frequency response of MSW devices can be tuned by varying the strength of the bias magnetic field.
8. **Effective excitation by transducers of simple design**

9. **Demonstrated Technology** - MSW Devices have already been used for realizing a class of microwave signal processing devices such as delay lines, phase shifters, resonators etc. with working frequencies from 1 to 50 GHz.

## 2.2 Background & Theory

The negative permeability shown by ferrite materials at frequencies exceeding the FMR frequency enables wave propagation in structures with arbitrary small cross section over limited frequency ranges [14]. These so called ‘slow branches’ — with small phase and group velocity — appear above the FMR frequency in the spectra of electromagnetic waves in waveguides containing ferromagnetic media. Solving boundary conditions for gyrotropic media using the magnetostatic approximation, the *magnetostatic waves* (MSW) and oscillations are obtained [17]. They are referred to as MSW since the electric-field contribution becomes negligibly small.

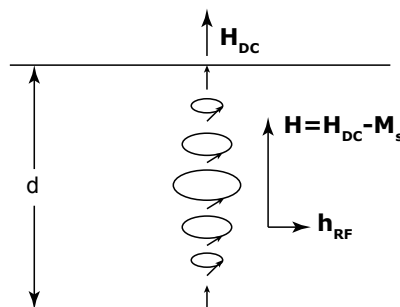


**Figure 2.1: Magnetostatic Modes** - Standing spin wave resonance across the thickness in a magnetic thin film. The precession cone angle of the magnetization has been exaggerated for clarity. After Ref. [44]

Electromagnetic waves in the magnetostatic approximation, whose wave numbers lie between those of electromagnetic waves and exchange spin waves, propagate in a magnetized ferromagnetic medium due to magnetic dipole interactions. This occurs when  $k_0 \ll k \ll \pi/a$ , where  $a$  is the spacing between spins. Consequently, these waves are also known as *dipolar spin waves* [44]. Moreover, the greater  $k$  is, the more applicable the magnetostatic approximation becomes [17].

Three pure MSW modes exist depending on the orientation of the bias magnetic field relative to the ferromagnetic film and the propagation direction. These modes are: Magnetostatic Surface Waves (MSSW), Magnetostatic Forward Volume Waves (MSFVW), and Magnetostatic Backward Volume Waves (MSBVW). These modes, and their field orientations are schematically depicted in Fig. 2.2(a). For a MSSW there is only a single propagating mode as opposed to a series of modes with thickness variations, as found with both volume waves. The phase and group velocities point in the same direction, making it a forward wave. Lastly, the wave amplitude decays exponentially starting from the film's surface rather than showing a periodic distribution throughout the thickness.

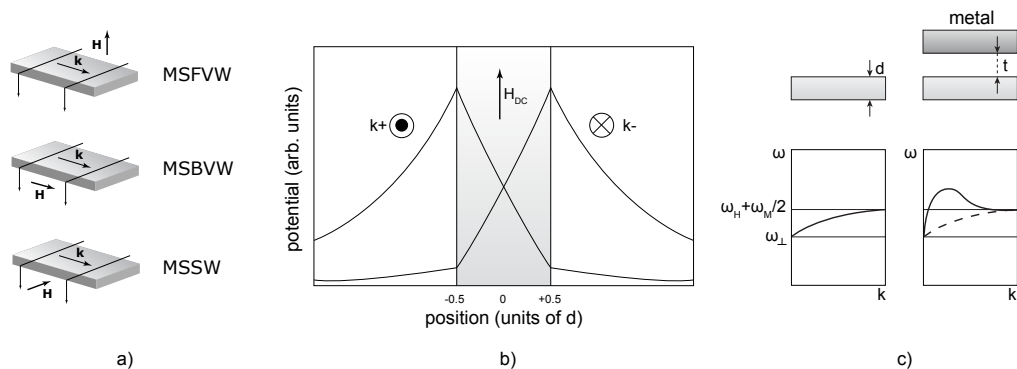


**Figure 2.2: Magnetostatic Wave Disperion** - a) The three magnetostatic modes. Adapted from Ref. [39]. b) Potential profiles for surface waves with  $s = \pm 1$ . Adapted from Ref. [44]. c) Frequencies of surface magnetostatic waves in a symmetric and asymmetrical structure containing a tangentially magnetized ferrite plate. Solid lines and dashed lines correspond to  $s = 1$  and  $s = -1$  respectively. Adapted from Ref. [17].

Oppositely propagating modes correspond to a field shift from one side of the film to the other (Fig. 2.2(b)). The dispersion of the spin-waves is not affected by this field shift. This is due to the symmetrical boundary conditions on either side of the film [44]. It has been shown [45] that when a tangentially magnetized ferromagnetic plate adjoins metal at one side ( $x = 0$ ) and air at the other side ( $x = d$ ), the boundary conditions become asymmetrical. The dispersion relation for the surface wave, in this case, becomes [17]:

$$\left(1 + 2\frac{\omega_H}{\omega_M} + 2s\frac{\omega}{\omega_M}\right) \frac{\omega_H + \omega_M - s\omega}{\omega_H + \omega_M + s\omega} = e^{-2kd} \quad (2.1)$$

The occurrence of terms involving  $s$  in the dispersion equation (eq. (2.1)) removes the directional degeneracy. Since  $s$  may take on the values  $+1$  or  $-1$  according to the propagation direction of the wave, its presence dictates different behavior for either direction (Fig. 2.2(c)).

Equation (2.1) has been employed by various authors when considering ferrite films and its validity has been confirmed experimentally. Khalili Amiri *et al.* [40] assume it to also be valid for metallic ferromagnetic films. However, as the authors acknowledge, little information exists regarding the nonreciprocal characteristics of spin-waves in thin, metallic magnetic elements [40].

We base our design on the results of Khalili Amiri *et al.* [40], and collaborated with the author. Khalili Amiri *et al.* use a shorted microstrip geometry on top of a laterally confined ferromagnetic layer. A schematic of the device structure is shown in Fig. 2.3. For a magnetization parallel to the antennas, an RF signal entering the antennas will excite magnetostatic surface spin waves on the upper or lower surface of the magnetic film, depending on their propagation direction [41]. A split in  $S_{21}$  and  $S_{12}$  becomes indicative of the split in dispersion curves. Based on the results shown by Khalili Amiri *et al.* [40], this geometry serves the purpose of obtaining nonreciprocity in a planar geometry. However, some additional considerations were made.

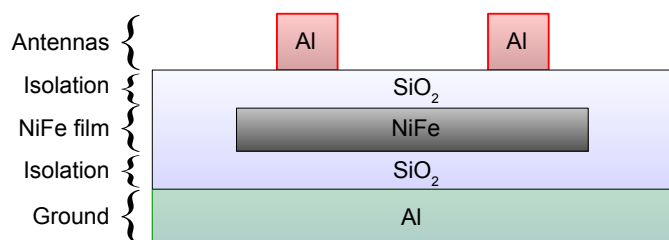


**Figure 2.3: MSSW Isolator Shorted Microstrip Structure** - Schematic of the device as fabricated by Khalili Amiri *et al.*

A microstrip geometry involves multiple deposition steps and at least one etch step for the vias. A coplanar waveguide (CPW) geometry, with one deposition step only, would offer design and fabrication simplicity. In the initial stages of the research, showing nonreciprocity as a proof of concept was the first, and main objective. This is why a coplanar waveguide geometry was investigated first. Furthermore, Khalili Amiri *et al.* [40] use laterally confined NiFe stripes, which require an additional deposition mask

as well as mask alignment. Again, to increase fabrication simplicity a ferromagnetic layer with full coverage was deposited. Therefore, unlike Khalili Amiri *et al.* [40] and Amiri *et al.* [41], multiple spin wave reflections due to the lateral confinement of the ferromagnetic stripes into account were not required to be taken into account.

At the time of fabricating this line of MSW isolators, access to the targeted magnetostrictive material CoFeB was inhibited. Thus, the focus was temporarily shifted to solely realizing nonreciprocal performance. Deposition of NiFe(80:20) was opted for, which Khalili Amiri *et al.* [40] presumably elected to use due to its high permeability. NiFe(80:20) however, has near-zero magnetostriction.

## 2.3 Coplanar Waveguide (GSSG)

The first device architecture that was attempted was a ground-signal-signal-ground (GSSG) coplanar waveguide geometry.

### 2.3.1 Materials & Methods

Fig. 2.4(a) shows the architecture for this device. The bias field was applied in parallel to the signal lines. The different isolator dimensions that were tested are listed in Table 2.1. NiFe films in a 80:20 composition were sputter deposited. The bottom SiO<sub>2</sub> thickness was kept constant, the top thickness was varied between 40 and 220 nm.

Signal Line Spacing ( $\mu\text{m}$ )	Width of Signal Lines ( $\mu\text{m}$ )			
80	10	20	30	40
100	10	20	30	40
150	10	20	30	40
200	10	20	30	40

**Table 2.1:** CPW GSSG Isolator Dimension Matrix

### 2.3.2 Results & Discussion

Fig. 2.4(b) shows a typical plot of S-parameters as a function of frequency. No difference is seen between S<sub>21</sub> and S<sub>12</sub> indicating the absence of nonreciprocity. Furthermore, the insertion loss is very high. Even if there had been nonreciprocity, the high insertion loss would have rendered it useless. Also, there was virtually no difference between the

## 2.3 Coplanar Waveguide (GSSG)

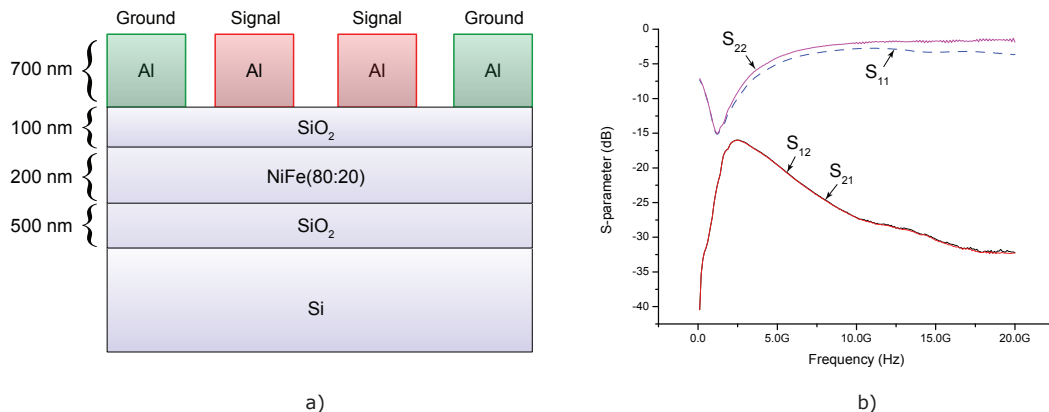


**Figure 2.4: Coplanar Waveguide (GSSG)** - a) Schematic of the device. b) S-parameters as a function of frequency for an oxide thickness of 40 nm and an applied bias of 100 Oe.

S-parameters with or without a bias field applied. For this reason no S-parameter plot under bias is included. All devices showed strikingly similar S-parameter plots, for all variations in structure geometry and layer thicknesses, therefore only one is included which is subjected to qualitative analysis.

The trough at approximately 1.5 GHz in  $S_{11}$  and  $S_{22}$  was initially interpreted to correspond to resonance losses. In retrospect this seems to be a mistake. Firstly, there was no reason to expect the FMR to be discernible for 0 applied bias, and the trough is visible for 0 applied bias. Secondly, there was no reason to expect FMR absorption to occur in  $S_{11}$  and  $S_{22}$  but not in  $S_{21}$  and  $S_{12}$ . The occurrence of FMR at a higher frequency (approximately 4.9 GHz) in the other device geometries confirmed this suspicion.

After being unable to demonstrate any nonreciprocity with this architecture the architecture used by Khalili Amiri *et al.* and the arguments that were used, were revisited. A new conclusion was reached that the architecture was not subjecting the ferromagnetic layer to the needed asymmetrical boundary conditions. As discussed in the theory section, magnetostatic surface waves on opposite sides of a ferromagnetic layer, experience different dispersion characteristics when they are subjected to asymmetrical boundary conditions. The excited spin-waves in a GSSG CPW geometry, however, can travel in between the antennas, while being subjected to *symmetrical* boundary conditions. This is illustrated with a closer look at the CPW structure in

Fig. 2.5. Only a slight asymmetry exists deriving from the fact that the spin-wave excited at the bottom of the ferromagnetic layer is further away from the antenna than the top layer, and thus the excitation energy would be somewhat weaker. For the most part, the spin-waves are expected to experience equal dispersion.

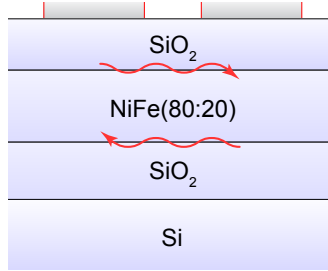


**Figure 2.5: Spin-Waves in Coplanar Waveguide (SGS)** - Spin-wave propagation in the CPW SGS geometry showing symmetrical boundary conditions.

## 2.4 Coplanar Waveguide (SGS)

In order to create asymmetrical boundary conditions a signal-ground-signal (SGS) CPW geometry was attempted. This structure was expected to subject the spin-waves traveling in between the signal lines to asymmetrical boundary conditions.

### 2.4.1 Materials & Methods

Fig. 2.6(a) shows the architecture for this device. The bias field was applied in parallel to the signal lines. The different isolator dimensions that were tested are listed in Table 2.2. NiFe films in a 80:20 composition were sputter deposited. Again, the bottom SiO<sub>2</sub> thickness was kept constant, the top thickness was varied between 40 and 220 nm.

Signal Line Spacing ( $\mu\text{m}$ )	Width of Signal Lines ( $\mu\text{m}$ )			
80	10	20	30	40
100	10	20	30	40
150	10	20	30	40
200	10	20	30	40

**Table 2.2:** CPW SGS Isolator Dimension Matrix

Unlike the GSSG CPW geometry, the spin-waves traveling on the surfaces of the ferromagnetic layer pass under the ground ground layer. The presence of the ground

## 2.4 Coplanar Waveguide (SGS)

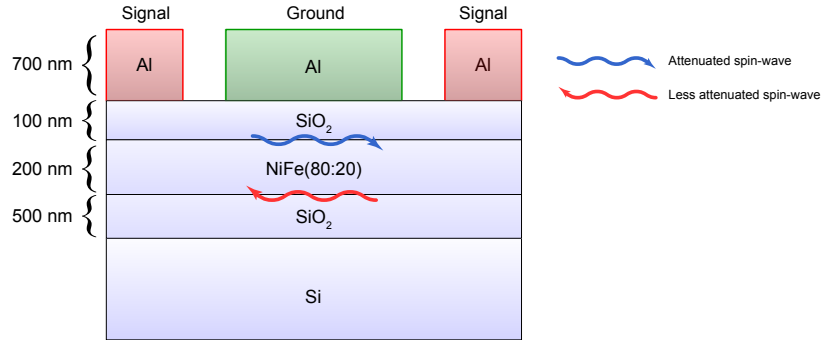


**Figure 2.6: Coplanar Waveguide (SGS) Device Geometry** - Schematic of the device geometry.

layer on one side of the ferromagnetic layer creates an asymmetrical boundary condition. On these grounds, nonreciprocity was expected.

### 2.4.2 Results & Discussion

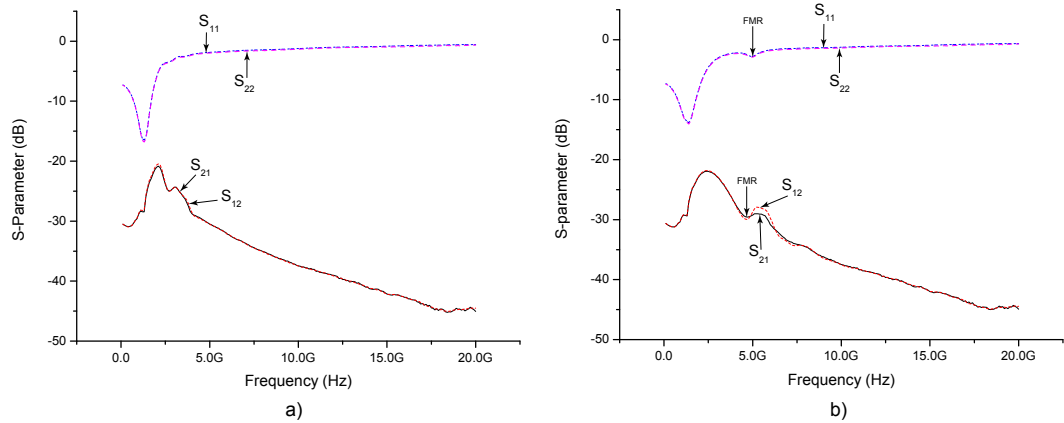


**Figure 2.7: S-Parameters for CPW S-G-S Geometry** - a) S-Parameters for an applied bias of 100 Oe. b) S-Parameters for an applied bias of 200 Oe

All the CPW SGS isolator structures showed comparable S-parameter behavior. Therefore one example is highlighted for qualitative analysis. No isolation was observed in the S-parameters. This was attributed to the large insertion losses which could overshadow any existing nonreciprocity.

When analyzing the data more carefully some additional information was deduced which was overlooked initially. At a bias field of 100 Oe no absorption due to FMR is discernible in the S-parameters. At approximately 4.9 GHz for an applied bias field of approximately 200 Oe we see a trough appear in all the S-parameters, corresponding to resonance absorption at the FMR. At frequencies slightly above the FMR we see some nonreciprocity, evidenced by a split in the  $S_{21}$  and  $S_{12}$  graphs. The isolation is estimated to be 2 dB at an insertion loss of 28 dB.

The level of insertion losses is higher for the SGS geometry in comparison to the GSSG geometry. The GSSG geometry, however, is the only structure showing isolation, albeit being too small to be useful.

## 2.5 Microstrip

In order to create asymmetrical boundary conditions a microstrip geometry was attempted. This structure was expected to subject the spin-waves traveling in between the signal lines to asymmetrical boundary conditions.

### 2.5.1 Materials & Methods

Fig. 2.8(a) shows the architecture for this device. The bias field is applied in parallel to the signal lines. The different isolator dimensions that were tested are listed in Table 2.3. NiFe films in a 80:20 composition were sputter deposited. Again, the bottom  $\text{SiO}_2$  thickness was kept constant, the top thickness was varied between 40 and 220 nm.

Signal Line Spacing ( $\mu\text{m}$ )	Width of Signal Lines ( $\mu\text{m}$ )			
80	10	20	30	40
100	10	20	30	40
150	10	20	30	40
200	10	20	30	40

**Table 2.3:** Microstrip Isolator Dimension Matrix

### 2.5.2 Results & Discussion

The microstrip isolator structures for the microstrip geometry, showed comparable S-parameter behavior for all thickness and geometric variations, which is represented in

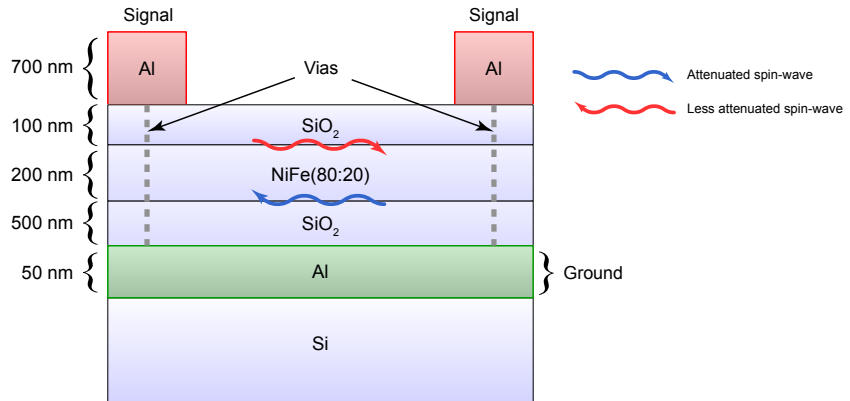


**Figure 2.8: Microstrip Device Geometry** - Schematic of the microstrip device geometry.

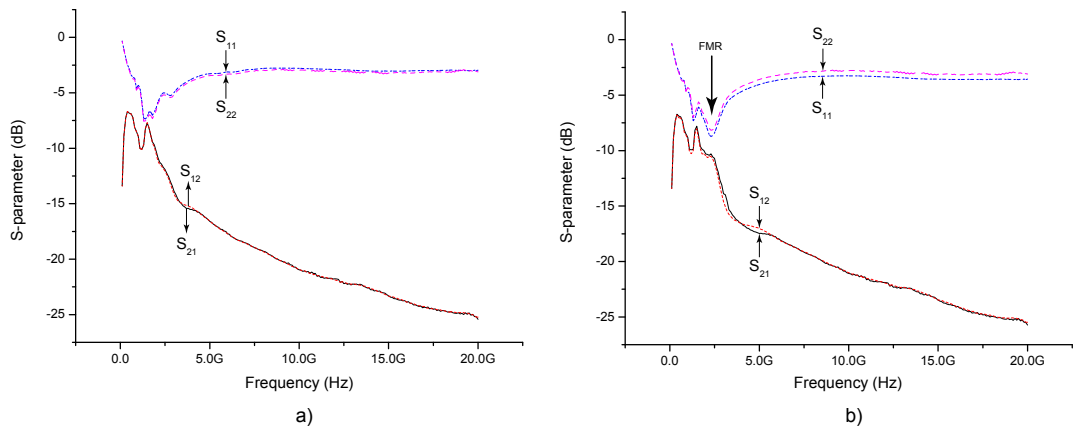


**Figure 2.9: S-parameters for Microstrip Geometry** - a) Microstrip geometry S-parameters with applied bias of 100 Oe. b) Microstrip geometry S-parameters with applied bias of 100 Oe

Fig. 2.9 (a) and (b). Therefore, again, only one graph is included for a qualitative discussion of the results.

The insertion losses in this case are slightly less dramatic than the CPW structures. Only a comparatively small field of 100 Oe is needed to show FMR absorption. One of the causes is likely the smaller insertion losses. In the case where a bias field is applied, some minor splitting of the  $S_{21}$  and  $S_{12}$  parameters occurs. When applying a bias, the split increases somewhat, at frequencies above FMR. Also visible is a splitting of  $S_{11}$  and  $S_{22}$  when applying a bias field. The cause of which is unknown.

## 2.6 Results & Discussion

Two of the isolator geometries show virtually no isolation. Only the SGS CPW geometry showed a very modest amount of isolation. It's hard to draw any conclusions from this, as there is very little literature available on either MSW technology on metallic ferromagnetic films or MSW technology for nonreciprocal devices. Khalili Amiri *et al.* [40] do not show or discuss measured S-parameters, thus making it hard to subject our results to critical analysis.

Although conduction losses are likely to have played a significant role in the high insertion losses seen in the isolator S-parameters, they are unlikely to be the only culprit. The microstrip structure was composed of similar materials and thicknesses as used by Khalili Amiri *et al.* [40], who do see noticeable nonreciprocity. This suggests that another loss mechanism might be at play. It's important to note that no formal impedance matching considerations were made. Thus, a certain degree of scattering is expected to occur at the input and output ports of the device. This, however, should only affect  $S_{11}$  and  $S_{22}$ .

Aside from conduction losses, the microstrip and coplanar waveguide structures will suffer from dielectric, magnetic, radiation and surface wave losses [15, 46]. These contributions have thus far been neglected, but the dielectric and magnetic losses in particular are known for their capacity to impact the insertion losses. With this in mind, the magnetic behavior of the NiFe was characterized using SQUID magnetometry and the resulting hysteresis loop is shown in Fig. 2.10. Although the low coercivity and relatively high saturation magnetization agree with expectations, the shape of the hysteresis loop is disconcerting. A loop with high squareness ( $M_r/M_s$ ) is expected, but a

value of 0.65 is observed. A region of linear increase in magnetization is observed in the non-hysteretic regime, between the hysteretic regime and the saturation magnetization. This is unexpected, and is an indication that the magnetic field has a ‘hard’ time saturating the film. A reduced squareness is often attributed to sub-optimal film quality. This sub-optimal behavior in the magnetic hysteresis loop raises the suspicion that magnetic losses might have played a larger role than was previously assumed.

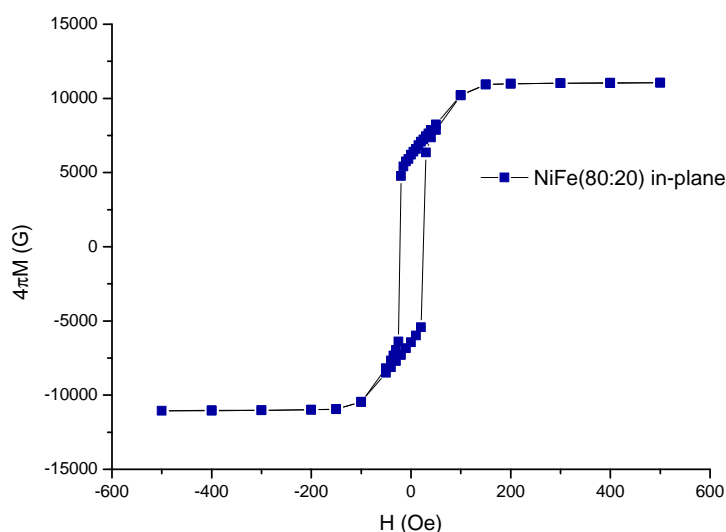


**Figure 2.10: SQUID measurement of NiFe** - SQUID measurement of NiFe showing an apparent difficulty in reaching saturation in the non-hysteretic regime.

A different, yet relevant resource, was later discovered. El-Sharawy and Guo [47] discuss the case of employing MSW technology for the purpose of a thin film isolator and fabricate such devices. They show an isolation of 30 dB, an insertion loss of 6 dB and a bandwidth of 1 GHz at 7.8 GHz. These results show promise for this type of isolator. Interestingly, the authors mention two reasons that MSSW transducers have not found an application in isolators or circulators: (1) high insertion losses and (2) low isolation due to electromagnetic coupling between the signal lines. The authors claim that the insertion loss can be further minimized by increasing film thickness or increasing the saturation magnetization of the magnetic film.

Based on our results and the very little work that has been done in the area, it is too soon to pass judgment on the feasibility of an MSW isolator. The feasibility of the

technology in terms of tunability — if reasonable levels of isolation could be achieved — *can* be evaluated.

If MSW technology utilizing metallic ferromagnetic films could provide a pathway to a monolithic isolator, would one be able to tune it through strain-mediated magnetoelectric coupling? Fetisov and Srinivasan has shown proof of concept in a bulk PZT/YIG composite phase shifter based on MSSW dispersion [35]. The author even remarks “*The phase shifter, due to non-reciprocal propagation of the surface MSW, can also function as a microwave isolator.*” Although the feasibility of many ferrite-based MSW devices has been demonstrated, Adam *et al.* notes that no applications have achieved the performance necessary to replace incumbent technology [14].

## 2.7 Conclusion

Three distinct architectures of thin film isolators were fabricated and tested while varying the signal line geometries and dielectric thickness. Two coplanar geometries and a microstrip geometry were fabricated. Only the CPW geometry with a SGS structure displayed a very modest amount nonreciprocity of 2 dB at an insertion loss of 28 dB. Figures which are far from desirable for an isolator.

Analogous to Amiri *et al.* [41] we conclude that there will be an optimal thickness for the observation of nonreciprocity, which will be determined by the skin depth at the frequency of operation. Khalili Amiri *et al.* show that the nonreciprocity vanishes for 50 nm NiFe(80:20) films as well as for 500 nm thick films. SQUID magnetometry on the NiFe films showed that its magnetic properties are sub-optimal, which might have contributed to the high insertion losses through magnetic losses.

A greater thickness allows for a greater volume of magnetized material which can, in principle, increase the nonreciprocal effect. Increased thicknesses, however, comes with increased eddy current losses. Thus, in order to increase the thickness of the magnetic film, the conductivity must be minimized. This is the conventional argument for using ferrites — insulating ferrimagnets — as microwave components. However, amorphous metals also show reduced conductivity while retaining their magnetic properties.

## Chapter 3

# Magnetolectric Composite Materials Characterization

### 3.1 Introduction

Magnetolectric laminate composites for RF applications have been realized by the growth of thin magnetic films on piezoelectric substrates [28, 48] and alternatively, by mechanically joining piezoelectric substrates with single crystal ferrite slabs [49]. The focus of this thesis has been on thin films and against that backdrop a heterostructure consisting of a piezoelectric substrate and a thin film of magnetic alloy  $\text{Co}_{80}\text{Fe}_{20}$  were grown and investigated on the one hand, and a piezoelectric substrate and an M-type Barium hexaferrite thin film on the other.

The differences between metallic magnetic thin films and ferrite thin films represents a critical trade-off in ME structures. Ferrites have conventionally been utilized for their favorable magnetic properties in conjunction with their low conductivities. This allows these materials to respond strongly to an external magnetic field while simultaneously exhibiting low losses at high frequencies. Metallic magnetic thin films — widely used in the memory industry — have only recently garnered attention for applications in microwave devices. Certain alloys display high permeabilities, satisfactory operating frequencies and easy deposition methods. The challenge to overcome has been the high conductivity attributed to metal films which causes significant losses at high frequencies.

A reduction in film thicknesses below the skin depth, is able to curb this effect by limiting the extent of eddy currents that are induced [50]. Additionally temperature

quenching during metal film deposition can thwart the crystal formation process within the film, eliciting an amorphous phase which shows comparatively low conductivity while maintaining most of its favorable magnetic properties [51].

Against this background both a metallic magnetic thin film as well as a ferrite thin film, deposited on a piezoelectric substrate, were investigated. The piezoelectric substrate is the common denominator in the investigated structures. Due, in part to this central role, and in part due to its remarkable electric behavior, it merits its own section.

### 3.1.1 PMN-PT (68:32) Single Crystal Substrates

The piezoelectric substrates that were used are single crystal  $[\text{Pb}(\text{Mg}_{1/3}\text{Nb}_{2/3})\text{O}_3]_{1-x}-[\text{PbTiO}_3]_x$  (PMN-PT) ( $x \approx 32\%$ ). Recently Wu *et al.* [52] reported that these single crystals, when cut and poled in the (011) orientation, exhibit a giant strain jump during the electric field driven polarization reorientation process (Fig. 3.1(b)). In fact, two permanent, and reversible, strain states can be achieved by applying a specified electric field. These remnant strains in (011) PMN-PT substrates were utilized to achieve reversible and permanent magnetic anisotropy changes in a Ni/PMN-PT heterostructure [53].

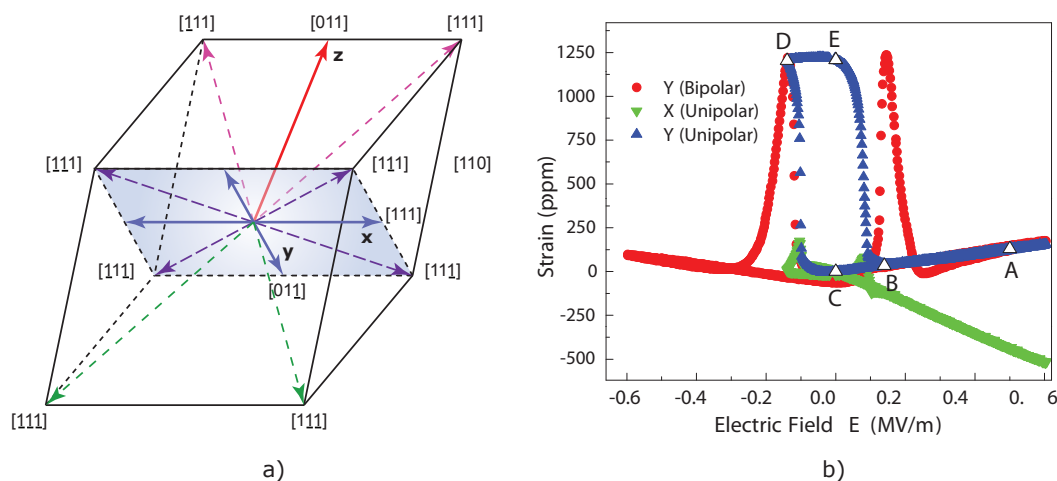


**Figure 3.1: PMN-PT Crystal Polarization Orientations and Strain Curve - a)** Polarization orientations for rhombohedral PMN-PT, after Ref. [52] **b)** Strain-field curve for PMN-PT (68:32) single crystal substrates. Taken from Ref. [53]

Wu *et al.* [52], in an attempt to explain the unexpected strain jump, treat the PMN-PT (68:32) crystal as exhibiting rhombohedral symmetry, and use the corresponding spontaneous polarization directions to explain the sudden spike in the field-strain behavior. Fig. 3.1(a) illustrates the rhombohedral crystal structure of  $\langle 011 \rangle$  PMN-PT with eight possible  $\langle 111 \rangle$  spontaneous polarization directions.

Figure 3.1(b) shows the corresponding bipolar strain measured along the  $y$ -direction as well as unipolar strain curves measured along  $x$  and  $y$ . The bipolar strain vs E-field curve along  $y$  shown in Fig. 3.1(b) indicates a large nonlinear strain jump, which is attributed to non-180° ferroelectric polarization reorientation [52]. For specimens poled along the  $[011]$  direction, there are roughly equal volume fractions of two crystal variants with polarizations aligned along the two  $[\underline{1}11]$  and  $[111]$  variants. When a reversed electric field is applied, the strain and electric displacement curves suggest that the polarizations first reorient by non-180° reorientation to four possible in-plane  $\langle 111 \rangle$  directions.

This non-180° polarization reorientation produces a large jump in the strain along the  $y$  direction. With further increases in the reversed electric field, the polarizations undergo another non-180° polarization reorientation to the two  $[111]$  and  $[\underline{1}11]$  variants. By operating at the right field, it is possible to take advantage of the first non-180° polarization reorientation to produce two reversible and permanent remnant strain states having significantly different strain values.

Another important feature of the (011) PMN-PT substrates is their large and oppositely oriented  $d_{31}$  and  $d_{32}$  coefficients. This leads to an anisotropic induced in-plane strain. Research in magnetoelectric coupling of laminate composites has predominantly focused on isotropic strains. Anisotropic strains allow for giant ME coefficients. Lou *et al.* [54] recognized this benefit and Lou *et al.* [28], using the magnetoelastic relations, cast it into the following formula

$$\Delta H = 3\lambda_s Y d_{eff} E / M_s \quad (3.1)$$

where  $Y$  is Young's modulus of the film,  $E$  is the electric field applied to the PMN-PT single crystal, and  $d_{eff}$  is the effective piezoelectric coefficient of the PMN-PT single

---

## 3.2 CoFe/PMN-PT Thin Film on Substrate Heterostructure

crystal which can be calculated as

$$d_{eff} = \frac{\nu d_{32} + d_{31}}{1 - \nu^2} - \frac{\nu d_{31} + d_{32}}{1 - \nu^2} = \frac{d_{31} - d_{32}}{1 + \nu} \quad (3.2)$$

where  $\nu$  is the Poisson's ratio of the magnetic film. The merits of maximizing the difference between  $d_{31}$  and  $d_{32}$  can be seen from eqs. (3.1) and (3.2).

The (011) PMN-PT single crystal ferroelectrics were manufactured and prepared by Atom Optics Co., LTD. (Shanghai, China) using the modified Bridgman growth method. The dimensions of the substrates were  $10 \times 5 \times 0.5$  mm with  $\langle 011 \rangle$  orientation along the thickness. Both surfaces were polished and provide a surface roughness less than  $30 \text{ \AA}$  [52]. 10 nm Ti and 50 nm Pt layers were deposited on one side as bottom electrode.

## 3.2 CoFe/PMN-PT Thin Film on Substrate Heterostructure

The initial aim of the research initiative was to use the CoFeB system as the magnetostrictive component in the ME heterostructure. CoFeB, however, was not available for deposition at the time due to the unavailability of the B target in the sputtering chamber. A Co-Fe alloy was selected as an alternative, where the choice for composition was based on maximizing the relevant material parameters.

### 3.2.1 Introduction

CoFe in a composition of (80:20) was selected. As can be seen from Fig. 3.2(b) the magnetocrystalline anisotropy decreases in the CoFe system for increasing Co content. Since a small coercivity is desirable for easy magnetization switching, and magnetocrystalline anisotropy is related to the coercive field, selecting a high cobalt content would minimize the coercive field. Literature values for  $\text{Co}_{80}\text{Fe}_{20}$  confirm this trend for higher values of Co [55].

As can be seen in Fig. 3.2(a), increasing the cobalt content in the CoFe system also decreases the saturation magnetization. The saturation magnetization plays part in determining the FMR frequency, which dictates the operation frequency. Since the focus of this research initiative was on frequencies exceeding 10 GHz, a comparatively

### 3.2 CoFe/PMN-PT Thin Film on Substrate Heterostructure

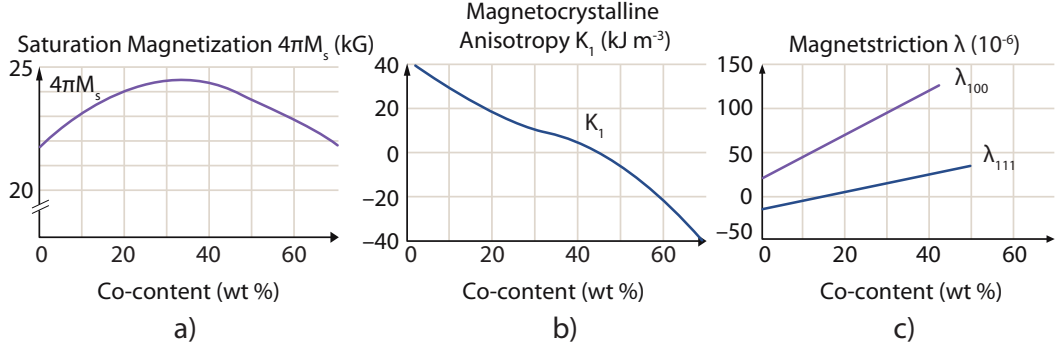


**Figure 3.2: Material Parameters as a Function of Cobalt Content in CoFe -**  
**a)** Saturation magnetization ( $M_s$ ) as a function of Co-content in the CoFe system. Taken from ref. [51]. **b)** Magnetocrystalline Anisotropy constant  $K_1$  as a function of Co-content in the CoFe system. Taken from ref. [51] **c)** Magnetostriction as a function of Co-content in the CoFe system. Taken from ref. [51]

small saturation magnetization was considered undesirable. The data in Fig. 3.2(a) does not cover Co-contents exceeding 60%. Values obtained from the literature fill in this information and point to a satisfactory high saturation magnetization of 17.4 kG for  $\text{Co}_{80}\text{Fe}_{20}$  [55].

For a film with the c-axis in-plane in the cgs system the FMR frequency is given by

$$f_{FMR} = |\gamma| \sqrt{(H + H_k)(H + H_k + 4\pi M_s)} \quad (3.3)$$

For self biased operation ( $H = 0$ ), using an  $H_k$  of 50 Oe [56], a saturation magnetization of 17.4 kG [55] and an absolute value for  $\gamma$  of 2.8 MHz/Oe eq. (3.3) gives an  $f_{FMR}$  of 9.3 GHz. Provided the film exhibits high squareness ratios, a self-biased device could potentially be obtained with an operation frequency in the 10 GHz range. Additionally, only a comparatively small bias field would be needed to reach higher operation frequencies. Although the saturation magnetization tends to suffer from increased Co-content, the magnetostriction coefficients tend to increase monotonically as can be seen in Fig. 3.2. Literature values confirm this trend with reported magnetostriction of 30 ppm for  $\text{Co}_{80}\text{Fe}_{20}$  [57].

In summary,  $\text{Co}_{80}\text{Fe}_{20}$  is a ferromagnetic alloy with a high saturation magnetization ( $4\pi M_s$ ) of 17.4 kG [55], a low coercivity ( $H_c$ ) of 20 Oe [55], and a comparatively high saturation magnetostriction ( $\lambda_s$ ) of 30 ppm [57]. The coercivity of CoFe has been shown

### 3.2 CoFe/PMN-PT Thin Film on Substrate Heterostructure

to strongly depend on the substrate texture [58, 59], film thickness and background pressure [60].

#### 3.2.2 Materials & Methods

CoFe depositions were carried out by Professor Krivorotov's group at the University of California Irvine. The  $\text{Co}_{80}\text{Fe}_{20}$  alloy was deposited using cosputtering with a Co and a Fe target under low Argon pressure. Magnetic hysteresis curves were obtained using SQUID magnetometry and longitudinal mode magneto-optical Kerr effect (MOKE) magnetometry.

#### 3.2.3 Results & Discussion

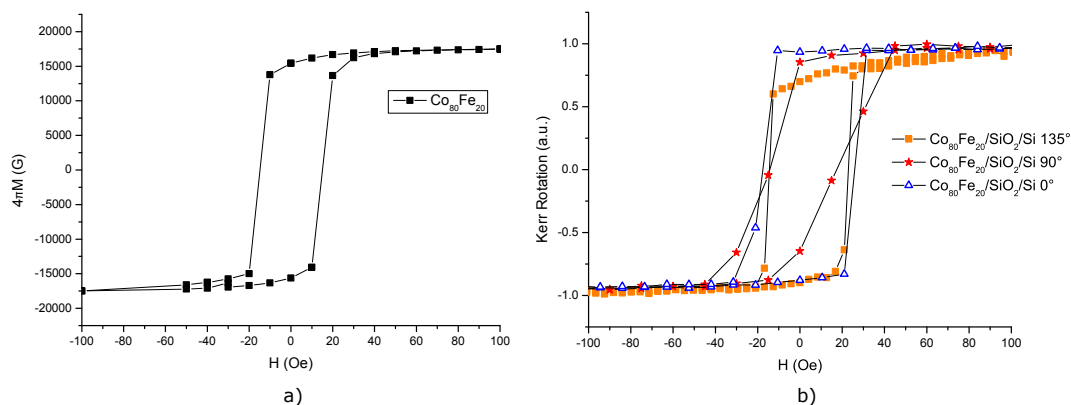


**Figure 3.3: In-Plane Magnetic Characterization of  $\text{Co}_{80}\text{Fe}_{20}$  - a)**  $\text{Co}_{80}\text{Fe}_{20}$  on Si SQUID measurement **b)** In-Plane MOKE Measurements on  $\text{Co}_{80}\text{Fe}_{20}$  for  $0^\circ$ ,  $90^\circ$  and  $135^\circ$ .

The saturation magnetization  $M_s$  was measured to be approximately 17.2 kG (Fig. 3.3), which corresponds reasonably well with literature values [55]. The coercive field ( $H_c$ ) was determined to be approximately 30 Oe (Fig. 3.3). This is higher than values reported in the literature of 20 Oe [55] and might be attributable to the coercive field's sensitivity to the growth template, background pressure or thickness of the layer.

Polycrystalline randomly oriented ferromagnetic films tend to have in-plane easy axes due to the dominating shape anisotropy of a thin film. This was also expected for the 500 nm  $\text{Co}_{80}\text{Fe}_{20}/\text{SiO}_2/\text{Si}$  film. The in-plane magnetic hysteresis loop was measured using MOKE. The sample was positioned at an arbitrary angle to the bias magnetic field and rotated from the starting position by  $90^\circ$  and  $135^\circ$ . The resulting hysteresis

### 3.2 CoFe/PMN-PT Thin Film on Substrate Heterostructure

curves are shown in Fig. 3.3(b). The squareness ratios ( $M_r/M_s$ ) for  $0^\circ$ ,  $90^\circ$  and  $135^\circ$  are 0.96, 0.86 and 0.74 respectively. Although the behavior could arguably still be characterized as easy-axis behavior, this does go against the expectation of in-plane isotropic magnetic behavior. A possible explanation could be a preferential orientation in the polycrystalline CoFe. The magnetic behavior of  $\text{Co}_{50}\text{Fe}_{50}$  thin films has been found to be highly sensitive to the substrate texture [58]. No template layer was used for CoFe as it was deposited directly onto the PMN-PT substrate. A preference for a certain orientation at the substrate surface could have transferred to the CoFe film, causing anisotropic magnetic in-plane behavior.

The out-of-plane magnetic hysteresis loop for the  $\text{Co}_{80}\text{Fe}_{20}/\text{SiO}_2/\text{Si}$  structure was not obtained. However, observation of a hard axis out-of-plane could have strengthened the argument for observation of an in-plane easy axis. Additionally, the hard axis hysteresis curve could be used to determine the anisotropy field.

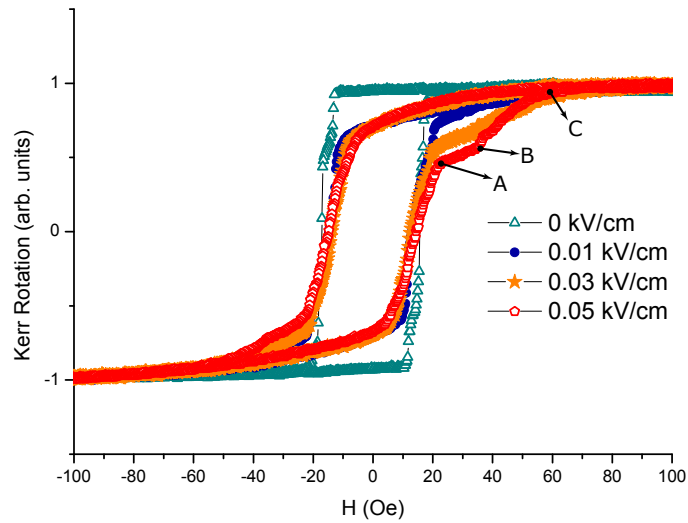


**Figure 3.4: CoFe on PMN-PT** - Magnetic hysteresis curves for a CoFe film for different applied electric fields.

Magnetoelectric coupling is demonstrated for a 500 nm polycrystalline  $\text{Co}_{80}\text{Fe}_{20}$  on Pt/Ti/PMN-PT heterostructure. The CoFe layer functioned as top electrode. For 0 applied bias the squareness ratio ( $M_r/M_s$ ) is 0.98. For an applied electric field of 0.01 kV/cm  $M_r/M_s$  becomes 0.73. Increasing the field beyond 0.01 kV/cm, however,

### 3.2 CoFe/PMN-PT Thin Film on Substrate Heterostructure

---

no longer affects the squareness. The only variation in the hysteresis behavior that is observed for these fields is the asymmetric behavior that appears in the transitioning segment from linear to nonlinear behavior. This induced change in behavior is more clearly visible for positive fields than for negative fields.

Taking a closer look at hysteresis loop for 0.05 kV/cm, more can be said about this behavior. Starting from 0 bias, for increasing positive fields the magnetization process starts off as a quasi-linear process, expected to correspond with domain rotation. These domain rotation contributions are also likely to cause the linear behavior seen for fields of 0.01–0.03 kV/cm, albeit at a slightly slower rate of magnetization. At point *A*, denoted in Fig. 3.4, a drastic decrease in magnetization rate is observed. This rate persist until point *B* (Fig. 3.4), at which a slight increase in magnetization rate is observed as the curve approaches saturation values at *C* (Fig. 3.4). The anomalous behavior seen in going from *A–B–C* is also seen for electric fields of 0.01–0.03 kV/cm, however, the effect is less pronounced.

As the magnetization process approaches the nonlinear regime — said differently, as the contributions to a change magnetization shift from predominantly domain rotation to predominantly domain movement — the rate of magnetization drops.

The odd thing about this is that the magnetic hysteresis curve is expected to be symmetrical about the origin — a positive and negative bias field will generally induce the same *magnitude* of magnetization, albeit in a different direction. This, however, is not the case here. This, and the fact that this behavior is only observed for the highest applied electric fields, makes it less likely to be an intrinsic property of the material. More likely, this behavior is caused by some artifact in the film.

A possible explanation could be that certain areas of the film are harder to saturate than others. Based on the hysteresis curve for 0 kV/cm, an unstrained region of the film, for instance, would reach saturation around 20 Oe. This coincidentally lies close to point *A* in Fig. 3.4. If one region of the film were to saturate before the rest of the film, its contribution to the magnetization rate would vanish, thereby dropping the overall magnetization rate. An unstrained region could have been the result of the very poor adhesion of the CoFe layer to the substrate. This was also observed experimentally. Although this seems a plausible explanation for the behavior for *A–B*, it fails to explain the *increased* magnetization rate for *B–C*.

#### 3.2.4 Conclusion

$\text{Co}_{80}\text{Fe}_{20}$  was grown on (111) Si substrates and (011) oriented poled PMN-PT substrates. An easy axis in-plane was expected, but reduced squareness values suggest there might be some magnetic anisotropy in-plane. CoFe compositions are known to show sensitivity in their coercive fields due to substrate texture, film thickness and Argon pressure during growth.

Magnetoelectric coupling is shown for a  $\text{Co}_{80}\text{Fe}_{20}/(011)\text{PMN-PT}$  heterostructure. The  $M_r/M_s$  ratio was reduced by 26% by an applied electric field of 0.01 kV/cm. Asymmetric behavior was observed in the magnetic hysteresis loop which increased in magnitude for increasing electric fields. This is likely due to a measurement artefact, possibly related to an unstrained area of the film.

Film adhesion was overlooked, but it will play a significant role in optimizing the ME coupling in laminate composites. The challenge will be to ensure good film adhesion while maintaining the desired crystal texture and material properties.

Based on the reports in the literature, supplemented with these obtained results,  $\text{Co}_{80}\text{Fe}_{20}$  is a reasonable candidate material for the magnetostrictive phase in a ME heterostructure. However, the CoFeB system remains an even better choice. The  $\text{Co}_{60}\text{Fe}_{20}\text{B}_{20}$  system provides higher saturation magnetization ( $M_s = 20\text{kG}$  [37]), higher anisotropy fields ( $H_k = 400\text{-}700\text{ Oe}$  [38]) and higher magnetostriction ( $\lambda_s = 31\text{ ppm}$  [38]). And, importantly, these physical quantities only diminish slightly for the amorphous phase. These quantities represent a higher saturation magnetization alternative to the increasingly popular amorphous FeGaB system ( $M_s = 11\text{-}15\text{ kG}$  [54],  $\lambda_s = 70\text{ ppm}$  [28]), albeit exhibiting lower saturation magnetostriction.

### 3.3 BaM/PMN-PT Thin Film on Substrate Heterostructure

Conventional ferrites — typically garnets — have characteristically low magnetocrystalline anisotropy and low saturation magnetization. This translates into comparatively low FMR frequencies and therefore low operation frequencies. This limits YIG-based devices to the 10-18 GHz range [61].

To reach higher frequencies, M-type barium hexagonal ferrite  $\text{BaFe}_{12}\text{O}_{19}$  (BaM) films have been used as an alternative to the garnets. BaM films can be processed to

### 3.3 BaM/PMN-PT Thin Film on Substrate Heterostructure

possess extremely high magnetocrystalline anisotropy fields ( $H_k$ ) up to 17,000 Oe. The high anisotropy fields stem from the alignment of the easy axis with the crystallographic  $c$ -axis and the ability to process BaM films with a high degree of crystal texture and preferential magnetic anisotropy [8]. This places the zero-field FMR frequency of BaM around 36 GHz. This enables devices that are based on this hexagonal ferrite to operate at frequencies as high as the Ku band for below resonance operations and beyond the Q band for above resonance operations [8].

BaM has the magnetoplumbite structure (space group  $Pb3/mmc$ ). It consists of 10 oxygen layers in which which four successive layers — each containing four oxygen anions — are followed by a fifth layer containing three anions and a Ba cation [8]. (see Fig. 3.5(a)).

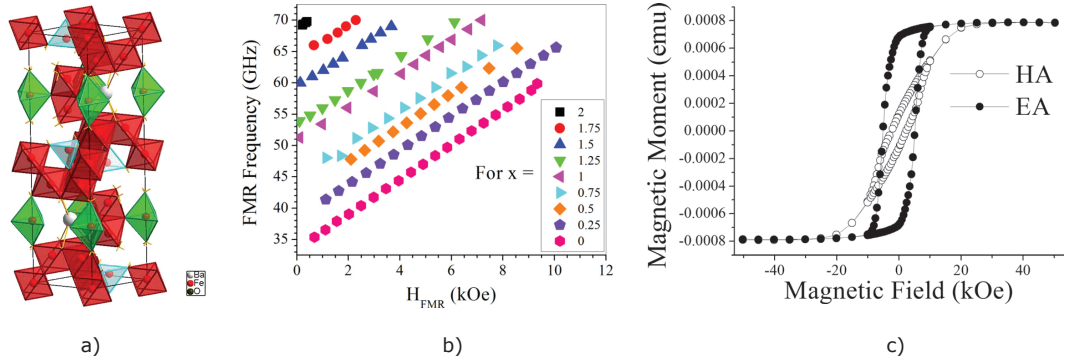


**Figure 3.5: BaM Structure, Doping Effects and Magnetic Hysteresis - a)** BaM magnetoplumbite structure. **b)** Applied field vs. FMR frequency for different Al doping concentrations of BaM. Taken from Ref. [62]. **c)** Magnetic hysteresis loop for BaM(0.75)Al taken from Ref. [62].

High squareness ratios, which are a hallmark of pristine crystal quality, can also be achieved. BaM films with high remnant magnetization have been processed, which allows for self-biased operation and low field frequency tuning (See Fig. 3.5(c)).

The remarkable versatility of the BaM system is exemplified by the increase or decrease of the anisotropy field ( $H_k$ ) — and thereby the FMR — that can be achieved through doping. Substitution of Sc or In for Fe reduces  $H_k$ , whereas Al and Ga substitutions allow for an increase. Use of BaM and its substitutional systems thus provides the capacity for device applications from 1 to 100 GHz [8].

### 3.3 BaM/PMN-PT Thin Film on Substrate Heterostructure

---

A variety of deposition techniques have been used to deposit BaM films. These include pulsed laser deposition [63], liquid phase epitaxy [64], RF magnetron sputtering [65], molecular beam epitaxy [66], chemical vapor deposition [67], screen printing [68] and more recently metallo-organic decomposition [62, 69]. The feasibility of BaM films for device applications has been proven through device applications such as phase shifters [70], filters [71] — and more importantly — circulators [72] and isolators [73].

BaM film quality is frequently deduced from the squareness ratio ( $M_r/M_s$ ) and the linewidth  $\Delta H_{FMR}$ . The highest quality films, expressed in these criteria, were grown using PLD and sputtering on single crystal sapphire ( $\alpha\text{-Al}_2\text{O}_3$ ).

The growth of BaM films with the crystallographic  $c$ -axis aligned perpendicular to the film plane leads to perpendicular magnetic anisotropy: a requirement for conventional circulator and isolator devices and perpendicular magnetic storage media. Certain device applications, however, require the growth of BaM films on conductive substrates or with in-plane magnetic anisotropy.

In coupled-line and stripline-type devices, for example, a ground plane is needed underneath the active layer. Nie *et al.* [69] succeeded in the fabrication of highly textured out-of-plane  $c$ -axis oriented BaM thin films on platinum (Pt) electrodes through metallo-organic decomposition (MOD) techniques. Harward *et al.* [62] expanded on this and were able to grow high quality BaM films with explicit control over the doping concentration of Al. FMR tuning as a function of Al doping was the result.

The work by Nie *et al.* [69] and Harward *et al.* [62] clearly demonstrates the feasibility of the use of MOD techniques to fabricate on metallic electrodes BaM thin films with high  $M_r/M_s$  ratios and reasonable low losses. In comparison to high-end techniques such as PLD, MOD it is relatively inexpensive and can ensure film homogeneity over large surfaces.

#### 3.3.1 Methods & Materials

The BaM films were grown by Prof. Celinski's group at the University of Colorado, Colorado Springs in a collaborative effort with Aneve Nanotechnologies.

The films were prepared on 300 nm-thick (111)-oriented Pt layers which were evaporated on Si wafers. The fabrication processes include three main steps, (1) spin coating of a precursor onto a substrate, (2) annealing at different temperatures (150-450° C) to remove solvents and realize metallo-organic decomposition, and (3) rapid thermal

### 3.3 BaM/PMN-PT Thin Film on Substrate Heterostructure

---

annealing (RTA) at high temperatures (850-900° C) to facilitate the formation of a proper structure. It was found that the RTA step was very critical for the realization of high-quality BaM films. It was demonstrated, for example, that the temperature significantly affects the crystalline structure of the film, and the type of background gas strongly affects both the remnant magnetization and FMR linewidth.

Magnetic moment data (emu) was converted to  $4\pi M_s$  (G) values by estimating the volume of the magnetic film. The volume was estimated by multiplying an estimate of the thickness by the film area, which was determined by photographing the sample and counting pixels. All magnetic hysteresis curves were obtained using a SQUID magnetometer.

#### 3.3.2 Results & Discussion

The measured ( $M_r/M_s$ ) ratio is 0.89, which is higher than that measured 0.85 by Harward *et al.* [62] for BaM(0.75)Al. Absolute magnetic moment is measured by Harward *et al.* [62] and therefore only a qualitative comparison can be made with the volumetric data in Fig. 3.6. The shape of the hysteresis loops, however, are very similar. From Fig. 3.6 it can be seen that the out-of-plane magnetic hysteresis loop corresponds to an easy axis and the in-plane loop corresponds to a hard axis. This is consistent with the expectation of a highly textured BaM film with its  $c$ -axis in an out-of-plane orientation.

$4\pi M_s$  is determined to be 5490 G, which is somewhat higher than that reported for single crystal BaM [74].  $H_c$  is approximately 5000 Oe, corresponding reasonably well with the coercive field measured by Harward *et al.* [62] for BaM(0.75)Al.

BaM thin films were also grown on PMN-PT (68:32) substrates with a Ti (10 nm) and a Pt (90 nm) coating. The films were characterized by atomic force microscopy (AFM), the result of which is shown in Fig. 3.7(b) and is compared with the AFM images obtained by Nie *et al.* [69] in Fig. 3.7(a).

Magnetic hysteresis curves for out-of-plane orientation and in-plane orientation were obtained and are displayed in Fig. 3.7. As is evident, from Fig. 3.7, both in-plane and out-of-plane orientations fail to saturate within at a magnitude of 30,000 Oe applied bias. This is surprising.

Morphological characterization, using scanning electron microscopy (SEM), could provide more insight in the film formation process. XRD analysis of the film could be

### 3.3 BaM/PMN-PT Thin Film on Substrate Heterostructure

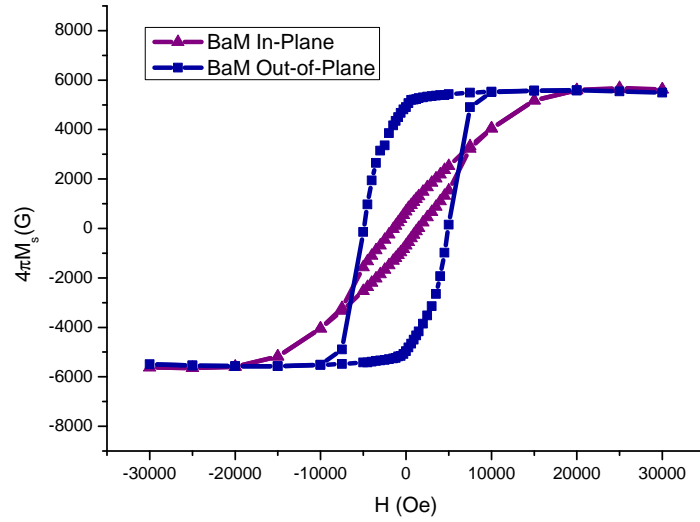


**Figure 3.6: Magnetic Hysteresis for  $\text{BaAl}_{0.25}\text{Fe}_{11.75}\text{O}_{19}$**  - Magnetic Hysteresis for a 200 nm  $\text{BaAl}_{0.25}\text{Fe}_{11.75}\text{O}_{19}$  film at room temperature with the applied DC magnetic field along the easy axis (green squares) and along the hard axis (purple triangles).

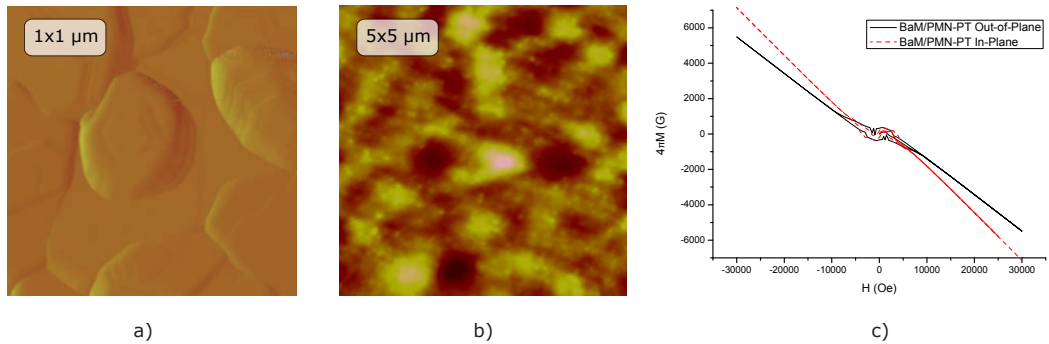


**Figure 3.7: Structural and Magnetic Characterization of a BaM thin film on PMN-PT** - a) AFM microscopy of BaM on Pt/Si as obtained by Nie *et al.* [69]. b) Obtained height profile using AFM microscopy of BaM on Pt/Ti/PMN-PT(68:32). c) Magnetic hysteresis loop of in-plane and out-of-plane BaM/Pt/Ti/PMN-PT structures as obtained by SQUID magnetometry.

### 3.3 BaM/PMN-PT Thin Film on Substrate Heterostructure

---

used to determine the crystal phases and determine the presence of BaM. Additionally the XRD profiles can be compared with data from the literature.

#### 3.3.3 Conclusion

A 200 nm BaM film, grown on a highly (111) oriented Pt template through metallo-organic decomposition was characterized using a SQUID magnetometer. The magnetic hysteresis curve was obtained for in-plane and out-of-plane orientations. Based on the high squareness ratio obtained for the out-of-plane orientation, the film is suspected to be highly textured with the crystallographic  $c$ -axis out-of-plane.

Pt/Ti coated PMN-PT (68:32) substrates were used as substrates for metallo-organic decomposition growth of BaM. The AFM results reveal, seemingly out-of-focus, clusters, which are similar in size as the grains for BaM films obtained by [69] Nie *et al.*. This suggests a lower level of atomic definition was achieved. The magnetic hysteresis loop obtained indicates a linear magnetic response between -30,000 and 30,000 Oe, with very little hysteresis. The film is likely to be of bad quality, but structural characterization would be able to provide more clues. A logical next step would be XRD to identify the crystal phases that are present in the film. Using these results as feedback, the deposition method can be further optimized.

## Chapter 4

# PMN-PT Sol-Gel Deposition Optimization

### 4.1 Introduction

Compositional changes in the relaxor ferroelectric  $(\text{Pb}(\text{Mg}_{1/3}\text{Nb}_{2/3})\text{O}_3)_{(1-x)}(\text{PbTiO}_3)_x$  (PMN-PT) result in a structural phase transition in the system. As  $x$  is varied, the system transitions between tetragonal symmetry in PT to rhombohedral symmetry observed in PMN. The transition itself, the morphotropic phase boundary, has been of great interest due to the comparatively large piezoelectric coefficients and dielectric permittivities that occur in its vicinity [75, 76].

This boundary, however, is not sharply defined. The extensive debate that has taken place on this topic has been summarized by Cowley and Gvasaliya [77]. A widely accepted explanation, as presented by Shuvaeva *et al.* [78], is that the rhombohedral and tetragonal phases are separated by two monoclinic phases  $Cm$  and  $Pm$ . At room temperature, crystals with  $x < 0.3$  show rhombohedral ( $R3m$ ) symmetry. The increased piezoelectric properties are then assigned to a monoclinic ( $Cm$ ) phase at  $0.3 < x < 0.36$  followed by the second monoclinic ( $Pm$ ) phase at  $0.36 < x < 0.47$  and tetragonal ( $P4mm$ ) symmetry for  $x > 0.47$  (Fig. 4.1).

A variety of deposition methods, such as RF magnetron sputtering [79], pulsed laser deposition [80–82], sol-gel [83–86] and metal-organic chemical vapor deposition [87], have been employed in order to realize PMN-PT thin films. Significant progress has been made in improving the quality of these films, which is exemplified by the

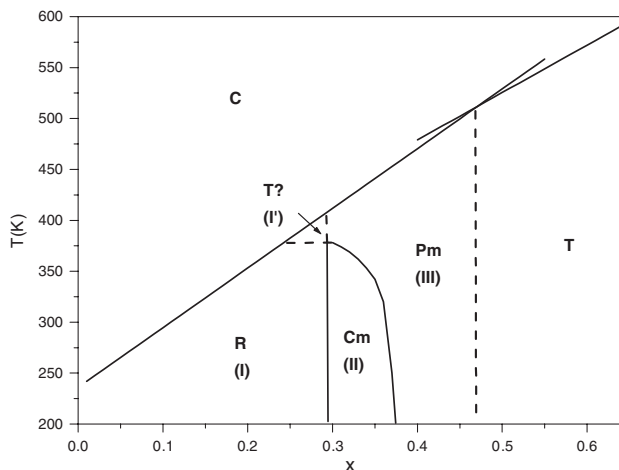


**Figure 4.1: Phase Diagram of PMN-PT** - Phase diagram of PMN-PT, showing the symmetries of the different phases. The symmetry of Phase  $\text{I}'$  remains uncertain at the present time. Taken from [78]

recent display of epitaxial PMN-PT thin films on silicon wafers by Baek *et al.* [88]. Of these techniques, sol-gel deposition has the following advantages [84]:

- Atom-level homogeneity.
- Easy control of composition.
- Good film uniformity.
- Low capital investment.
- Scalable.

With silicon integration as the perennial holy grail, research has focused on methods to realize high quality sol-gel deposited PMN-PT films on silicon wafers. A Pt template layer is often employed for this purpose and serves a multitude of purposes. Firstly, as a buffer layer for interdiffusion of atoms, secondly as a bottom electrode used for electric characterization, and lastly, as a template for growth. Highly (111)-oriented Pt is reported to induce highly (111)-oriented PMN-PT growth [84], likely due to the small lattice mismatch between Pt(111) ( $a = 3.932 \text{ \AA}$ ) and PT ( $a = 3.961 \text{ \AA}$ ) [83] and to lesser extent with PMN ( $a = 4.041 \text{ \AA}$ ) [84]. Pt, however, is known to have weak adhesion to silicon substrates [89]. Abe *et al.* [89] showed that not only does Ti act as

an effective adhesive layer, the Ti atoms diffuse through the Pt when subjected to high temperatures. This leads to a Ti/Pt alloy. For a 10:90 composition the Ti/Pt alloy can more readily adsorb oxygen atoms, which may lead to a decreased Pb evaporation rate and thereby effect stoichiometry.

Maintaining correct stoichiometry is essential to growing high quality ferroelectric films. In fact, the pyrochlore phase is known to appear when the stoichiometry deviates from the perovskite stoichiometry. Such is the case for excess Pb reacting with Nb [82]. Next to controlling the crystal phase, the other main challenge to PMN-PT thin film deposition on Pt/Si and Pt/Ti/Si is controlling the crystal orientation. Failure in overcoming either, leads to a degradation in film quality and therefore in piezoelectric performance [84]. Where the difficulty pertaining to the phase development arises due to incorrect stoichiometry, the difficulty in orientation arises due to the difference in the surface texture of Pt.

The surface texture can also effect the needed annealing temperature. For perovskite PMN-PT deposition by sol-gel, a high nucleation energy barrier must be overcome by relatively higher annealing temperatures than are used for PZT depositions. This high nucleation energy barrier can be reduced by the use of a template layer with a good match in lattice and structure, such as PT [84] or PZT [85]. Higher temperatures, however, promote the volatilization of lead. Which then, through a deviation in stoichiometry, favors the formation of pyrochlore phases [84].

Previous studies have demonstrated the existence of three major types of pyrochlores: the stoichiometric pyrochlore with formula  $\text{Pb}_2\text{Nb}_2\text{O}_7$  ( $\text{P}_2\text{N}_2$ ), A-site deficient pyrochlore such as  $\text{Pb}_3\text{Nb}_4\text{O}_{13}$  ( $\text{P}_3\text{N}_4$ ) and B-site deficient pyrochlore such as  $\text{Pb}_3\text{Nb}_2\text{O}_8$  ( $\text{P}_3\text{N}_2$ ) [90]. Unfortunately, many pyrochlore phases exist with near indistinguishable XRD signatures and plausible stoichiometries. Thus, an unambiguous phase assignment becomes nearly impossible. The coexistence of these Pb-rich and Pb-deficient phases is a result of the similar thermodynamic stabilities of the perovskite and pyrochlore phases at the temperatures under investigation [80].

In spite of these challenges, sol-gel deposited PMN-PT has been readily demonstrated. Park *et al.* [83] report on sol-gel deposited (100) and (111) oriented PMN-PT (70:30) on platinated Si. Zhou and Zhang [85] report on in-plane polarized PMN-PT (70:30) films on  $\text{ZrO}_2/\text{SiO}_2/\text{Si}$  and  $\text{PZT}/\text{ZrO}_2/\text{SiO}_2/\text{Si}$  substrates. Feng *et al.* [84] report on PMN-PT (68:32) thin films grown on Pt/Ti/SiO<sub>2</sub>/Si by a modified solution

process using an inorganic magnesium precursor. The authors show that films with a highly (111)-preferred orientation are realized when annealed at 650° C. Goel *et al.* [86] grow PMN-PT (68:32) thin films on Pt/Si substrates and indium tin oxide (ITO) coated glass substrates. Zhu *et al.* [91] report on the growth of thick film PMN-PT (65:35) on Pt/Ti/SiO<sub>2</sub>/Si.

## 4.2 Methods & Materials

A Pb(Mg<sub>1/3</sub>Nb<sub>2/3</sub>)O<sub>3</sub>-PbTiO<sub>3</sub> (70:30) sol-gel solution was obtained from CHEMAT SCIENTIFIC. Two batches of sol-gel grown PMN-PT films were fabricated.

First, silicon (111) 6” wafers were used and coated with a 10 nm layer of Ti followed by a 100-200 nm layer of highly (111) oriented Pt through e-beam evaporation. The PMN-PT solution was spin-coated at 3000 rpm for 30 s on the Pt/Ti coated SiO<sub>2</sub>/Si wafers. A temperature scheme used for the deposition of PZT on Pt/Ti/SiO<sub>2</sub>/Si [92] was first attempted. A two stage pyrolysis was employed to drive out the solvent and decompose the organic compounds. This consisted of a 5 minute heat treatment at 150° C, followed by a 5 minute heat treatment at 350° C. The film was crystallized at 700° for 60 s using an RTA. This process was repeated four and seven times to obtain a variation in thickness. The obtained XRD profiles for the first deposition are shown in Fig. 4.2(a).

For the second batch, deposition schemes for sol-gel PMN-PT from the literature were referenced. Based on choice of substrate and PMN-PT sol-gel composition, the work done by Zhou and Zhang [85] and Zhu *et al.* [91] were deemed most applicable and form the basis for the follow up sol-gel temperature scheme. Silicon (111) 6” wafers were used and coated with a 10 nm layer of Ti followed by a 100-200 nm layer of highly (111) oriented Pt through e-beam evaporation. Both Zhou and Zhang as well as Zhu *et al.* treat the films at 250° C for 1 minute, followed by 1 minute at 400°. Each film is then annealed at 650° [85] or 750° [91] for 60 s using a rapid thermal annealer (RTA). This preparation scheme was emulated. Spin coating parameters remained unaltered and a range of annealing temperatures between 650° C and 750° C was targeted. The resulting XRD profiles are shown in Fig. 4.3.

XRD profiles are compared with literature results on the PMN-PT system, for sol-gel and non sol-gel deposition methods. Additionally, simulations of crystal symmetries

likely to occur, were undertaken, using CRYSTMALMAKER software to create the crystals and SINGLECRYSTAL to simulate an XRD profile of their powder mixture. PMN-PT (70:30) was simulated as monoclinic ( $Cm$ ) — consistent with Shuvaeva *et al.* [78] — using materials parameters from Singh and Pandey [93] ( $a = 5.6962 \text{ \AA}$ ,  $b = 5.6806 \text{ \AA}$ ,  $c = 4.0123 \text{ \AA}$  and  $\beta = 90.131^\circ$ ). Tetragonal PbO, with space group  $P4/nmm$  was simulated with  $a = 3.976 \text{ \AA}$ ,  $c = 5.023 \text{ \AA}$  [94]. Orthorhombic PbO with space group  $Pbma$  and lattice parameters  $a = 5.489 \text{ \AA}$ ,  $b = 4.755 \text{ \AA}$  and  $c = 5.891 \text{ \AA}$  [94]. The simulation results are shown in Fig. 4.2(b).

### 4.3 Results & Discussion

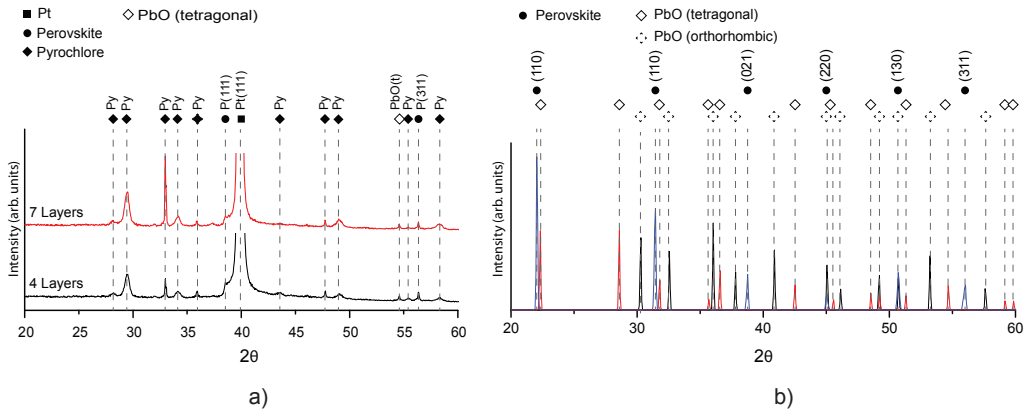


**Figure 4.2: PMN-PT Sol-Gel XRD Profiles for 4 and 7 layers - a)** XRD profiles for PMN-PT on Pt/Ti/SiO<sub>2</sub>/Si. Four and seven layers are shown. **b)** Simulated powder x-ray diffraction pattern for a (1/1/1) mixture of randomly oriented 0.7PMN-0.3PT ( $Cm$ ), PbO ( $P4/nmm$ ) and PbO ( $Pbma$ )

The XRD  $2\theta$  scan for the first, PMN-PT sol-gel deposition are shown in Fig. 4.2(a). The peak at  $39.9^\circ$  corresponds to (111) Pt and its relative intensity indicates the Pt layer is highly (111) oriented. The perovskite phase is deduced from the peaks at  $38.6^\circ$  and  $56.4^\circ$ . These peaks are frequently labeled (111) and (211) for pseudo-cubic PMN-PT (70:30) [83, 85]. However, simulating the PMN-PT (70:30) XRD profile with monoclinic space group ( $Cm$ ) and parameters — consistent with recent reported data on the PMN-PT system [77, 78, 93] — suggests that this peak corresponds to the (021) and (311) symmetry planes in monoclinic ( $Cm$ ) PMN-PT (70:30) instead (See Fig. 4.2(b)).

Using the XRD data on a range of different lead pyrochlore compositions provided by Ubic and Reaney [95] the pyrochlore peaks are identified. Certain pyrochlore peaks, such as the peak at  $33.0^\circ$ , are observed by other authors [85, 86]. The majority, however, is not. One likely reason is that — based on the multitude of corresponding peaks — the pyrochlore phase appears to be the predominant phase. Which, in most cases, can be considered an undesirable result, and would therefore go unreported in the literature.

All peaks are now accounted for, except the peak at  $54.6^\circ$ . This peak is not observed by most authors. Yu *et al.* [90] — in their solid state reaction pathway — recognize it as tetragonal PbO. This is consistent with the simulation results as is seen in Fig. 4.2(b). This is the only simulated peak for tetragonal PbO that is visible in the XRD profile. Other peaks are either negligible or ambiguously manifested with regards to the pyrochlore peaks. This could suggest a preferential orientation for tetragonal PbO in the film.

Based on Fig. 4.2(a) and (b), the observation can be made that the pyrochlore phase seems to dominate over the perovskite phase. This suggests that the temperature scheme needs to be revised.

The XRD  $2\theta$  scan for the second deposition of sol-gel PMN-PT is shown in Fig. 4.3. The presence of highly (111) oriented Pt is evidenced by the peak at  $39.9^\circ$ . The peak is slightly wider and comparatively smaller than the first deposition (Fig. 4.2(a)). This is attributed to the thinner 100 nm Pt film that is used in the second deposition, as opposed to the 200 nm Pt film in the former. Peaks at  $38.6^\circ$  correspond to the perovskite (111). This is consistent with Feng *et al.* who see preferential (111) orientation for PMN-PT on Pt(111)/Si/SiO<sub>2</sub>. Park *et al.* see perovskite peak intensity for the (111) direction increase for increasing temperatures up to  $750^\circ$  C. Again, using the lead pyrochlore XRD data provided by Ubic and Reaney [95], the pyrochlore phases are identified.

Goel *et al.* show an XRD profile for PMN-PT (68:32) sol-gel derived films, annealed at  $550^\circ$  C showing a peak at approximately  $41^\circ$ . The authors haven't denoted the peak however. Similarly Li *et al.* show a peak at  $41^\circ$  for magnetron sputtered PMN-PT (77:33) but do not label it or mention it. Maria *et al.* [80] show a peak at approximately  $41^\circ$  for PLD deposited epitaxial PMN-PT (70:30) on LaAlO<sub>3</sub> — under conditions favoring increased PbO<sub>x</sub> volatility — and denote it as PbO<sub>x</sub>.

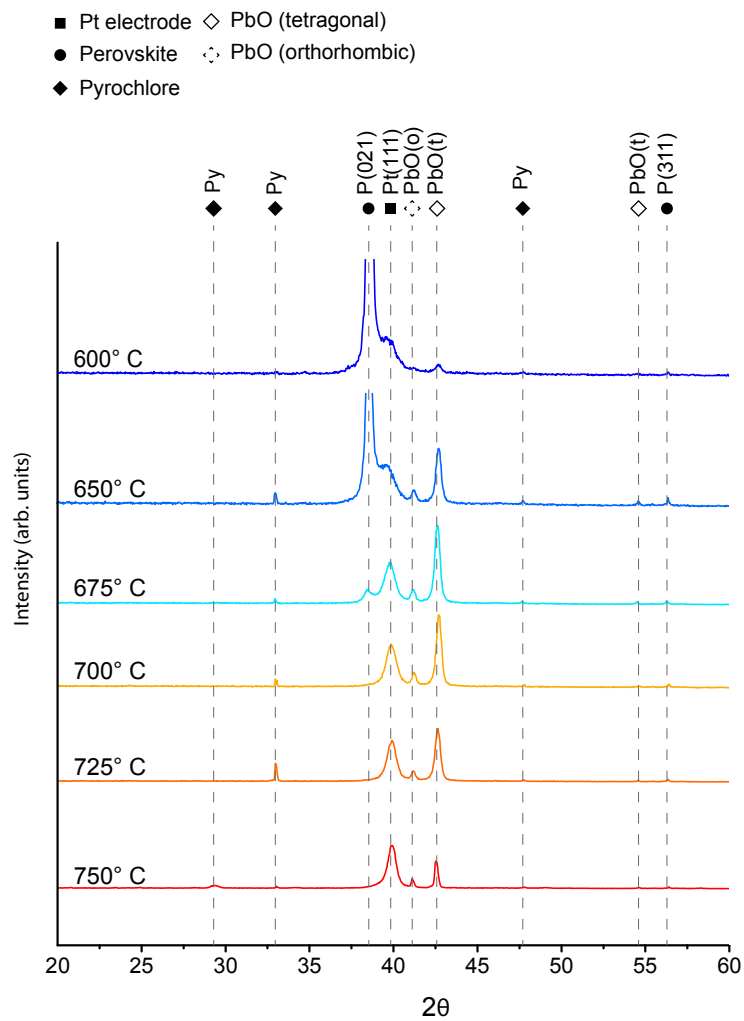


**Figure 4.3: PMN-PT Sol-Gel XRD Profiles for 1 Layer** - XRD profiles for PMN-PT on Pt/Ti/SiO<sub>2</sub>/Si. Anneal temperatures from 600° C to 750° C are shown.

After simulating the XRD profile of various candidate crystals using SINGLECRYSTAL software, the peak is found to coincide reasonably well with orthorhombic PbO (Massicot). Yu *et al.* [90] realize PMN-PT (65:35) powders and ceramics through a modified solid state reaction. The authors observe the presence of orthorhombic PbO, however different peaks are observed. This could suggest a different crystal phase is at play here, or a preferential orientation of orthorhombic PbO in the obtained film.

King *et al.* [96] measure the peak at  $42.5^\circ$  and attribute it to the perovskite phase for PMN-PT (70:30). They, however, do not label the  $hkl$  planes. The peak at  $42.5^\circ$  is not reported by any other authors. In the simulation it is found to correspond reasonably well with tetragonal PbO. Tetragonal PbO is also observed by Yu *et al.* [90], although similar to orthorhombic PbO, it is expressed across a host of different angles. Again, this could suggest a different crystal phase is at play, or a preferential orientation of tetragonal PbO in the obtained film.

The intensity of the  $42.5^\circ$  peak increases abruptly above  $600^\circ$  C, reaches a maximum at  $675^\circ$  C and gradually decreases as the temperature increases towards  $750^\circ$ . The peak at  $41^\circ$  appears at  $650^\circ$  C and slightly wanes as the temperature is increased towards  $750^\circ$  C. This is consistent with the expected increased volatility of PbO that occurs at higher temperatures, as increased lead loss is known to occur for increased temperatures [84].

The peak at  $38.6^\circ$  indicates the presence of the perovskite phase. For  $600^\circ$ , this phase seems to be dominant. Only minor peaks for tetragonal PbO and pyrochlore are observed. At  $650^\circ$  C a slight increase is seen in the intensity of the perovskite peak. This occurs in conjunction with the onset of peaks corresponding to the pyrochlore phase, and most notably, orthogonal and tetragonal PbO. Above  $650^\circ$  C the perovskite phase quickly disappears and the film seems to be dominated by the two symmetries of PbO.

## 4.4 Conclusion

PMN-PT (70:30) thin films were realized through the sol-gel process on platinated silicon substrates. When annealed at  $600^\circ$  a predominantly perovskite film is obtained. Minor contributions from the pyrochlore and other extraneous phases are traceable. Simulation results suggest the pyrochlore might be accompanied by a tetragonal PbO

phase. These result look promising and optimization efforts should focus on the temperature range at 600°.

For higher temperatures the film quality quickly deteriorates with the onset of non-perovskite phases. These phases are characterized by some pyrochlore peaks, but, predominantly by peaks occurring at 41° and 42.5°. Through comparison with results presented in the literature and simulations, these peaks were identified as orthorhombic and tetragonal PbO respectively.

Further optimization should be undertaken to eliminate any traces of non-perovskite phases in the 600° C range. Morphology studies employing SEM and AFM can provide further insight into the development of the film and its quality. Once optimized, pole figure analyses can be performed to characterize the in-plane crystal orientation, the results of which can be compared with other authors. After structural and morphological optimization, electrical characterization becomes interesting. Piezoelectric and dielectric coefficients could be obtained and compared with literature results in order to characterize the piezoelectric performance of the film.

## Chapter 5

# Simulation of Magnetoelectrically Coupled RF Devices

Part of the initial STTR proposal that led to this research initiative, were plans to develop a 3D magnetoelectrically coupled model using the finite element method (FEM). A FEM model of the coupling has the advantage that it could give us more insight into the behavior and magnitude of the induced effective field. Secondly, computational electromagnetics have become a foundation in the design process of most modern day circuits and devices as well as in the analysis of radiation and scattering problems.

### 5.1 Introduction

COMSOL MULTIPHYSICS was selected as opposed to conventional FEM software used for microwave circuit modeling such as HFSS and CST. COMSOL was selected for its known ability to incorporate mechanically moving elements in conjunction with the usual computational, mechanically static electromagnetics.

COMSOL comes with in-house modules for modeling the piezoelectric effect as well as magnetic fields. No module exists, however, for modeling magnetostrictive materials. I envisioned that it should be possible to realize magnetostrictive behavior by leveraging the existing structural mechanics and magnetic field modules to collectively model a magnetoelectric effect. A careful, bottom-up, theoretical derivation of the constitutive relations of the system would be required to successfully implement this.

## 5.2 Derivation of the Constitutive Relations

I followed the derivation presented by Auld [97] employing the IEEE nomenclature for piezomagnetism [98].

An amount of work  $\delta W$  is done on a unit mass of crystal through applied mechanical, electrical and magnetic forces. Likewise, a quantity of heat  $\delta Q$  is added to this system. The total energy of the crystal then increases by

$$\delta U = \delta Q + \delta W \quad (5.1)$$

where  $U$  is the *internal energy* per unit mass of the crystal. In thermodynamics the internal energy is expressed in terms of averages over all atoms in a system, expressed in terms of macroscopic field variables. Choosing a complete set of macroscopic state variables,  $X_1, \dots, X_n$ , the internal energy becomes a function of these state variables

$$U(X_1, \dots, X_n) \quad (5.2)$$

and the partial derivatives become

$$dU = \frac{\partial U}{\partial X_1} dX_1 + \frac{\partial U}{\partial X_2} dX_2 + \dots + \frac{\partial U}{\partial X_n} dX_n. \quad (5.3)$$

In principle, any set of variables which determines the state of the crystal in its entirety, can be used. One particular set of variables, however, gives simple physical interpretations to the partial derivatives in eq. (5.12). Through thermodynamic derivations it can be shown [97] that the change in stored energy as a product of applied increments of strain, electric and magnetic fields to a system becomes

$$dW = T_{ij} dS_{ij} + E_i dD_i + H_i dB_i \quad (5.4)$$

where subscripts indicate summation over coordinate systems. Then, from the second law of thermodynamics

$$dQ = \Theta(d\sigma) \quad (5.5)$$

where  $\Theta$  is the temperature and  $\sigma$  is the entropy. Consequently

$$dU = \Theta d\sigma + T_{ij} dS_{ij} + E_i dD_i + H_i dB_i \quad (5.6)$$

## 5.2 Derivation of the Constitutive Relations

---

which is the total derivative of the internal energy. It then follows that

$$\Theta = \frac{\partial U}{\partial \sigma}, \quad T_{ij} = \frac{\partial U}{\partial S_{ij}}, \quad E_i = \frac{\partial U}{\partial D_i}, \quad H_i = \frac{\partial U}{\partial B_i} \quad (5.7)$$

where  $\sigma$ ,  $S_{ij}$ ,  $D_i$  and  $B_i$  are independent variables. The independent variables can be altered through the definition of a new energy function such that the differentials of the desired variables appear appropriately in the differential of the energy function. Rewriting the derivative of the internal energy in eq. (5.6) by using the product of the energy terms

$$\Theta d\sigma = d(\Theta\sigma) - \sigma d\Theta \quad (5.8)$$

$$TdS = d(TS) - SdT \quad (5.9)$$

$$EdD = d(ED) - DdE \quad (5.10)$$

$$HdB = d(HB) - BdH \quad (5.11)$$

which leads to

$$dU = d(\Theta\sigma) - \sigma d\Theta + d(TS) - SdT + d(ED) - DdE + d(HB) - BdH \quad (5.12)$$

Bringing the derivatives of products to the left hand side, we obtain

$$d(U - \Theta\sigma - TS - ED - HB) = -\sigma d\Theta - SdT - DdE - BdH \quad (5.13)$$

We call this energy function the Gibbs energy function

$$G = U - \Theta\sigma - TS - ED - HB \quad (5.14)$$

whose derivative is

$$dG = -\sigma d\Theta - SdT - DdE - BdH \quad (5.15)$$

Thus,

$$\sigma = -\frac{\partial G}{\partial \Theta}, \quad S_{ij} = -\frac{\partial G}{\partial T_{ij}}, \quad D_i = -\frac{\partial G}{\partial E_i}, \quad B_i = -\frac{\partial G}{\partial H_i} \quad (5.16)$$

The dependent variables  $\sigma$ ,  $S_{ij}$ ,  $D_i$  and  $B_i$  can be expanded using a Taylor series as a function of the independent variables  $\Theta$ ,  $T_{ij}$ ,  $E_{ij}$ ,  $H_i$  which gives rise to the *constitutive*

## 5.2 Derivation of the Constitutive Relations

---

*equations* describing our system. Assuming constant entropy and constant electric field, we can limit ourselves to the expansion of  $S_{ij}$  and  $B_i$ .

However, as we will later see, our FEM software (COMSOL) requires inputs expressed in terms of  $T_{ij}$  and  $B_i$ . Thus we must change one of our dependent variables. Starting once again from the derivative of the internal energy in eq. (5.12) we use the product rule to rewrite the energy terms as in eqs. (5.8), (5.10) and (5.11), however leaving the  $T_{ij}dS_{ij}$  term untouched. This results in a modified Gibbs potential.

$$d(U - \Theta\sigma - ED - HB) = -\sigma d\Theta + TdS - DdE - BdH \quad (5.17)$$

Where

$$G = U - \Theta\sigma - ED - HB \quad (5.18)$$

and

$$dG = -\sigma d\Theta + TdS - DdE - BdH. \quad (5.19)$$

This illustrates a recipe for interchanging energy functions, such that we can choose the dependent and independent variables of our choice. This technique can be used to derive an expression for a potential function  $G$  which we can use to derive the constitutive relations of the system with dependent and independent variables of our choice.

Assuming constant temperature and electric field and using eq. (5.19), the following relationships can be shown to exist between the dependent variables and the independent quantities.

$$T_{ij} = \left( \frac{\partial G}{\partial S_{ij}} \right)_B ; \quad B_n = - \left( \frac{\partial G}{\partial H_n} \right)_T \quad (5.20)$$

where subscripts imply that those variables are held constant during the partial differentiation. Expanding  $T$  and  $B$  up to the second order and making use of the fact that the expansion is done at an arbitrary base state we obtain

$$T = \frac{\partial T_{ij}}{\partial H_m} H_m + \frac{\partial T_{ij}}{\partial S_{kl}} S_{kl} + \frac{1}{2} \frac{\partial^2 T_{ij}}{\partial S_{kl} \partial S_{mn}} S_{kl} S_{mn} + \frac{1}{2} \frac{\partial^2 T_{ij}}{\partial H_m \partial H_n} H_m H_n + \frac{\partial^2 T_{ij}}{\partial S_{kl} \partial H_p} S_{kl} H_p \quad (5.21)$$

## 5.2 Derivation of the Constitutive Relations

---

$$B = \frac{\partial B_n}{\partial S_{ij}} S_{ij} + \frac{\partial B_n}{\partial H_m} H_m + \frac{1}{2} \frac{\partial^2 B_n}{\partial S_{ij} \partial S_{kl}} S_{ij} S_{kl} + \frac{1}{2} \frac{\partial^2 B_n}{\partial H_m \partial H_p} H_m H_p + \frac{\partial^2 B_n}{\partial S_{ij} \partial H_m} S_{ij} H_m \quad (5.22)$$

The partial derivatives of  $G$  appearing in these equations represent material constants evaluated under specific conditions in the base state. While the precise constitutive relations are best represented by an infinite number of terms in the series, the number of terms will be limited by investigating the response of a particular material system subjected to specific conditions.

The values of these material constants are determined from experimental evidence. For example, tests on classical materials, such as piezoelectrics, show that many exhibit linear stress/strain relationships. This indicates that quadratic and higher order terms should be neglected in the constitutive relations. For magnetostrictive materials, experimental observations suggest [11] that the strain, for either positively or negatively applied field, is the same. That is, strain is symmetric with respect to magnetic field. This indicates that magnetic field terms will appear in the constitutive relations as even powers. Additionally strain shows a quadratic dependence on magnetic field [11]. The stiffness of a magnetostrictive material has also been reported to change as a function of applied magnetic field, indicating that a coupling term between stress and magnetic field will appear in the constitutive relation [99].

The piezomagnetic coefficient (third-order tensor), where “ $\checkmark$ ” is used to distinguish between the piezoelectric and piezomagnetic tensors

$$\frac{\partial B_n}{\partial S_{ij}} = \frac{\partial}{\partial S_{ij}} \left( -\frac{\partial G}{\partial H_n} \right) = - \left( \frac{\partial^2 G}{\partial S_{ij} \partial H_n} \right) = \check{d}_{ijn} = \check{d}_{In} \quad (5.23)$$

The second-order permeability coefficient (second-order tensor)

$$\frac{\partial B_n}{\partial H_m} = \frac{\partial}{\partial H_m} \left( -\frac{\partial G}{\partial H_n} \right) = - \left( \frac{\partial^2 G}{\partial H_m \partial H_n} \right) = \mu_{nm}^S \quad (5.24)$$

## 5.2 Derivation of the Constitutive Relations

---

Elastic stiffness or elasticity constant (fourth-order tensor)

$$\frac{\partial T_{ij}}{\partial S_{kl}} = \frac{\partial}{\partial S_{kl}} \left( \frac{\partial G}{\partial S_{ij}} \right) = \left( \frac{\partial^2 G}{\partial S_{ij} \partial S_{kl}} \right) = c_{ijkl}^H = c_{IJ}^H \quad (5.25)$$

The transpose piezomagnetic coefficient (third-order tensor)

$$\frac{\partial T_{ij}}{\partial H_n} = \frac{\partial}{\partial H_n} \left( \frac{\partial G}{\partial T_{ij}} \right) = \left( \frac{\partial^2 G}{\partial H_n \partial S_{ij}} \right) = \check{d}_{nij}^t = \check{d}_{nI}^t \quad (5.26)$$

where the capital subscripts in the piezomagnetic coefficient indicate an abbreviated subscript which is explained in Appendix B.5.

Even though the actual magnetostrictive coefficient and its inverse are defined as second order derivatives of the stress and the magnetic flux respectively, for simplicity we will be approximating the magnetoelastic effect as a linear effect by omitting any nonlinear terms.

In reality, the response of magnetostrictive materials is not only nonlinear, it is also history dependent. However, magnetostrictive materials used in applications are often biased so that the resulting material response can be approximated by a set of linear equations as can be seen in Fig. 1.10(b). Due to the analogous character of these equations to the linear electroelastic piezoelectric equations, these equations are called the *piezomagnetic* equations. By omitting the second order derivatives in eqs. (5.21) and (5.22) and using eq. (5.20) to express the partial derivatives in terms of partial derivatives of the Gibbs potential, representing material constants evaluated at a base state. The *piezomagnetic equations* become

$$T_{ij} = c_{ijkl}^H S_{kl} - \check{d}_{nij}^t H_n \quad (5.27)$$

$$B_n = \check{d}_{nij}^t S_{ij} + \mu_{kl}^S H_l \quad (5.28)$$

Omitting the indices

$$\boxed{\mathbf{T} = \mathbf{c}^H \cdot \mathbf{S} - \check{\mathbf{d}}^t : \mathbf{H}} \quad (5.29)$$

$$\boxed{\mathbf{B} = \check{\mathbf{d}} \cdot \mathbf{S} + \mu^S : \mathbf{H}} \quad (5.30)$$

Where dot and double dot products represent, respectively, summations over single subscripts and pairs of subscripts in eqs. (5.27) and (5.28).

## 5.3 Implementation

In order to implement the obtained constitutive relations, pre-existing modules in COMSOL were used. By combining a magnetic fields interface and a piezoelectric module (which includes electrostatics and structural mechanics) magnetoelectrical coupling can be realized through the inclusion of cross coupling terms between magnetic and structural quantities. The COMSOL modeling parameters that were used are discussed in Appendix B.4

### 5.3.1 The Magnetic Field Interface

The magnetic field can be accounted for through the MAGNETIC FIELDS NO CURRENTS interface in COMSOL. In magnetostatic problems where no electric currents are present, it is possible to formulate and solve the problem using a scalar magnetic potential. The derivation in [100] is followed and presented in Appendix B.1. The constitutive relation relating magnetic induction to magnetic field becomes

$$\mathbf{B} = \mu_0 \mu_r \mathbf{H} + \mathbf{B}_r \quad (5.31)$$

As can be seen from eq. (5.31) a remnant magnetic flux term  $\mathbf{B}_r$  is accounted for within COMSOL. We use this remnant flux term to account for our  $(\mathbf{e} \cdot \mathbf{S})$  term in eq. (5.30). The full expressions are given in Appendix B.3.

The piezoelectric phase is designated as a magnetic material with a relative permeability of 1

$$\mathbf{B} = \mu_0 \mathbf{H} \quad (5.32)$$

### 5.3.2 The Piezoelectric Interface

The structural mechanics framework within the piezoelectric interface in COMSOL can be used [101]. The derivation thereof is presented in Appendix B.2. Without temperature dependence or initial strains, the piezomagnetic phase can be treated as a

linear elastic material with constitutive relation

$$\boxed{\mathbf{T} = \mathbf{T}_0 + \mathbf{c} : (\mathbf{S})} \quad (5.33)$$

As can be seen from eq. (5.33) an initial stress term  $\mathbf{T}_0$  is accounted for within COMSOL. We will again be using this extra term to account for our extended coupling, this time accounting for our  $(\mathbf{e}^t : \mathbf{H})$  term in eq. (5.30). The full expressions are listed in Appendix B.3.

The piezomagnetic phase can be treated as a material with an electric permittivity of 1 with constitutive relation

$$\boxed{\mathbf{D} = \epsilon_0 \mathbf{E}} \quad (5.34)$$

The piezoelectric interface is used to define the piezoelectric phase as a piezoelectric material with corresponding constitutive relations

$$\boxed{\mathbf{S} = \mathbf{s}_E \mathbf{T} - \mathbf{d}_t \mathbf{E}} \quad (5.35)$$

and

$$\boxed{\mathbf{D} = \mathbf{d}_S \mathbf{T} + \epsilon_S \mathbf{E}} \quad (5.36)$$

## 5.4 Verification of the Model

Lou *et al.* [28] present experimental and analytical values for the induced  $\Delta H$  in a ME heterostructure consisting of a single crystal [011] cut PMN-PT (69:31) substrate and a 100 nm amorphous  $\text{Fe}_{75}\text{Ga}_{10}\text{B}_{15}$  film. The ME effect is used to show proof of concept of a tuned microwave device. An induced magnetic anisotropy of 300 Oe with an applied electric field of  $\pm 8$  kV/cm was calculated, and 330 Oe was measured.

By using this same heterostructure and the corresponding material properties the intention was to recreate these results through a third pathway: finite element analysis. The material parameters that were needed to run the simulation were obtained from a variety of sources.

### 5.4.1 Piezoelectric Material Properties

The heterostructure used by Lou *et al.* [28], consists of a [011] cut PMN-PT (69:31) substrate, which shows anisotropic in-plane behavior with piezoelectric coefficients de-

terminated by Han *et al.*  $d_{31} = -1800$  pC/N and  $d_{32} = 900$  pC/N [102]. Although providing calculated and measured piezoelectric parameters Han *et al.* [102] do not provide the elastic compliance tensor, dielectric tensor and density required by the simulation software. These data are not readily available for PMN-PT (69:31), but are available for PMN-PT (70:30) and PMN-PT (68:32) [103]. I elected to run two models for the piezoelectric phase

1. Using the piezoelectric coefficients of PMN-PT (69:31) with the material parameters of PMN-PT (70:30)
2. Using the piezoelectric coefficients of PMN-PT (70:30) with its own material parameters

for which the parameters are given in Appendix B.4.2. This is based on my assumption that the material parameters of PMN-PT (70:30) and PMN-PT (69:31), like their piezoelectric parameters, are in the same range.

### 5.4.2 Magnetostrictive Material Properties

By interpreting the nonlinear magnetostrictive effect in  $\text{Fe}_{75}\text{Ga}_{10}\text{B}_{15}$  as linear piezomagnetism one can arrive at the elements of the transpose piezomagnetic tensor used in the constitutive equations eqs. (5.29) and (5.30). The piezomagnetic elements are given by the indexed partial derivative of magnetic flux density to strain. Using the permeability, the flux density can be converted into the magnetic field. Thus, the elements of the transpose piezomagnetic tensor are defined by

$$\check{d}_{nI}^t = \frac{\partial B_n}{\partial S_I} = \frac{\partial(1/(\mu_0\mu_r)H_n)}{\partial S_I}. \quad (5.37)$$

Thus by accounting for all the elements of both the magnetic flux density tensor as well as the strain tensor, an expression for the piezomagnetic tensor can be obtained.

A 100 nm FeGaB film is considered with a relative permeability  $\mu_r$  of 1000 [28], a saturation magnetostriction of 60 ppm[28] and a Young's modulus of 65 GPa [28]. The value for applied magnetic field is estimated from the magnetic field versus magnetostriction relationships in Ref. [104]. A value of 15 Oe (= 1194 A/m) is obtained, to induce 50 ppm of magnetostriction in a FeGaB film with a saturation magnetostriction

of 60 ppm. No data on the Poisson ratio for FeGaB was available and it was estimated to be similar to other Fe-rich alloys as 0.2.

Rasoanoavy *et al.* [105] model a magnetoelectric effect in COMSOL and, analogous to Rasoanoavy *et al.*, I assume that, in the case where a magnetic field is applied along the  $x$  direction, the pseudopiezomagnetic effect in the amorphous FeGaB film causes a change in length of  $\frac{3}{2}\lambda$  along the  $x$ -direction and  $-\frac{3}{2}\lambda$  along the  $y$ -direction. When the magnetic field is rotated to be in line with the  $y$ -direction, the structure is now contracted and elongated by the same amounts, but now along the alternate axes. This holds true for amorphous magnetostrictive materials [105]. The change in length in the  $z$ -direction is neglected because the film's thickness is much smaller in relation to its length and width. The calculations of the piezomagnetic coefficients are presented in Appendix B.4.3. The piezomagnetic tensor of FeGaB in the case of longitudinal uniaxial anisotropy in the  $x$  direction, becomes in (A/m/N)

$$\check{d}_{\mathbf{nI}} = \begin{pmatrix} 10000 & -10000 & 0 & 0 & 0 & 0 \\ 0 & 0 & 0 & 0 & 0 & 0 \\ 0 & 0 & 0 & 0 & 0 & 0 \end{pmatrix} \quad (5.38)$$

The piezomagnetic tensor for FeGaB in the case of longitudinal uniaxial anisotropy in the  $y$  direction becomes, in (A/m/N)

$$\check{d}_{\mathbf{nI}} = \begin{pmatrix} 0 & 0 & 0 & 0 & 0 & 0 \\ 10000 & -10000 & 0 & 0 & 0 & 0 \\ 0 & 0 & 0 & 0 & 0 & 0 \end{pmatrix}. \quad (5.39)$$

## 5.5 Results & Discussion

For the Fe<sub>75</sub>Ga<sub>10</sub>B<sub>15</sub>/PMN-PT (69:31) heterostructure the central area of the film experiences an induced magnetic field of approximately 39 Oe, as can be seen in Fig. 5.1(a). This field becomes considerably higher along the higher strained edges reaching values of up to 1000 Oe, albeit changing from an in-plane orientation to out-of-plane. The piezoelectric deformation leads to an elongation in the  $x$ -direction and a contraction in the  $y$ -direction, due to the negative  $d_{31}$  and positive  $d_{32}$  values.

For the Fe<sub>75</sub>Ga<sub>10</sub>B<sub>15</sub>/PMN-PT (70:30) heterostructure the central area experiences an induced magnetic field, of approximately 43 Oe, as can be seen in Fig. 5.1(b). Again,

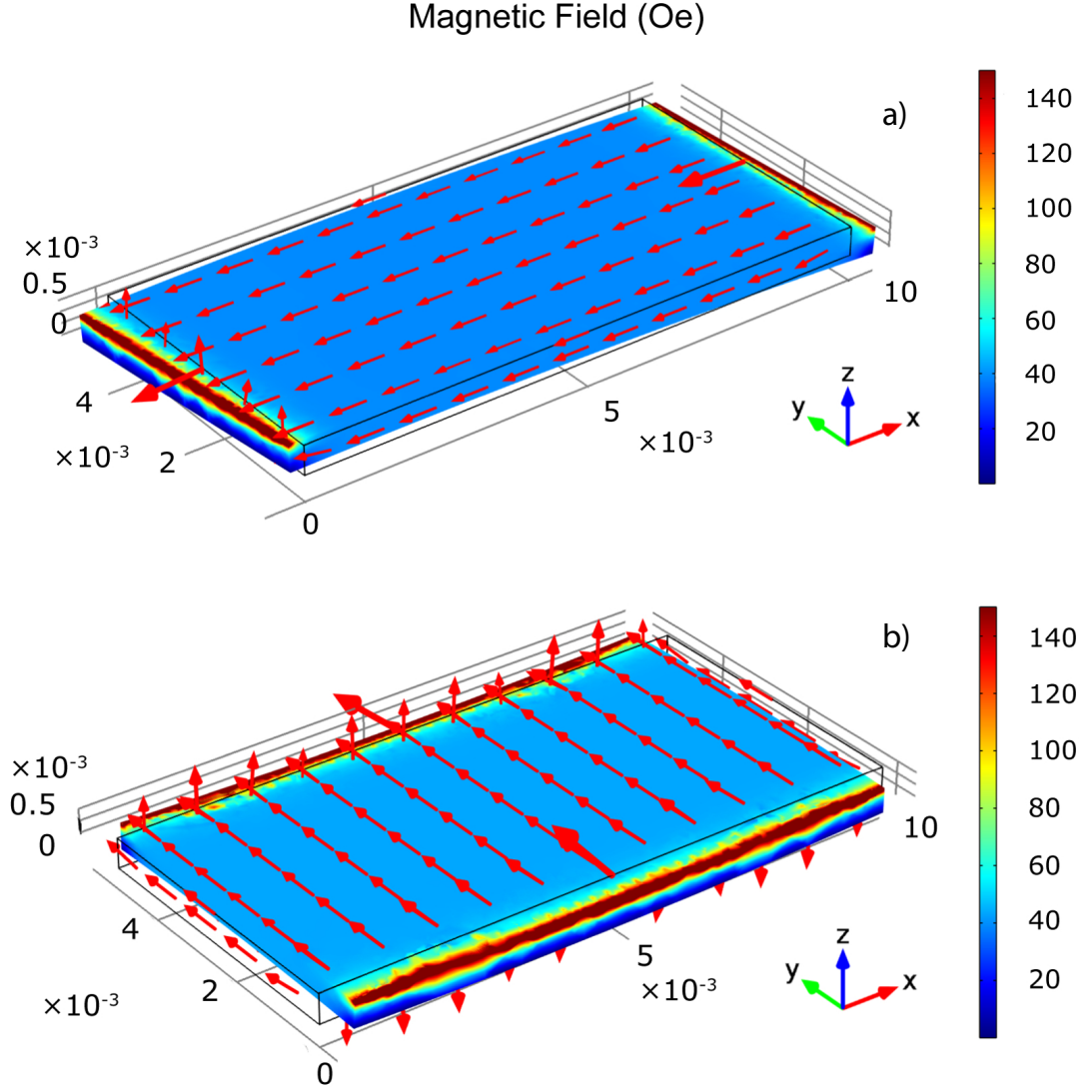


**Figure 5.1: H-Field Distribution for 100 nm  $\text{Fe}_{75}\text{Ga}_{10}\text{B}_{15}$ /PMN-PT** - a) Magnetic field in a magnetostrictive  $\text{Fe}_{75}\text{Ga}_{10}\text{B}_{15}$  film induced by a  $5 \times 10 \times 0.5$  mm PMN-30%PT single crystal [011] cut substrate with a 8 kV/cm electric field applied in the  $z$ -direction. Elongation along the  $x$ -direction and contraction along the  $y$ -direction is observed as a result of a negative  $d_{31} = -1800$  pC/N and a positive  $d_{32} = 900$ . The piezoelectric deformation is exaggerated for clarity. b) Magnetic field in a magnetostrictive  $\text{Fe}_{75}\text{Ga}_{10}\text{B}_{15}$  film by a  $5 \times 10 \times 0.5$  mm PMN-30%PT single crystal [011] cut substrate with a 8 kV/cm electric field applied along the  $z$ -direction. Elongation along the  $y$ -direction and contraction along the  $x$ -direction is observed as a result of a positive  $d_{31} = 813$  pC/N and a negative  $d_{32} = -2116$  pC/N. The piezoelectric deformation is exaggerated for clarity.

the field becomes considerably higher along the higher strained edges reaching values of 1000 Oe, again changing from an in-plane orientation to out-of-plane.

The large, apparent discrepancy in piezoelectric coefficients for PMN-PT is caused by the different coordinate systems chosen by Han *et al.* [102] and Shanthi *et al.* [103]. The coordinate transformation relating the two is  $x_1 = -y_2, y_1 = -x_2, z_1 = z_2$ .

Both configurations result in an induced magnetic field which is considerably lower than analytically and experimentally determined by Lou *et al.*. This is especially surprising since the magnetostrictive and piezoelectric layers are perfectly bonded in the FEM software, leaving no room for coupling losses. Furthermore, clamping effects on the piezoelectric substrate were minimized by imposing flexible boundary conditions. The flexible boundary conditions function as a spring foundation, which alleviates any clamping effect that may be caused on the PMN-PT substrate (Appendix B.4.1). This is confirmed by the near homogeneous  $S_1$  distribution which are seen in the simulated substrate. On these grounds – of presumably perfect coupling – a *higher* induced magnetic field was expected.

For one, this leads to the suspicion that the effective piezomagnetic constant – as the only parameter value that could not be obtained from other published work – was not accurately determined. This is somewhat understandable since the ratio between applied bias field and magnetostrictive strain were inferred from the behavior of other FeGaB alloys close in composition to Fe<sub>75</sub>Ga<sub>10</sub>B<sub>15</sub> in Ref. [104]. A magnetic field vs. magnetostriction measurement of the actual composition would provide more accuracy in estimating an effective piezomagnetic coefficient.

However, this is likely not the only cause of this discrepancy. Assuming a linear relation, as is predicted by the relations given by Lou *et al.* [28], a tenfold increase in  $\Delta H$  could be accounted for by a tenfold increase in piezomagnetic coefficient. A tenfold increase in piezomagnetic coefficient, however, implies a tenfold increase in the induced field/magnetostriction coupling. An error of up to 50% is plausible, but a tenfold increase is highly unlikely. Another cause for the the discrepancy could be the relatively coarse FEM tetrahedral mesh that was used in order to run the simulation within reasonable time limits.

The accuracy of the model can be increased by taking certain previously neglected effects into account. Chakrabarti [106] derived a 3D, two way coupled, dynamic, non-linear FEM model for magnetostrictive materials. In doing so, the author elegantly

compares the current state of research in the modeling of magnetostrictive materials in a table, according to their capabilities. Following this logic our model can be made more accurate by expanding it to include magnetodynamics (eddy currents), electromagnetic body forces and nonlinear constitutive laws. This is not to mention effects pertaining to magnetic domains, grain boundaries and hysteresis. To ultimately incorporate microwave electromagnetics, the Polder tensor permeability model as well as resonance losses also need to be taken into account.

### 5.6 Conclusion

The first steps towards a ME simulation for RF devices were undertaken. Basic 3D, two-way, linear magnetoelectrical coupling was realized in a magnetostatic approximation. The unique anisotropic in-plane strain in [011] cut PMN-PT substrates was modeled, resulting in a uniaxially induced magnetic field in the magnetostrictive film. The simulated induced magnetic field in the  $\text{Fe}_{75}\text{Ga}_{10}\text{B}_{15}$  film was considerably lower than reported by Lou *et al.* [28] from analytical calculations and experimental measurements. One cause may be that the piezomagnetic coefficients were inaccurately estimated due to a lack of magnetic field vs. magnetostriction data on this specific composition. This alone, however, does not account for the almost tenfold discrepancy in induced magnetic fields. Another cause may be the relative coarseness of the tetrahedral mesh that was used for the FEM simulation.

## Chapter 6

# Conclusion

The feasibility of a magnetoelectrically tunable isolator for frequencies above 10 GHz was investigated. An isolator mode of operation with an in-plane magnetization is likely to be most suitable for integration. This allows one to take full advantage of the benefits of anisotropic in-plane strain. Anisotropic strain provides the capacity for a significantly greater tuning range of the FMR frequency. The challenges faced in the development of magnetoelectrically tunable nonreciprocal RF devices are best characterized in terms of a set of trade-offs.

### 1. Nonreciprocity vs. Losses

Increased magnetic layer thickness can increase the nonreciprocity by increasing the total amount of contributing magnetic moments. Increased volume, however, results in an increase in eddy current losses which mitigates the nonreciprocal effect. Therefore, there will always be an optimal film thickness which minimizes eddy current losses while maximizing nonreciprocity.

The magnetic film can be engineered in certain shapes that deviate from that of a uniform planar film. A discontinuous film consisting of separate areas of film can play a role in impeding the flow of eddy currents. At the same time, a discontinuous film can decrease the coupling to the magnetic field, which results in a decreased nonreciprocal effect.

Epitaxy, as well as stoichiometry, become harder to control for increasingly thicker films. Non epitaxial growth leads to reduced crystal quality, which results in

---

increased magnetic, or dielectric losses. Deviation from the desired stoichiometry can lead to decreased magnetic or piezoelectric performance of the crystal.

## 2. Epitaxy vs. Clamping

Although the high crystal quality associated with epitaxial growth plays a part in reducing losses and promoting high electric and magnetic performance, it causes the grown layer to become rigidly attached to its substrate, thereby inhibiting its ability to deform. The severity of this clamping effect depends on the relative stiffnesses of the materials, as well as on their volume ratios. For equal stiffnesses, the clamping effect is minimized when both films have equal thickness.

## 3. Self-Biasing vs. Tunability

Self-biased operation is a highly coveted feat because it removes the need to bias the magnetic film with an external magnet. The physical principle underlying self-biased operation is based on two criteria that must be met. Firstly, the remnant magnetization which is retained by the magnetic film upon removing the bias field is close enough to the saturation magnetization as to result in high frequency operation without the occurrence of losses associated with domain movement. Secondly, the FMR frequency must occur at a frequency high enough to ensure the desired operating frequency band. This can be accomplished by maximizing the material specific quantities in the Kittel equation, namely, saturation magnetization, anisotropy field and demagnetizing field. Saturation magnetization, coercivity and anisotropy field are intricately related to one another through spin-orbit coupling. The anisotropy field represents the field that is needed to rotate the magnetization from an easy axis to a hard axis. Thus, by somewhat oversimplifying the situation, one can say that for a smaller anisotropy field it will be easier to tune the hysteretic behavior between an easy axis and a hard axis. This reveals an inherent trade-off between high zero-field operating frequencies and tunability.

## 4. Crystal Quality vs. MMIC Compatability

Achieving pristine crystal quality minimizes losses, but introduces practical issues. Pulsed laser deposition serves as a good example. The magnetic and piezoelectric figures of merit for PLD grown epitaxial thin films are among the highest

---

measured. PLD, however, requires a high vacuum deposition chamber, elevated substrate temperatures and can only ensure a comparatively small area of homogeneously deposited film. These traits make PLD incompatible with monolithic microwave integrated circuit (MMIC) technology.

Improved crystal quality for piezoelectric materials also equates to a large dielectric constant. For device geometries that use a ground plane, the structure operates as a plate capacitor with a giant capacitance. The impedance of a device is determined by the ratio between its inductance and its capacitance. Thus a comparatively large dielectric constant will strongly influence the impedance of the structure. To minimize scattering at the input and output port, the impedance of the structure must be designed to be matched with the impedance of the system (usually  $50 \Omega$ ). This can be done by optimizing the structure's geometry. Thus, the quality of the crystal will indirectly influence the ideal geometry of the device.

## 5. Ferrites vs. Alloys

Ferrites are magnetic dielectrics which makes them more resistant to eddy current losses. Magnetic alloys are conductive, however, higher magnetostriction values can be reached in certain alloys. And although ferrites generally display lower magnetostriction values, the magnetocrystalline anisotropy fields of certain ferrites are uncontested. Both materials can show easy-axis hysteresis loops with high squareness ratios given high crystal quality growth. Ferrites, and hexaferrites in particular, are generally harder to grow than for instance the FeGaB and CoFeB systems. Ferrite deposition processes often require extremely high temperatures and specific lattice matched substrates to induce high crystal quality. FeGaB and CoFeB alloys, however, show near-optimal performance in an amorphous phase.

Although ferrite systems such as BaM exhibit remarkable versatility as well as extraordinarily high operation frequencies, the potential for strain-mediated tuning is dwarfed by that of metallic magnetic alloys. By comparison, the FeGaB/PZN-PT bilayer reported by Lou *et al.* [107] showed  $156 \text{ GHz}\cdot\text{cm}/\text{kV}$  tunability, compared to the  $3 \text{ MHz}\cdot\text{cm}/\text{kV}$  for BaM/PZN-PT shown by Srinivasan *et al.* [108]. Ferrites, BaM and its substitutional systems in particular, seem more suitable for self-biased operation at GHz frequencies. Whereas amorphous alloys, such as the

---

CoFeB and FeGaB systems, seem more suitable for tunable purposes, either with a modest bias or self-biased at low GHz frequencies.

## 6. Complexity vs. Predictability

Microwave electromagnetic simulations are critical tool in the development of microwave devices. Analytical approaches quickly lose their appeal as geometries increase in complexity, as such, numerical techniques are conventionally employed in electromagnetics simulations. Even numerical procedures, however, become increasingly taxing in terms of needed computation power for increased complexity. Real materials are usually non-homogenous, anisotropic and non-linear. Additionally, bulk behavior can differ significantly from behavior at the thin film limit. With a shift towards thin film devices, the usual simplifications will become less accurate.

This research initiative has uncovered the intrinsic challenges that are faced in the development of voltage-tunable ME laminate composites for nonreciprocal RF devices. Based solely on the results presented in this thesis the feasibility of voltage-tunable isolators above 10 GHz cannot be conclusively determined. However, a thorough review of the most recent literature strongly suggest that a voltage-tunable isolator is within reach. These resources should be used to guide further research in this path and are detailed in the next section: Suggestions for Future Research.

## Chapter 7

# Suggestions for Future Work

Based on the current state of the literature on the subject of voltage-tunable ME laminate composites for nonreciprocal RF devices, an assessment can be made regarding the feasibility of a tunable isolator above 10 GHz.

The heterostructure with the highest product of magnetostrictive and piezoelectric coefficients, with a viable operation frequency is the FeGaB/PZN-PT heterostructure reported by Lou *et al.* [107]. These authors show a self-biased electric field tunable range from 1.75 to 7.57 GHz. It is reasonable to expect that this tunability can be harnessed at frequencies above 10 GHz using a small bias field. Alternatively higher zero field operating frequencies can be achieved using the CoFeB system, albeit exchanging it for a smaller tunable range due to its lower magnetostriction coefficient.

Relatively little research has focused on in-plane anisotropic piezoelectric strains. With technology shifting towards epitaxial thin layer devices, mechanical actuation would ideally be provided by thin layer piezoelectrics. Due to the clamping effect experienced by these thin films, the effective piezoelectric deformation is always reduced. Thus it will be critical to optimize the effective piezoelectric effect by employing strategies such as using crystals with anisotropic in-plane piezoelectric coefficients. Next to PMN-PT (011), PZN-PT (011) ( $d_{31} = -3000 \text{ pC}\cdot\text{N}^{-1}$ ,  $d_{32} = 1100 \text{ pC}\cdot\text{N}^{-1}$  [107]) exhibits anisotropic strain with even higher piezoelectric coefficients. The PZN-PT (011) system will likely be of increasingly technological relevance.

The versatility of BaM and its substitutional systems endows the hexagonal ferrite with the capacity to be used for applications ranging from 1 to 100 GHz. Strain mediated tunability, however, is intrinsically limited due to its comparatively low mag-

---

netostrictive constant ( $15 \cdot 10^{-6}$  [109]). Although piezoelectric-BaM heterostructures have been investigated, an alternative strategy, the tuning of the dielectric constant, seems to hold more potential in terms of tuning range. The ferroelectric  $\text{Ba}_x\text{Sr}_{1-x}\text{TiO}_3$  has been used as the dielectric in capacitors which become tunable due to the voltage tunable dielectric constant of BST. These tunable capacitors have been used to create tunable RF components such as filters. BST films have also been used in conjunction with ferromagnetic layers. The tuning then relies on the excitation of hybrid magnetolectric modes. The change in bias voltage across the BST gives rise to a change in its dielectric constant, and this then results in a change in the frequency of the hybrid magnetolectric mode and a corresponding shift in the FMR frequency of the ferromagnetic layer. Song *et al.* [110] grow epitaxial BST on a BaM slab and report an ME coefficient of 41.8 MHz/kV. Which is significantly higher than the 3 MHz/kV for BaM/PZN-PT reported by Srinivasan *et al.* [108].

A relatively new isolator design has been shown to exhibit reasonable isolation values as well as insertion losses. The ferrite coupled line circulator utilizes longitudinally magnetized ferrite materials to couple the modes between closely spaced waveguides [111]. The nonreciprocity in FCLs was explained in terms of coupled-mode theory [112, 113]. FCL isolators show the potential for a large bandwidth, planar layout and a small biasing field [8, 114, 115]. Self-biased designs using BaM have been reported [116], and Wang *et al.* [117] extend the concept to metallic magnetic films. Various authors have identified the coupled line geometry to hold the potential for true monolithic microwave integrated circuit integration [8, 114, 118]. A ferrite coupled line geometry has been shown to be able to realize significant isolation with relatively low losses. Subbiah and Alphones [119] use a coupled line geometry on a YIG slab to create a tunable isolator. It seems very reasonable, then, to assume that an FCL tunable isolator could be realized by drawing from the results for dielectric tuning of BaM reported by Srinivasan *et al.* [108] and the isolator coupled line geometry on YIG reported by Subbiah and Alphones [119].

Interesting results have been obtained by leveraging the shape anisotropy of exotic film geometries. Kuanr *et al.* [120] fabricate a monolithic isolator utilizing a field displacement effect. Nickel nanowires were fabricated by deposition in a porous alumina matrix. The shape anisotropy of these nanowires allows for a comparatively small bias field. Nanowires have also been used by author authors to realize nonreciprocal RF

---

devices that can potentially be self-biased [121–123]. Wang *et al.* [117] design and simulate a coupled line structure with an in-plane thin needle-shaped metallic magnetic film. This allows for self-biasing due to the created shape anisotropy. Additionally, the reduced shape of the magnetic film results in reduced eddy current losses, albeit also reducing the strength of the nonreciprocal effect. Shape anisotropy can not only be utilized for self-biasing, but possible also for increased tuning, as shown by Hockel *et al.* [124]. The authors were able to rotate the magnetization in 2000 nm diameter deposited Ni rings on PMN-PT substrates. It seems that, for metallic magnetic films in particular, the geometry of the film can be used as an engineering parameter to realize self-biasing, reduced losses and perhaps increased tunability through magnetization rotation.

Numerous authors [8, 26, 118] state the need for high quality epitaxial thin films for magnetoelectric devices. Both the piezoelectric and the magnetostrictive film are benefitted by an increase in crystal quality in terms of performance as well as high frequency losses. Thin films of BaM and its substitutional systems with the *c*-axis in-plane are of particular interest. So far the primary strategy showing reasonable success seems to be PLD growth on  $\alpha$ -sapphire substrates. Other deposition techniques generally show greater linewidths and diminished squareness [118].

In general, ferrites — BaM and its substitutional systems in particular — seem more suitable for self-biased operation at GHz frequencies. Whereas CoFeB and FeGaB seem to me more suitable for tunable purposes, either with a modest bias or self-biased at low GHz frequencies. Where a combination of both functionalities is desired, combining the strengths of both material categories might provide new pathways to achieving self-biased tunable RF devices above 10 GHz. For instance, a magnetized BaM film could act as biasing magnet for a FeGaB film. Or conversely, a FeGaB film could act as a tunable bias magnet for a BaM film. The challenge then becomes monolithic integration of both films while maintaining high crystal quality.

One last note relates to recent interest in self-assembled magnetoelectric nanocomposites. Simultaneous growth of certain spinel-perovskite combinations results in a self-assembled pillar array of one phase embedded in a matrix of the other. These structures show out-of-plane epitaxy, which has been viewed as having the potential to overcome the substrate clamping effect in a thin film geometry. Comparatively little

---

focus, however, has been on the RF applications for such ME heterostructures. Benatmane *et al.* [125] select a  $\text{BiFeO}_3\text{-NiFe}_2\text{O}_4$  (BFO-NFO) system due to the beneficial microwave properties of NFO, and show voltage controlled FMR shifting (albeit with large linewidths). The geometry of the magnetostrictive pillars also results in shape anisotropy effects which hold potential for self-biased operation. As stated earlier, however, ferrite-piezoelectric generally seem to have less tuning potential than a ferrite-BST heterostructure. In this case in particular, since BFO is a weak piezoelectric.

Perhaps then, the BTO-NFO [126] system is more interesting. If the BTO can be replaced by Ba-doped  $\text{SrTiO}_3$ , a new, dielectrically tunable vertical ME nanostructure could be realized. The increased surface area that results from out-of-plane epitaxy can also prove to be beneficial, as Song *et al.* [110] claim that high quality interfaces result in stronger dielectric tuning effects of BST on the ferrite.

# Appendix A

## Microwave Theory

### A.1 Frequency Bands

**Table A.1:** Waveguide Frequency Bands

Band	Frequency Range
R band	1.70 to 2.60 GHz
D band	2.20 to 3.30 GHz
S band	2.60 to 3.95 GHz
E band	3.30 to 4.90 GHz
G band	3.95 to 5.85 GHz
F band	4.90 to 7.05 GHz
C band	5.85 to 8.20 GHz
H band	7.05 to 10.10 GHz
X band	8.2 to 12.4 GHz
Ku band	12.4 to 18.0 GHz
K band	15.0 to 26.5 GHz
Ka band	26.5 to 40.0 GHz
Q band	33 to 50 GHz
U band	40 to 60 GHz
V band	50 to 75 GHz
W band	75 to 110 GHz
Y band	325 to 500 GHz

## A.2 Derivation of Polder Permeability

The torque acting on  $\mathbf{m}$  is given by

$$\mathbf{T} = \mu_0 \mathbf{m} \times \mathbf{H} \quad (\text{A.1})$$

where  $\mu_0$  is the permeability of vacuum. The spin momentum  $\mathbf{J}$  is oppositely directed to  $\mathbf{m}$ , which gives

$$\mathbf{m} = -\gamma \mathbf{J} \quad (\text{A.2})$$

where the gyromagnetic ratio  $\gamma = 2.21 \times 10^5$  (rad/s)(A/m). The torque acting on a body is equal to the rate of change of angular momentum of the body

$$\mathbf{T} = d\mathbf{J}/dt. \quad (\text{A.3})$$

Combining these equations, it follows that

$$d\mathbf{m}/dt = -\mu_0 \gamma (\mathbf{m} \times \mathbf{H}). \quad (\text{A.4})$$

If there are  $N$  unbalanced spins ( $\mathbf{m}$ ) per unit volume, the magnetic dipole moment per unit volume (the magnetization) is given by

$$\mathbf{M} = N\mathbf{m}, \quad (\text{A.5})$$

and if all the magnetic moments precess in unison, the macroscopic form of the equation of motion can be written as

$$d\mathbf{M}/dt = -\mu_0 \gamma (\mathbf{M} \times \mathbf{H}). \quad (\text{A.6})$$

The real and imaginary parts of the complex susceptibility tensor are given by [15]

$$\chi'_{xx} = \frac{\omega_0 \omega_m (\omega_0^2 - \omega^2) + \omega_0 \omega_m \omega^2 \alpha^2}{[\omega_0^2 - \omega^2 (1 + \alpha^2)]^2 + 4\omega_0^2 \omega^2 \alpha^2} \quad (\text{A.7})$$

$$\chi''_{xx} = \frac{\alpha \omega \omega_m [\omega_0^2 + \omega^2 (1 + \alpha^2)]}{[\omega_0^2 - \omega^2 (1 + \alpha^2)]^2 + 4\omega_0^2 \omega^2 \alpha^2} \quad (\text{A.8})$$

$$\chi'_{xy} = \frac{\omega \omega_m [\omega_0^2 - \omega (1 + \alpha^2)]}{[\omega_0^2 - \omega^2 (1 + \alpha^2)]^2 + 4\omega_0^2 \omega^2 \alpha^2} \quad (\text{A.9})$$

## A.2 Derivation of Polder Permeability

---

$$\chi''_{xy} = \frac{2\omega_0\omega_m\omega^2\alpha}{[\omega_0^2 - \omega^2(1 + \alpha^2)]^2 + 4\omega_0^2\omega^2\alpha^2} \quad (\text{A.10})$$

## Appendix B

# Modeling Parameters and Derivations

### B.1 Magnetic Field

Following the derivation in [100]. In magnetostatic problems where no electric currents are present, it is possible to formulate and solve the problem using a scalar magnetic potential. In a current-free region you have  $\nabla \times \mathbf{H} = 0$ . This implies that the magnetic scalar potential  $V_m$  can be defined from the relation  $\mathbf{H} = -\nabla V_m$ , which is analogous to the definition of the electric potential for static electric fields. Using the constitutive relation  $\mathbf{B} = \mu_0(\mathbf{H} + \mathbf{M})$ , the equation  $\nabla \cdot \mathbf{B} = 0$  becomes

$$-\nabla \cdot (\mu_0 \nabla V_m - \mu_0 \mathbf{M}) = 0 \quad (\text{B.1})$$

The MAGNETIC FIELDS, NO CURRENTS interface in COMSOL uses this equation for modeling of magnetostatics in the absence of electric currents.

We use one of the provided alternative versions of the constitutive relation that includes a term for the remnant flux density. The constitutive relation becomes

$$\mathbf{B} = \mu_0 \mu_r \mathbf{H} + \mathbf{B}_r \quad (\text{B.2})$$

where  $B_r$  is the remnant flux density, we use this term to introduce magnetoelastic coupling terms. The equation used by COMSOL becomes

$$\boxed{-\nabla \cdot (\mu_0 \mu_r \nabla V_m + B_r) = 0} \quad (\text{B.3})$$

### B.1.1 Boundary Conditions for the Magnetic Fields Module

With no surface currents present the interface conditions

$$\mathbf{n}_2 \times (\mathbf{A}_1 - \mathbf{A}_2) = 0 \quad (\text{B.4})$$

$$\mathbf{n}_2 \times (\mathbf{H}_1 - \mathbf{H}_2) = 0 \quad (\text{B.5})$$

need to be fulfilled. Because  $A$  is being solved for, the tangential component of the magnetic potential is always continuous, and thus the first condition is automatically fulfilled. The second condition is equivalent to the natural boundary condition and is hence also fulfilled unless surface currents are explicitly introduced. COMSOL implements these boundary conditions for us when using the MAGNETIC FIELDS NO CURRENTS interface.

## B.2 Structural Mechanics

Physical space is known as the *spatial frame* and positions in the physical space are identified by lowercase *spatial coordinate* variables  $x$ ,  $y$  and  $z$ .

Continuum mechanics also makes use of another set of coordinates, known as *material* coordinates. These are conventionally denoted by uppercase variables  $X$ ,  $Y$  and  $Z$  and are used to label material particles. Any material particle is uniquely identified by its position in some given reference configuration. If the solid stays in this configuration, material and spatial coordinates of every particle coincide and displacements are zero by definition [101].

When the solid objects deform due to external or internal forces and constraints, each material particle keeps its material coordinates  $X$ , while its spatial coordinates change with time and applied forces such that it follows a path

$$\mathbf{x} = \mathbf{x}(\mathbf{X}, t) = \mathbf{X} + \mathbf{u}(\mathbf{X}, t) \quad (\text{B.6})$$

in space. The material coordinates are constant, thus the current spatial position is uniquely determined by the displacement vector  $\mathbf{u}$ , which points from the reference position to the current position. The global Cartesian components of this displacement vector in the spatial frame, by default called  $u$ ,  $v$ , and  $w$ , are the primary dependent variables in the SOLID MECHANICS interface [101].

The gradient of the displacement, which occurs frequently in the following theory, is always computed with respect to material coordinates. In 3D:

$$\nabla \mathbf{u} = \begin{pmatrix} \frac{\partial u}{\partial X} & \frac{\partial u}{\partial Y} & \frac{\partial u}{\partial Z} \\ \frac{\partial v}{\partial X} & \frac{\partial v}{\partial Y} & \frac{\partial v}{\partial Z} \\ \frac{\partial w}{\partial X} & \frac{\partial w}{\partial Y} & \frac{\partial w}{\partial Z} \end{pmatrix} \quad (\text{B.7})$$

The total strain tensor is written in terms of the displacement gradient

$$\mathbf{S} = \frac{1}{2}(\nabla \mathbf{u} + \nabla \mathbf{u}^t) \quad (\text{B.8})$$

A more compact notation is introduced for the right-hand side. The described operation takes the symmetric part of the displacement gradient, and it will therefore be represented by appending a subscript  $s$  to the gradient symbol. Thus

$$\mathbf{S} = \frac{1}{2}(\nabla \mathbf{u} + \nabla \mathbf{u}^t) = \nabla_s \mathbf{u} \quad (\text{B.9})$$

Since the strain tensor is symmetric, each component can be specified by one subscript rather than two. These are defined according to the scheme

$$\mathbf{S} = \begin{pmatrix} S_{xx} & S_{xy} & S_{xz} \\ S_{yx} & S_{yy} & S_{yz} \\ S_{zx} & S_{zy} & S_{zz} \end{pmatrix} = \begin{pmatrix} S_1 & \frac{1}{2}S_6 & \frac{1}{2}S_5 \\ \frac{1}{2}S_6 & S_2 & \frac{1}{2}S_4 \\ \frac{1}{2}S_5 & \frac{1}{2}S_4 & S_3 \end{pmatrix} \quad (\text{B.10})$$

where the order of numbering in the abbreviated system follows the cyclic pattern shown. The convention of introducing factors  $\frac{1}{2}$  is standard practice in elasticity theory, the reason being that it simplifies some of the key equations. In this abbreviated subscript notation, the strain may be written as a six-element column matrix rather than a nine-element square matrix. That is

$$\mathbf{S} = \begin{pmatrix} S_1 \\ S_2 \\ S_3 \\ S_4 \\ S_5 \\ S_6 \end{pmatrix} \quad (\text{B.11})$$

The convention used is to denote abbreviated subscripts by upper case letters ( $S_I$ ) and full subscripts by lower case letters ( $S_{ij}$ ).

One immediate advantage of the factors  $\frac{1}{2}$  introduced is that the strain components in abbreviated subscripts are related in a simple way to the particle displacement components.

When the stress matrix is symmetric, the abbreviated subscript notation can also be used to describe stress components. In this case the convention is to omit the factors  $\frac{1}{2}$  that appear in eq. (B.12) and

$$\mathbf{T} = \begin{pmatrix} T_{xx} & T_{xy} & T_{xz} \\ T_{yx} & T_{yy} & T_{yz} \\ T_{zx} & T_{zy} & T_{zz} \end{pmatrix} = \begin{pmatrix} T_1 & T_6 & T_5 \\ T_6 & S_2 & T_4 \\ T_5 & T_4 & T_3 \end{pmatrix} \quad (\text{B.12})$$

The stress tensor can now be written as a six-element column matrix

$$\mathbf{T} = \begin{pmatrix} T_1 \\ T_2 \\ T_3 \\ T_4 \\ T_5 \\ T_6 \end{pmatrix} \quad (\text{B.13})$$

Comsol uses the The Duhamel-Hooke's law which relates the stress tensor to the strain tensor and temperature

$$\mathbf{T} = \mathbf{T}_0 + \mathbf{c} : (\mathbf{S} - \mathbf{S}_0 - \alpha \Delta \Theta) \quad (\text{B.14})$$

where  $\mathbf{c}$  is the 4th order elasticity tensor, the colon stands for the double-dot tensor product (or double contraction),  $\mathbf{T}_0$  and  $\mathbf{S}_0$  are initial stresses and strains,  $\Delta \Theta$  is the temperature difference and  $\alpha$  is the thermal expansion tensor.

Due to the symmetry, the elasticity tensor can be completely represented by a symmetric 6-by-6 matrix as:

$$\mathbf{c} = \begin{pmatrix} c_{11} & c_{12} & c_{13} & c_{14} & c_{15} & c_{16} \\ c_{21} & c_{22} & c_{23} & c_{24} & c_{25} & c_{26} \\ c_{31} & c_{32} & c_{33} & c_{34} & c_{35} & c_{36} \\ c_{41} & c_{42} & c_{43} & c_{44} & c_{45} & c_{46} \\ c_{51} & c_{52} & c_{53} & c_{54} & c_{55} & c_{56} \\ c_{61} & c_{62} & c_{63} & c_{64} & c_{65} & c_{66} \end{pmatrix} = \begin{pmatrix} c_{1111} & c_{1122} & c_{1133} & c_{1112} & c_{1123} & c_{1113} \\ c_{1122} & c_{2222} & c_{2233} & c_{2212} & c_{2223} & c_{2213} \\ c_{1133} & c_{2233} & c_{3333} & c_{3312} & c_{3323} & c_{3313} \\ c_{1112} & c_{2212} & c_{3312} & c_{1212} & c_{1223} & c_{1213} \\ c_{1123} & c_{2223} & c_{3323} & c_{1223} & c_{2323} & c_{2313} \\ c_{1113} & c_{2213} & c_{3313} & c_{1213} & c_{2313} & c_{1313} \end{pmatrix} \quad (\text{B.15})$$

The elasticity coefficients are entered following Voigt notation, the sorting of indices becomes:

$$\begin{pmatrix} 11 \\ 22 \\ 33 \\ 23, 32 \\ 13, 31 \\ 12, 21 \end{pmatrix} \leftrightarrow \begin{pmatrix} 1 \\ 2 \\ 3 \\ 4 \\ 5 \\ 6 \end{pmatrix} \leftrightarrow \begin{pmatrix} x \\ y \\ z \\ yz \\ xz \\ xy \end{pmatrix} \quad (\text{B.16})$$

### B.3 Implementation

The  $B_r$  term becomes

$$\mathbf{B}_r = \begin{pmatrix} \check{d}_{11}S_1 + \check{d}_{12}S_2 + \check{d}_{13}S_3 + \check{d}_{14}S_4 + \check{d}_{15}S_5 + \check{d}_{16}S_6 \\ \check{d}_{21}S_1 + \check{d}_{22}S_2 + \check{d}_{23}S_3 + \check{d}_{24}S_4 + \check{d}_{25}S_5 + \check{d}_{26}S_6 \\ \check{d}_{31}S_1 + \check{d}_{32}S_2 + \check{d}_{33}S_3 + \check{d}_{34}S_4 + \check{d}_{35}S_5 + \check{d}_{36}S_6 \end{pmatrix}. \quad (\text{B.17})$$

And the  $S_0$  term becomes

$$\mathbf{S}_0 = \begin{pmatrix} \check{d}_{11}H_1 + \check{d}_{21}H_2 + \check{d}_{31}H_3 \\ \check{d}_{12}H_1 + \check{d}_{22}H_2 + \check{d}_{32}H_3 \\ \check{d}_{13}H_1 + \check{d}_{23}H_2 + \check{d}_{33}H_3 \\ \check{d}_{14}H_1 + \check{d}_{24}H_2 + \check{d}_{34}H_3 \\ \check{d}_{15}H_1 + \check{d}_{25}H_2 + \check{d}_{35}H_3 \\ \check{d}_{16}H_1 + \check{d}_{26}H_2 + \check{d}_{36}H_3 \end{pmatrix}. \quad (\text{B.18})$$

## B.4 Modeling Parameters

### B.4.1 Spring Foundation

A spring foundation was applied to the bottom surface of the PMN-PT substrate. The spring constant per unit area in  $\text{N}/(\text{m}\cdot\text{m}^2)$

$$k_A = \begin{pmatrix} 5 \cdot 10^7 \\ 5 \cdot 10^7 \\ 5 \cdot 10^7 \end{pmatrix}. \quad (\text{B.19})$$

### B.4.2 Piezoelectric Material Parameters

The elastic compliance tensor is given in  $10^{-12} \text{ m}^2/\text{N}$  by

$$s_{ij}^E = \begin{pmatrix} 23.3 & -33.4 & 9.26 & 0 & 0 & 0 \\ -33.4 & 97.5 & -69.0 & 0 & 0 & 0 \\ 9.26 & -69.0 & 72.8 & 0 & 0 & 0 \\ 0 & 0 & 0 & 13.7 & 0 & 0 \\ 0 & 0 & 0 & 0 & 151.1 & 0 \\ 0 & 0 & 0 & 0 & 0 & 20.2 \end{pmatrix}. \quad (\text{B.20})$$

The piezoelectric tensor for PMN-PT (70:30) in  $10^{-12} \text{ C}/\text{N}$  is given by

$$d_{iJ} = \begin{pmatrix} 0 & 0 & 0 & 0 & 3262 & 0 \\ 0 & 0 & 0 & 289 & 0 & 0 \\ 813 & -2116 & 1916 & 0 & 0 & 0 \end{pmatrix}. \quad (\text{B.21})$$

The piezoelectric tensor for PMN-PT (69:31) in  $10^{-12} \text{ C}/\text{N}$  is given by

$$d_{iJ} = \begin{pmatrix} 0 & 0 & 0 & 0 & 5300 & 60 \\ 0 & 0 & 0 & 0 & 0 & 0 \\ -1800 & 900 & 2000 & 0 & 0 & 2520 \end{pmatrix}. \quad (\text{B.22})$$

The relative permittivity tensor is given by

$$\epsilon_{ij}^S = \begin{pmatrix} 1405 & 0 & 0 \\ 0 & 1216 & 0 \\ 0 & 0 & 766 \end{pmatrix}, \quad (\text{B.23})$$

and the density in  $\text{kg}/\text{m}^3$

$$\rho = 8150. \quad (\text{B.24})$$

### B.4.3 Magnetostrictive Material Parameters

For uniaxial anisotropy along the  $x$ -axis, using the altered relative permeability ( $\mu_r = 1000$ ) [28] the piezomagnetic tensor coefficients become:

$$e_{11} = \frac{\mu_0 \mu_r \partial H_1}{\partial S_1} = \frac{1.5 \text{ N/A/m}}{3 \cdot 50 \cdot 10^{-6}} = 10000 \text{ N/A/m} \quad (\text{B.25})$$

$$e_{11} = \frac{\mu_0 \mu_r \partial H_1}{\partial S_1} = \frac{1.5 \text{ N/A/m}}{-3 \cdot 50 \cdot 10^{-6}} = 10000 \text{ N/A/m} \quad (\text{B.26})$$

And for uniaxial anisotropy along the  $y$ -axis, the piezomagnetic tensor coefficients become:

$$e_{21} = \frac{\mu_0 \mu_r \partial H_1}{\partial S_1} = \frac{1.5 \text{ N/A/m}}{-3 \cdot 50 \cdot 10^{-6}} = 10000 \text{ N/A/m} \quad (\text{B.27})$$

$$e_{22} = \frac{\mu_0 \mu_r \partial H_1}{\partial S_1} = \frac{1.5 \text{ N/A/m}}{3 \cdot 50 \cdot 10^{-6}} = 10000 \text{ N/A/m} \quad (\text{B.28})$$

The Young modulus is given by [28]

$$Y = 65 \text{ GPa} \quad (\text{B.29})$$

The Poisson's ratio is estimated as

$$\nu = 0.2 \quad (\text{B.30})$$

The density was taken to be that of Armco Iron at 300° K in kg/m<sup>3</sup>

$$\rho = 7855 \quad (\text{B.31})$$

## B.5 Notation of the Piezoelectric and Piezomagnetic Tensors

Since  $S_{ij} = S_{ji}$ , the arguments used in [101] to show that  $s_{ijkl} = s_{jikl}$  and  $c_{ijkl} = c_{ijlk}$  can also be applied here. That is,  $d_{ijk}$  can always be defined so that  $d_{ijk} = d_{jik}$ . When the stress is symmetric,  $T_{ij} = T_{ji}$ , the definition  $d_{ijk} = d_{ikj}$  can also be made. This means that the abbreviated subscript can be introduced

## B.5 Notation of the Piezoelectric and Piezomagnetic Tensors

---

$$e_{ijk} = e_{iJ} = \begin{pmatrix} d_{11} & d_{12} & d_{13} & d_{14} & d_{15} & d_{16} \\ d_{21} & d_{22} & d_{23} & d_{24} & d_{25} & d_{26} \\ d_{31} & d_{32} & d_{33} & d_{34} & d_{35} & d_{36} \end{pmatrix} \quad (\text{B.32})$$

Throughout this capital letter subscripts range over the subset of integers

1, 2, 3, 4, 5, 6

## Appendix C

# Thin Film Characterization

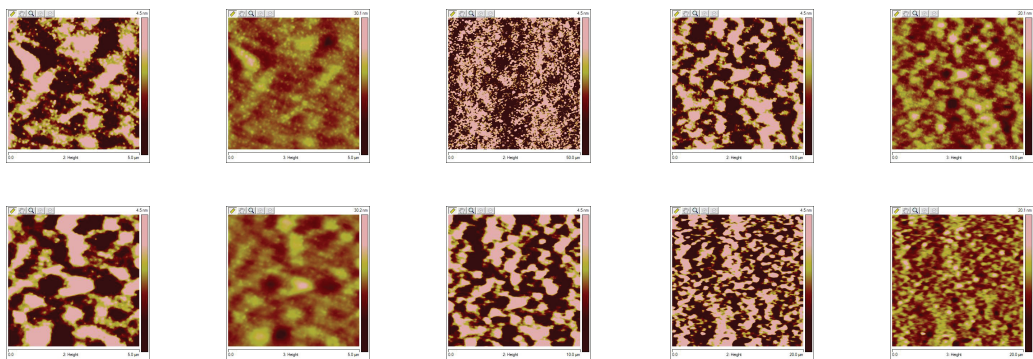


**Figure C.1:** BaM on Pt/Si - AFM images of metallo-organic decomposition growth of BaM on Pt(111)/Si.

# References

- [1] G. Balk, *Archives of the Dutch East India Company (VOC) and the local institutions in Batavia (Jakarta)* (2007).
- [2] W. Cady, *Piezoelectricity: an introduction to the theory and applications of electromechanical phenomena* (1964).
- [3] W. Schumann, *Gemstones of the World: Newly Revised & Expanded Fourth Edition* (2009).
- [4] R. Dietrich, *The tourmaline group* (1985).
- [5] P. Curie, *J. Phys. Theor. Appl.* (1894).
- [6] J. Van Suchtelen, *Philips Res Repts* **27**, 28 (1972).
- [7] J. Coey, *Magnetism and Magnetic Materials* (2009).
- [8] V. G. Harris, *Handbook of Magnetic Materials* (2012).
- [9] N. Spaldin, *Magnetic Materials: Fundamentals and Applications* (Cambridge Univ Pr, 2010).
- [10] S. Crane, *Magnetolectric coupling in multifunctional nanostructured complex oxide thin films*, Ph.D. thesis, UC Berkeley (2009).
- [11] G. Engdahl, *Handbook of giant magnetostrictive materials* (2000).
- [12] K. Buschow, *Physics of magnetism and magnetic materials* (2003).
- [13] D. Polder, *Philosophical magazine* , 253 (1949).
- [14] J. Adam, L. Davis, and G. Dionne, *Microwave Theory* **50**, 721 (2002).
- [15] D. Pozar, *Microwave engineering* (2009).
- [16] U. Özgür, Y. Alivov, and H. Morkoç, *Journal of Materials Science: Materials in Electronics* **20**, 789 (2009).
- [17] A. Gurevich and G. Melkov, *Magnetization oscillations and waves* (CRC, 1996).
- [18] A. Fuller, *Ferrites at microwave frequencies* (1987).
- [19] J. Golio, *The RF and microwave handbook* (2001).
- [20] Philips, *Application Note*, Tech. Rep. (Philips Semiconductors, 2003).
- [21] R. Newnham, *Properties of materials: anisotropy, symmetry, structure* (2005).
- [22] K. Rabe and C. Ahn, *Physics of ferroelectrics: a modern perspective*, Vol. 9 (Springer Verlag, 2007).
- [23] W. Eerenstein, N. D. Mathur, and J. F. Scott, *Nature* **442**, 759 (2006).
- [24] R. Newnham, D. Skinner, and L. Cross, *Materials Research Bulletin* **13**, 525 (1978).
- [25] M. Bichurin, D. Filippov, V. Petrov, V. Laletsin, N. Paddubnaya, and G. Srinivasan, *Physical Review B* **68**, 10 (2003).
- [26] G. Srinivasan, *Annual Review of Materials Research* **40**, 153 (2010).
- [27] M. Avellaneda and G. Harshé, *Journal of intelligent material systems and structures* **5**, 501 (1994).
- [28] J. Lou, D. Reed, M. Liu, C. Pettiford, and N. X. Sun, *Compare A Journal Of Comparative Education* , 33 (2009).
- [29] M. Liu, O. Obi, J. Lou, Y. Chen, Z. Cai, S. Stoute, M. Espanol, M. Lew, X. Situ, K. S. Ziemer, V. G. Harris, and N. X. Sun, *Advanced Functional Materials* **19**, 1826 (2009).
- [30] C. Pettiford, S. Dasgupta, S. Yoon, and N. Sun, *IEEE Transactions on Magnetics* **43**, 3343 (2007).
- [31] A. Tatarenko and V. Gheevarghese, *Electronics* **42**, 3 (2006).
- [32] A. Tatarenko and G. Srinivasan, *Microwave and Optical Technology Letters* **53**, 261 (2011).
- [33] B. Noren, *Microwave Journal* (2004).
- [34] M. Bichurin, R. Petrov, and Y. Kiliba, *Ferroelectrics* , 37 (1997).
- [35] Y. Fetisov and G. Srinivasan, *Electronics Letters* **41**, 1 (2005).
- [36] G. Srinivasan, *Final Report*, Tech. Rep. (Office of Naval Research, 2010).
- [37] M. Munakata and M. Yagi, *IEEE Transactions on Magnetics* **41**, 3262 (2005).
- [38] D. Wang, C. Nordman, Z. Qian, J. M. Daughton, and J. Myers, *Journal of Applied Physics* **97**, 10C906 (2005).
- [39] W. Ishak, *Proceedings of the IEEE* **76**, 171 (1988).
- [40] P. Khalili Amiri, B. Rejaei, M. Vroubel, and Y. Zhuang, *Applied Physics Letters* **91**, 062502 (2007).
- [41] P. Amiri, B. Rejaei, M. Vroubel, and S. Wang, *IEEE Transactions on Magnetics* **45**, 4215 (2009).
- [42] M. Bailleul, D. Olligs, and C. Fermon, *Physical Review Letters* **91**, 1 (2003).
- [43] V. Demidov, B. Kalinikos, and P. Edenhofer, *Journal of applied ...* **91**, 10007 (2002).
- [44] D. D. Stancil, *Spin Waves* (Springer US, Boston, MA, 2009).

## REFERENCES

- [45] S. Seshadri, Proceedings of the IEEE , 506 (1970).
- [46] N. Kinayman and M. Aksun, *Modern microwave circuits* (2005).
- [47] E.-B. El-Sharawy and J.-S. Guo, Microwave Symposium Digest, 1995 ... **1**, 107 (1995).
- [48] M. Liu, O. Obi, J. Lou, S. Stoute, J. Y. Huang, Z. Cai, K. S. Ziemer, and N. X. Sun, Applied Physics Letters **92**, 152504 (2008).
- [49] G. Srinivasan and Y. Fetisov, Integrated Ferroelectrics **83**, 89 (2006).
- [50] J. Slonczewski, B. Petek, and B. Argyle, IEEE Transactions on Magnetics **24**, 2045 (1988).
- [51] W. Martienssen and H. Warlimont, *Springer handbook of condensed matter and materials data* (2005).
- [52] T. Wu, P. Zhao, M. Bao, A. Bur, J. L. Hockel, K. Wong, K. P. Mohanchandra, C. S. Lynch, and G. P. Carman, Journal of Applied Physics **109**, 124101 (2011).
- [53] T. Wu, A. Bur, P. Zhao, K. P. Mohanchandra, K. Wong, K. L. Wang, C. S. Lynch, and G. P. Carman, Applied Physics Letters **98**, 012504 (2011).
- [54] J. Lou, D. Reed, C. Pettiford, M. Liu, P. Han, S. Dong, and N. X. Sun, Applied Physics Letters **92**, 262502 (2008).
- [55] M. K. Chung and S.-R. Lee, Physica Status Solidi (a) **201**, 1747 (2004).
- [56] K. Ikeda, K. Kobayashi, and M. Fujimoto, Journal of the American ... **73**, 169 (2002).
- [57] L. Lin, N. Thiagarajah, H. W. Joo, J. Heo, K. A. Lee, and S. Bae, Applied Physics Letters **97**, 242514 (2010).
- [58] C. L. Platt, a. E. Berkowitz, D. J. Smith, and M. R. McCartney, Journal of Applied Physics **88**, 2058 (2000).
- [59] T. Thomson and P. Riedi, IEEE Transactions on Magnetics **34**, 1045 (1998).
- [60] S. Bae, J. Li, J. H. Judy, and S. Zurn, Applied Physics Letters **77**, 3435 (2000).
- [61] J. Wu, J. Lou, M. Li, and G. Yang, Microwave Theory ... **60**, 1587 (2012).
- [62] I. Harward, Y. Nie, a. Gardner, L. Reisman, and Z. Celinski, Journal of Applied Physics **111**, 07A514 (2012).
- [63] Y.-Y. Song, S. Kalarickal, and C. E. Patton, Journal of Applied Physics **94**, 5103 (2003).
- [64] S. D. Yoon and C. Vittoria, Journal of Applied Physics **93**, 8597 (2003).
- [65] M. S. Yuan, H. L. Glass, and L. R. Adkins, Applied Physics Letters **53**, 340 (1988).
- [66] Z. Cai, T. L. Goodrich, B. Sun, Z. Chen, V. G. Harris, and K. S. Ziemer, Journal of Physics D: Applied Physics **43**, 095002 (2010).
- [67] S. Pignard and J. Sénateur, Journal de Physique IV **7**, 4 (1997).
- [68] Y. Chen, T. Fitchorov, Z. Cai, K. S. Ziemer, C. Vittoria, and V. G. Harris, Journal of Physics D: Applied Physics **43**, 155001 (2010).
- [69] Y. Nie, I. Harward, K. Balin, A. Beaubien, and Z. Celinski, Journal of Applied Physics **107**, 073903 (2010).
- [70] Z. Wang, Y.-Y. Song, Y. Sun, J. Bevivino, M. Wu, V. Veerakumar, T. J. Fal, and R. E. Camley, Applied Physics Letters **97**, 072509 (2010).
- [71] R. Camley, Z. Celinski, and T. Fal, ... and Magnetic Materials **321**, 2048 (2009).
- [72] P. Shi, H. How, and X. Zuo, IEEE Transactions on Magnetics **37**, 2389 (2001).
- [73] S. Capraro, T. Rouiller, M. Le Berre, J.-P. Chatelon, B. Bayard, D. Barbier, and J. J. Rousseau, IEEE Transactions on Components and Packaging Technologies **30**, 411 (2007).
- [74] M. Wittenauer, J. Nyenhuis, and A. Schindler, Journal of Crystal Growth **130**, 533 (1993).
- [75] X. Zhao, B. Fang, H. Cao, Y. Guo, and H. Luo, Materials Science and Engineering: B **96**, 254 (2002).
- [76] S.-E. Park and T. R. ShROUT, Journal of Applied Physics **82**, 1804 (1997).
- [77] R. Cowley and S. Gvasaliya, Advances in ... **60**, 229 (2011).
- [78] V. Shuvaeva, A. Glazer, and D. Zekria, Journal of Physics: ... **17**, 5709 (2005).
- [79] W. Li, J. Xue, Z. Zhou, J. Wang, H. Zhu, and J. Miao, Ceramics International **30**, 1539 (2004).
- [80] J.-P. Maria, W. Hackenberger, and S. Trolrier-McKinstry, Journal of Applied Physics **84**, 5147 (1998).
- [81] V. Nagarajan, S. P. Alpay, C. S. Ganpule, B. K. Nagaraj, S. Aggarwal, E. D. Williams, a. L. Roytburd, and R. Ramesh, Applied Physics Letters **77**, 438 (2000).
- [82] A. Laha, S. Saha, and S. Krupanidhi, Thin solid films **424**, 274 (2003).
- [83] J. H. Park, F. Xu, and S. Trolrier-McKinstry, Journal of Applied Physics **89**, 568 (2001).
- [84] M. Feng, W. Wang, H. Ke, J. Rao, and Y. Zhou, Journal of Alloys and Compounds **495**, 154 (2010).
- [85] Q. Zhou and Q. Zhang, Journal of the American Ceramic Society **2000**, 2000 (2002).
- [86] T. Goel, P. Kumar, A. James, and C. Prakash, Journal of electroceramics **13**, 503 (2004).
- [87] S. Lee and M. Custodio, Journal of Crystal Growth **226**, 247 (2001).

## REFERENCES

- [88] S. H. Baek, J. Park, D. M. Kim, V. a. Aksyuk, R. R. Das, S. D. Bu, D. a. Felker, J. Lettieri, V. Vaithyanathan, S. S. N. Bharadwaja, N. Bassiri-Gharb, Y. B. Chen, H. P. Sun, C. M. Folkman, H. W. Jang, D. J. Kreft, S. K. Streiffer, R. Ramesh, X. Q. Pan, S. Trolier-McKinstry, D. G. Schlom, M. S. Rzchowski, R. H. Blick, and C. B. Eom, *Science* (New York, N.Y.) **334**, 958 (2011).
- [89] K. Abe, H. Tomita, and H. Toyoda, *Japanese Journal of Applied Physics* (1991).
- [90] S. Yu, H. Huang, L. Zhou, and Y. Ye, *Journal of the American Ceramic Society* **91**, 1057 (2008).
- [91] B. P. Zhu, Q. F. Zhou, K. K. Shung, Q. Wei, and Y. H. Huang, 2009 IEEE International Ultrasonics Symposium , 2197 (2009).
- [92] T.-K. Chung, G. P. Carman, and K. P. Mohanchandra, *Applied Physics Letters* **92**, 112509 (2008).
- [93] A. Singh and D. Pandey, *Physical Review B* **67**, 1 (2003).
- [94] D. Adams, A. Christy, J. Haines, and S. Clark, *Physical Review B* **46**, 358 (1992).
- [95] R. Ulic and I. Reaney, *Journal of the American Ceramic Society* **78**, 2472 (2002).
- [96] H. King, S. Ferguson, D. Waechter, and S. Prasad, *Proc. ICONS* (2002).
- [97] B. Auld, *Acoustic fields and waves in solids* (1990).
- [98] *IEEE standard on magnetostrictive materials: piezomagnetic nomenclature* (IEEE Standards Board, 1991).
- [99] G. P. Carman and M. Mitrovic, *Journal of Intelligent Material Systems and Structures* **6**, 673 (1995).
- [100] Comsol, *AC / DC Module User Guide*.
- [101] Comsol, *Structural Mechanics Module*.
- [102] P. Han, W. Yan, J. Tian, X. Huang, and H. Pan, *Applied Physics Letters* **86**, 052902 (2005).
- [103] M. Shanthi, L. C. Lim, K. K. Rajan, and J. Jin, *Applied Physics Letters* **92**, 142906 (2008).
- [104] J. Lou, R. E. Insignares, Z. Cai, K. S. Ziemer, M. Liu, and N. X. Sun, *Applied Physics Letters* **91**, 182504 (2007).
- [105] F. Rasoanoavy, V. Laur, S. De Blasi, J. Lezaca, P. QuelAffelAlec, K. Garelo, and B. Viala, *Journal of Applied Physics* **107**, 09E313 (2010).
- [106] S. Chakrabarti, *Modeling of 3D Magnetostrictive Systems with Application to Galfenol and Terfenol-D Transducers*, Ph.D. thesis (2011).
- [107] J. Lou, M. Liu, D. Reed, Y. Ren, and N. Sun, *Advanced Materials* **21**, 4711 (2009).
- [108] G. Srinivasan, a. S. Tatarenko, V. Mathe, and M. I. Bichurin, *The European Physical Journal B* **71**, 371 (2009).
- [109] G. Srinivasan, I. V. Zavislyak, and a. S. Tatarenko, *Applied Physics Letters* **89**, 152508 (2006).
- [110] Y. Song, J. Das, P. Krivosik, H. Seo, and M. Wu, *Magnetics Letters, IEEE* **1**, 2500204 (2010).
- [111] L. Davis and D. Sillars, *IEEE Transactions on Microwave Theory and Techniques* **MTT-34**, 804 (1986).
- [112] D. Marcuse, *Bell System Technical Journal* **54**, 985 (1975).
- [113] J. Mazur and M. Mrozowski, . . . and Techniques, *IEEE Transactions on* **31**, 159 (1989).
- [114] C. Queck and L. Davis, *Microwave Theory and Techniques, IEEE . . .* **50**, 2910 (2002).
- [115] S. D. Yoon, J. Wang, N. Sun, C. Vittoria, and V. G. Harris, *IEEE Transactions on Magnetics* **43**, 2639 (2007).
- [116] C. Queck, *Electronics Letters* **39**, 4 (2003).
- [117] J. Wang, S. Yoon, V. Harris, C. Vittoria, and N. Sun, *Electronics letters* **43**, 49 (2007).
- [118] M. Wu, *Edited by Leszek Malkinski* (2012).
- [119] S. Subbiah and A. Alphones, *IEE Proceedings Microwave, Antennas & Propagation* **150**, 219 (2003).
- [120] B. K. Kuanr, V. Veerakumar, R. Marson, S. R. Mishra, R. E. Camley, and Z. Celinski, *Applied Physics Letters* **94**, 202505 (2009).
- [121] M. Darques, J. De la Torre Medina, L. Piraux, L. Cagnon, and I. Huynen, *Nanotechnology* **21**, 145208 (2010).
- [122] A. Saib, M. Darques, L. Piraux, D. Vanhoenacker-Janvier, and I. Huynen, *Journal of Physics D: Applied Physics* **38**, 2759 (2005).
- [123] L. Carignan and T. Kodera, *Proceedings of the 39th European Microwave Conference* **39**, 743 (2009).
- [124] J. L. Hockel, A. Bur, T. Wu, K. P. Wetzlar, and G. P. Carman, *Applied Physics Letters* **022401**, 3 (2012).
- [125] N. Benatmane, S. P. Crane, F. Zavaliche, R. Ramesh, and T. W. Clinton, *Applied Physics Letters* **96**, 082503 (2010).
- [126] C. Deng, Y. Zhang, J. Ma, Y. Lin, and C.-W. Nan, *Acta Materialia* **56**, 405 (2008).